Czech University of Life Sciences Prague

Faculty of Environmental Sciences

Indirect methods for modelling forest microclimate

Vít Kašpar

This dissertation thesis is submitted for the degree

Doctor of Philosophy at the Department of Spatial Sciences.

Prague

March 2023

Indirect methods for modelling forest microclimate

Dissertation Thesis

Author: Vít Kašpar

Supervisor: Assoc. Prof. Jan Wild
                  Czech University of Life Sciences Prague

I hereby declare that the dissertation thesis entitled *Indirect methods for modelling forest microclimate* submitted for the degree Doctor of Philosophy in study programme Landscape Engineering, field of study Environmental Modelling is my original work guided by my supervisor. All sources of information, text, illustration, tables and images have been specifically cited.

....
Vít Kašpar

Acknowledgements

There are, as always, too many people to thank individually for their help and support throughout my years of studying for a PhD. In particular, for the publication of the studies in this book, I am grateful to Jan Wild for encouraging me to pursue science, Martin Kopecký for showing me the true meaning of science, all other members of the Department of Geoecology at the Institute of Botany for creating an inspiring and motivating environment that I was fortunate enough to be a part of, Vítězslav Moudrý and Petra Šímová for giving me the confidence and freedom to study independently, Miloš Zapletal for broadening my focus, and the journal editors and anonymous reviewers who supported my articles. Without their encouragement, I may have had to abandon my research some time ago.

My deepest gratitude goes to my father-in-law, Ivo, who, as a practical man, constantly mirrored to me the meaning of my research, my mother-in-law, Danuše, who provided me with material support during times when I needed to focus on my work, my family in Pilsen - my mother Markéta, my father Čestmír, my sister Klára, and her family - on whose long-distance love and support I have come to depend, and my wife Barbora and our daughter, Odeta, who make every day special.

Abstract

The microclimate of forests, which refers to the fine-scale variation of climatic conditions near the ground, is critical to the survival and functioning of terrestrial organisms. However, monitoring and understanding the processes that govern microclimate at an adequate spatial-temporal resolution under forest canopies is challenging. Given that the forest microclimate is primarily shaped by the characteristics of the forest canopy, local climatic conditions can potentially be investigated through associated vegetation properties.

The objective of this thesis is to explore the suitability of indirect, field-based, and remote sensing methods in quantifying tree canopy structures as proxy parameters for forest microclimate modelling. By using data from hemispherical photographs, unmanned aerial systems, satellite products, and in-situ measured radiation and meteorological properties, I examined the relationship between forest structure and microclimatic conditions under the forest canopy.

The results indicate that indirectly derived canopy structure variables explain microclimatic conditions well and thus provide suitable inputs for microclimate models. The demonstrated approaches and suggested methodologies for gathering, processing, and applying microclimate-relevant data on vegetation characteristics of various temperate forests can make a substantial advance in forest microclimate modelling.

Abstrakt (Czech)

Lesní mikroklima, tedy jemná variabilita klimatických podmínek v blízkosti země, hraje zásadní roli v přežití a funkci suchozemských organismů. Sledování a pochopení procesů, jimiž se řídí mikroklima při adekvátním prostorově-časovém rozlišení, je však pod lesními korunami složité. Vzhledem k tomu, že lesní mikroklima je utvářeno především vlastnostmi lesního zápoje, mohou být místní klimatické podmínky potenciálně zkoumány pomocí souvisejících vlastností vegetace.

Práce si klade za cíl prozkoumat využitelnost nepřímých metod na základě terénního sběru dat i dálkového průzkumu Země při kvantifikaci struktury korun stromů jako zástupného parametru modelování lesního mikroklimatu. Pomocí dat z hemisférických fotografií, bezpilotních systémů a satelitních produktů a in-situ měřených radiačních a meteorologických vlastností byl zkoumán vztah mezi strukturou lesa a mikroklimatickými podmínkami pod korunovým zápojem.

Výsledky ukázaly, že nepřímo odvozené proměnné struktury zápoje dobře vysvětlují mikroklimatické podmínky a poskytují tak vhodné vstupy pro modely mikroklimatu. Demonstrované přístupy a navrhované metodologie pro sběr, zpracování a aplikaci mikroklimaticky relevantních dat o vegetačních charakteristikách různých lesů mírného pásma tak mohou znamenat důležitý pokrok v modelování lesního mikroklimatu.

Contents

II Research   34

Part I

Introduction and Theory

Chapter 1

Thesis Preface

1.1 Foreword

Since ancient times, forests have been mysterious places, shrouded in secrets and perceived as hostile and inhospitable environments for humans. The need to cultivate these dark and impenetrable forests full of wild beasts has shaped our relationship with them for millennia. Many mythological figures associated with the forest disappeared with the advent of rationality and scientific knowledge, which replaced the romantic adoration of its beauty or the pragmatism of economic utility. However, one persisted over time: the forest has always been viewed as an environment that is difficult to access, observe, and even understand to some extent.

The unique scenery of dense and unfathomable forest canopies was described by Alfred Russel Wallace (1878):

"The observer new to the scene would perhaps be first struck by the varied yet symmetrical trunks, which rise up with perfect straightness to a great height without a branch, and which, being placed at a considerable average distance apart, give an impression similar to that produced by the columns of some enormous building. Overhead, at a height, perhaps, of a hundred feet, is an almost broken canopy of foliage formed by the meeting together of these great trees and their interlacing branches; and this canopy is usually so dense that but an indistinct glimmer

of the sky is to be seen, and even the intense tropical sunlight only penetrates to the ground subdued and broken up into scattered fragments. There is a weird gloom and a solemn silence, which combine to produce a sense of the vast—the primaeval—almost of the infinite. It is a world in which man seems an intruder."

In the past 35 years, our ability to quantify canopy architecture and understand internal processes has expanded beyond the ground-based perspective of the 19th century. Today, indirect observation methods provide us with valuable information about forest environments that can be sensed effectively on a large scale and without the need to physically measure at a site. This offers new insights under tree canopies in difficult-to-access areas, such as tropical rainforests or boreal taiga, where a great deal of world biodiversity resides, and which are essential for maintaining planetary biophysical cycles.

Novel approaches for quantifying forest architecture, which drives inner forest processes, may advance our understanding and modelling of the mechanisms within forests and their canopies. Given the impacts of human-induced climate change and environmental degradation, forest canopies represent an adaptive potential that provides functions that moderate processes related to atmospheric physics and chemical composition, among others. Comprehension of these effects is vital when predicting the influence of changing climate on species and human societies. It is also crucial for the successful management and conservation of global forests and the ecosystem services they provide.

This work focuses on methods that lead to a description of forest canopies associated with modelling these regulatory ecosystem services - the ability to modify microclimatic conditions and influence local air quality.

1.2 Research Motivation

In today's world of climate change, environmental degradation, and rapid urban development, the importance of trees is increasingly being discussed. As we enter a public park or a pristine forest, we can feel their uniqueness, especially during the scorching summer heat when the air seems stagnant, and the sun's sharp rays force all living organisms to seek shelter from the heat. At such times, the shade, coolness, refreshing humidity, and uplifting scent of essential oils under the treetops provide natural refuge.

These fascinating phenomena inspired me to contemplate the function of forests and vegetation. In my bachelor's and diploma thesis, I focused on the regulatory services of forests, particularly their impact on accumulation and erosion processes. I had the opportunity to understand how tree root systems and grass turf keep topsoil compact, prevent soil erosion, and gully formation. However, this was only one of the many services that forests provide. Fate brought me to the team of Jan Wild, where I had the opportunity to explore the processes of forest climates near the ground, the factors that affect them, and the ecological consequences that ensue.

My underlying motivation for this research was my natural curiosity about understanding the mechanisms of the surrounding world, not to conquer or transform them, but to observe and listen to the secrets of nature humbly and quietly. This also influenced the methods I chose for my research, which were non-destructive and often remotely deployed to assure me that I was penetrating the sanctity of the forest environment only through knowledge and not physical intervention. Moreover, I believe that understanding the internal processes of forests can be a valuable argument for forest preservation, protection, and mutual respect as a place that provides us not only with recreational pleasure but also with a whole range of necessary ecosystem functions. I hope to have contributed, at least partially, to this cause.

1.3 Thesis Structure

The thesis is divided into two parts and ten chapters. The **Part I** provides a theoretical background and brief introduction to selected elements of forest microclimate, and reviews related vegetation parameters and their derivation from indirect techniques. The **Part II** consists of three published studies and one manuscript and discusses their interrelation and contribution to forest canopy science. The studies are listed in the following order:

- **Study I:** Ecologically relevant canopy openness from hemispherical photographs.

- **Study II:** Temperature buffering in temperate forests: Comparing microclimate models based on ground measurements with active and passive remote sensing.

- **Study III:** Unmanned Aerial Systems to modelling air pollution removal by urban greenery.

- **Study IV:** From orbit to forest understorey: Spatial-temporal relationships between the canopy surface temperature and air and soil temperatures in the forest interior.

Chapter 2

Objectives of the Thesis

The aim of the thesis is to advance indirect, proximal and remote sensing (RS) methods in the quantification of tree canopy structures in relation to forest microclimate modelling. The relationship between forest structure and microclimatic conditions under the forest canopy is investigated using hemispherical photography (HP), unmanned aerial systems (UAS) and satellite products and in situ measured radiation and meteorological properties.

Specifically, papers reported here: **1)** explore how canopy openness calculated from different angles of view of HP controls air and soil temperature and photosynthetically active radiation in understories of deciduous broadleaved forests; **2)** compare the influence of the canopy cover and height inferred from the HP and passive and active sensors onboard UAS as predictors of air and soil temperature offsets (i.e. differences between the forest understorey and treeless areas); **3)** demonstrate how UAS-derived canopy structure parameters may be incorporated into mechanistic models of dry deposition and thus enable to reveal spatial heterogeneity of air pollution removal rates among various species and life stages of woody plants; and **4)** quantify seasonal and daily differences between temperatures on the surface of forest canopy inferred by MODIS satellite products and air and soil temperatures measured in various vertical strata below forest canopy.

Chapter 3

Theoretical Background

3.1 Introduction

Traditionally, the climate, or macroclimate, is described by meteorological variables measured standardly at a height of about $1.5 - 2$ m (10 m for wind speed) (Barry and Blanken 2016). However, in a forest environment, conditions change rapidly in the air layer below forest canopies that act as a semi-permeable membrane creating specific fine-scale climate variations, generally understood as microclimate (Geiger et al. 1995).

Microclimate has been interpreted in various ways depending on the discipline and context (Barry and Blanken 2016, Geiger et al. 1995, Orlanski 1975). In this thesis, microclimate will be considered to typically have a spatial resolution below 100 m, and vertically range from near ground to the treetops.

Classic approaches are inadequate for describing such variable conditions in complex environments and it is necessary to apply novel methods. While the existing network of microclimate sensors mounted on fixed towers, canopy cranes, or on the ground is geographically sparse and provides only point-based information (Lembrechts et al. 2020, Nakamura et al. 2017, Lowman 2021), standardized weather stations characterize rather long-term free-air conditions (Potter et al. 2013). Approaches that would effectively interpolate field-based microclimate

measurements or downscale macroclimatic information are, therefore, required.

Mapping microclimate heterogeneity over time at large spatial scales can potentially be achieved indirectly, based on an empirical relationship with the governing properties of tree canopies (Zellweger et al. 2019b). A potential solution could lie in the methods of remote and proximal (e.g., ground-based) sensing of vegetation characteristics, i.e., techniques for the acquisition of information about biophysical properties of objects without direct physical contact (Bréda 2003, Gower et al. 1999, Jonckheere et al. 2004). Such contactless measurement is generally faster, amenable to automation and hereby suitable for larger spatial and temporal sampling. Hereinafter, such methods will be referred to as indirect.

In this thesis, I specifically focused on two indirect techniques: 1) in situ HP for understanding the structural drivers of understorey microclimate and providing auxiliary data for 2) passive and active RS that offers opportunities to produce detailed and spatially continuous data layers, which can serve as explanatory variables for modelling of the horizontal and vertical variation in microclimatic conditions over large spatial and temporal scales.

3.2 Selected elements of the forest microclimate

The physical obstacles represented by leaves, tree crowns and branches influence the flow of energy and substances between the internal environment of the forest and the free atmosphere above. The forest canopy structure, generally defined as the three-dimensional distribution of trees' structural elements (Pan et al. 2013), modifies primarily the four components of the energy budget in the forest understorey (Geiger et al. 1995). In the estimated order of their importance, these processes are

as follows: 1) solar and thermal radiation, 2) latent-heat exchange, 3) sensible heat flux (heat convection), and 4) heat conduction (Bramer et al. 2018, Geiger et al. 1995). Hence, the forest canopy fundamentally reshapes the prevailing character of the local climate and establishes specific microclimatic conditions, which subsequently affect the diversity and productivity of forest communities (Nakamura et al. 2017). In the following sections, canopy effects on some microclimate conditions relevant to the papers included in this thesis will be briefly specified.

3.2.1 Transmitting radiation and light availability

The main ability of the canopy is to reflect, scatter and absorb incoming solar radiation (Geiger et al. 1995). During clear and warm days, much of the incoming shortwave solar radiation is absorbed and reflected by the canopy.

When short-wave solar radiation hits the treetops, part of the electromagnetic radiation (up to 30 %) is reflected back into the atmosphere (Barry and Blanken 2016). The proportion varies depending on canopy albedo driven in part by species composition, with coniferous forests achieving generally lower reflectance compared to mixed or deciduous trees (Davidson and Wang 2004, Kuusinen et al. 2014b). In addition, however, different albedo values occur even within the same species group (Hovi et al. 2016), and vary depending on the canopy structure and crown morphology.

A certain proportion of the solar spectrum is further absorbed by the assimilation organs of the tree canopy (Geiger et al. 1995). During the growing season, photosynthetically active radiation (PAR) in the wavelength range of 0.4 – 0.7 µm is used for the needs of photosynthesis (Barry and Blanken 2016).

The amount of the remaining solar radiation transmitted into forest undergrowth generally decreases with increasing canopy quantity

(Fig. 3.1). Solar radiation passing through the canopy subsequently constitutes one of the main components of the energy and the heat balance of the forest's internal environment. Compared to non-forest areas, however, this component is significantly reduced to only short-lasting sunflecks (Chazdon and Pearcy 1991), which plays an important role as a limiting ecological factor for the plants and other organisms living in the forest understorey (Canham et al. 1990, Tinya et al. 2009). Depending on the vertical and horizontal structure of forest canopies (e.g., the distance to the forest edge, canopy gaps, tree height distribution, leaf clumping), they can block over 95 % of visible light from reaching the Earth's surface (Bonan 2008, Geiger et al. 1995, Davies-Colley et al. 2000).
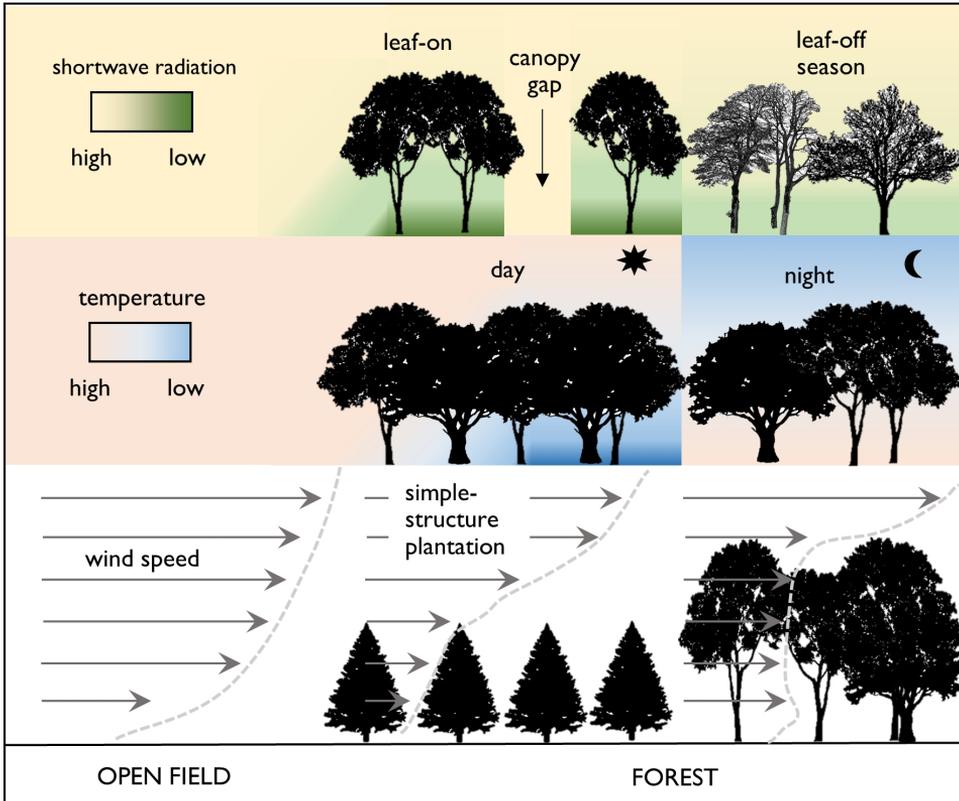
Figure 3.1: Short-wave radiation, temperature, and wind speed gradients in open areas and within forest canopies. Modified from De Frenne et al. (2021), Geiger et al. (1995).

3.2.2 Temperature buffering

The main microclimatic manifestation of the tree canopy lies in its ability to buffer temperature extremes and reduce the diurnal, seasonal and interannual variability of air and soil temperatures in the forest understorey (Geiger et al. 1995).

The limited amount of penetrating solar radiation, the cooling effect of transpiration and less intensive air mixing (Geiger et al. 1995, Monin and Obukhov 1954) reduce the daily temperature maxima in the understorey by up to several degrees compared to the adjacent treeless areas (Von Arx et al. 2012, Konarska et al. 2016, Meili et al. 2021). This buffering phenomenon peaks in the late afternoon hours (Meili et al. 2021) and is particularly pronounced in deciduous stands during warm and cloud-free summer days (Von Arx et al. 2012, Von Arx et al. 2013).

Conversely, this relationship is reversed at night-time and early morning, where the canopy generally increases the understorey temperature minima as it shields longwave radiation outgoing from the Earth (De Frenne et al. 2019, Geiger et al. 1995). However, the warming effect varies depending on the weather situation and canopy structure. Generally, compared to the effect on the daily maxima, the buffering of temperature minima tends to be of lower magnitude or even marginal (Von Arx et al. 2012). Distribution of such temperature differences and microclimate gradients varies also within a forest as a function of the distance from the forest edge and treetops (Geiger et al. 1995, Suggitt et al. 2011). Depending on the density of the canopy (Fig. 3.1) and on the intensity of turbulent air mixing, understorey temperatures are usually continuously dampened towards the forest floor on clear days (De Frenne et al. 2021). While in sparser canopies, where the whole air mass of the forest is affected and temperature is more evenly distributed, denser canopies slow down the penetration of the radiation, which increases the temperature differences between

the treetops and the forest floor (Geiger et al. 1995). Similarly, dense canopies increase the horizontal temperature gradient with the growing distance from the forest edge towards the forest core (Chen et al. 1993).

Overall, the forest canopy, combined with the effect of understorey vegetation (Stickley and Fraterrigo 2021), moderates daily and seasonal temperature variation relative to free-air conditions, with the greatest difference being observed near the ground in forest cores (De Frenne et al. 2019, Geiger et al. 1995). The moderating capacity is generally larger in summer than in winter (Von Arx et al. 2012), and further increases as ambient temperatures become more extreme (De Frenne et al. 2019). However, understorey temperature buffering is a more complex and interconnected mechanism that is influenced, among other things, by wind speed (Huang et al. 2015), topography (Macek et al. 2019), and the availability of soil water and atmospheric moisture (Davis et al. 2019).

3.2.3 Wind attenuation

The forest canopy does not only act as a barrier to energy exchange, it also effectively reduces the turbulent mixing of air through decreased wind speeds flow (Fig. 3.1). Due to the increased surface roughness and higher friction at the tops of trees or in forest edges, wind is blocked and slowing down towards the forest interior (Geiger et al. 1995). The typical vertical wind speed profile inside forests shows a significant wind attenuation in the treetops and, if winds are strong and the shrub layer is absent, a secondary wind speed maximum in the branch-free trunk area, where the fraction velocity is lower (Geiger et al. 1995). The dense and high canopies not only prevent the penetration of vertical air movement; they also limit its horizontal movement and turbulent air mixing (Chen et al. 1993). The extent to which the wind can penetrate the forest understorey or the forest core depends, besides canopy properties, also on other factors, such as the external wind speed

(Chen et al. 1993, Huang et al. 2015), the edge orientation (Hylander 2005), or the wind direction (Davies-Colley et al. 2000).

Wind speed in a forest environment determines various processes, such as the fluxes of energy and trace gases (e.g., CO_2, H_2O, O_3) (Turnipseed et al. 2009, Greco and Baldocchi 1996, Baldocchi et al. 1987). The interaction between the wind flow and canopy characteristics influences the aerodynamic dispersion (Tiwari et al. 2019) as well as dry deposition fluxes of atmospheric particles (Zhang et al. 2001) and gases (Emberson et al. 2001). Thus, the canopy drives not only physical microclimatic properties but also the chemical composition and air quality.

3.3 Microclimate-related vegetation parameters and their determination by indirect methods

As outlined in the previous chapter, the forest canopies fundamentally drive the understorey microclimate. In the following sections, I review some of the key vegetation determinants of the forest microclimate and describe how such characteristics can be derived from indirect methods. In doing so, attention will be specifically paid to HP, thermal sensing, photogrammetry, and laser-scanning, i.e. methods used in the attached studies (**Part II**).

3.3.1 Canopy reflectance

Canopy reflectance determines the energy and radiation balances at the top of the canopy, i.e. the extent to which sunlight heats these surfaces. It is, therefore, an important factor in forest microclimate modelling (Maclean and Klinges 2021).

Most commonly, this parameter is quantified by surface albedo, defined as the fraction of solar irradiance reflected by the canopy surface over the complete solar spectrum (Dickinson 1983). Traditionally, the measurement of surface canopy albedo has been based on simultaneous direct measurements with upward-facing and downward-facing pyranometers installed on cranes or towers (Kuusinen et al. 2012). Miniaturized versions of such pyranometers have recently been also mounted on UAS (Levy et al. 2018).

Alternatively, surface albedo can be derived from the shortwave interval (comprising the visible and near-infrared domains only) detected by passive satellite RS (Pinker 1985). Data products derived over large scales are commonly provided from the MODIS (Schaaf et al. 2002, Wang et al. 2014) and LANDSAT campaigns (He et al. 2018, Kuusinen et al. 2014a, Wang et al. 2016), or other RS platforms for higher-resolution imaging (Franch et al. 2018).

However, these canopy albedo estimations are sometimes biased, particularly by the presence of snow or within-canopy shadowing. Forest albedo determination can be improved, for instance, by using high-resolution, properly timed UAS sensing (Cao et al. 2018, Levy et al. 2018) or by using auxiliary RS vegetation parameters (Alibakhshi et al. 2020, Lukeš et al. 2014, Hovi et al. 2016, Kuusinen et al. 2014b).

Additionally, canopy reflectance recorded from multispectral and hyperspectral airborne and space-borne sensors provides information on the functional traits of the vegetation and phenological differences that may also be related to microclimatic gradients. For instance, the light regime beneath the forest canopies varies depending on leaf properties and tree species (Canham et al. 1994), leading to species-specific microclimatic conditions in the understorey (Asner et al. 2015). Vegetation spectral indices (e.g. NDVI, NDWI, EVI) retrieved from these platforms may constitute an easily available substitution for canopy structure variables (Carlson and Ripley 1997) and, thus, serve as satisfactory predictors for modelling forest microclimate

temperature data in large-scale analyses (Haesen et al. 2021).

3.3.2   Canopy surface temperature

Forest microclimate is further determined by heat conductance and temperature at the canopy surface (Maclean and Klinges 2021), commonly inferred from land surface temperature (LST), which can be derived from long-wave infrared radiation emitted by the canopy layer in the spectral range of 7.5 to 14 µm (Tomlinson et al. 2011).

To retrieve LST across a small scale, a thermal camera has been used in the field to explore canopy temperature distribution among different tree species (Leuzinger and Körner 2007) or to demonstrate the differences in microhabitat temperatures between the soil and LST (Scherrer and Koerner 2010). This approach is becoming more available with the advent of handheld thermal infrared recorders (Su et al. 2020) and easy-to-use devices that can be attached to a smartphone (García-Tejero et al. 2018). However, images from these cameras have to be treated appropriately, taking into account, for instance, the object emissivity and distance to the target, device-specific wavelength spectrum and data calibration (Bramer et al. 2018).

Another long-established approach uses a thermal camera mounted on satellite platforms, such as, for example, Landsat (Jiménez-Muñoz et al. 2014), Sentinel (Sobrino et al. 2016), or MODIS (Neteler 2010) missions. Satellite-derived LSTs were already tested to create a time series of global monthly surface temperatures (Metz et al. 2017) or daily average temperatures in the forest understorey (Laskin et al. 2017). While this satellite-borne RS method is effective, it suffers from low spatial or temporal resolution and is regularly hampered by clouds and other atmospheric disturbances, especially in mountainous regions (Neteler 2010).

Greater potential, therefore, lies in very high-resolution sensors installed on aircraft (Hesslerová et al. 2013) or UAS (Faye et al. 2016, Cheung

et al. 2021). Operating at lower altitudes, these RS techniques have already brought the resolution of the images closer to the range usable for monitoring microscale processes (Maclean et al. 2017). On the other hand, acquired data usually provide only short-term information unique for the moment of acquisition, which cannot capture the ecologically relevant microclimate in its complexity (Körner and Hiltbrunner 2018). Furthermore, radiation detected by a thermal camera does not reflect only the emitted energy of the scanned object, but also the radiation emitted from surrounding sources, i.e., from the atmosphere or external optics (Bramer et al. 2018).

However, even with repeated thermal data acquisition and its appropriate calibration and processing (Döpper et al. 2020), the fundamental problem remains that the measured values correspond only to temperatures on canopy surfaces, whereas conditions below the canopy remain out of view. For these reasons, RS-inferred surface thermal reflectance is a valuable source of information; for modelling the microclimate heterogeneity within the forest interior, it must, however, be supplemented with the properties of canopy architecture (Jiang and Weng 2017).

3.3.3 Canopy height

In addition to the surface radiative properties, below-canopy microclimatic conditions can be approximated using detailed 3D vegetation structure characteristics, with canopy height being one of the most important parameters (Maclean and Klinges 2021).

Canopy height has a significant effect on the forest microclimate in several ways. First, it regulates how much radiation is attenuated at any given height. Taller canopies effectively modulate the amount of penetrating solar radiation and ultimately reduce near-ground air temperature and moisture content in the understorey (Frey et al. 2016, Von Arx et al. 2013, Smith-Tripp et al. 2022).

Secondly, canopy height can be used as a reasonable proxy variable for surface roughness parameters (Tian et al. 2011, Raupach 1994, Trepekli and Friborg 2021), which govern the momentum exchange and wind speed profile (Campbell 1986) and which are usually difficult to measure directly (Shaw and Pereira 1982).

For indirect estimation of canopy height in the field, small hand-held clinometers applying trigonometrical principles are traditionally used. Contemporary methods of tree height determination are based mostly either on analogue clinometers (Hall et al. 2005), laser rangefinders (Asner et al. 2002), or ultrasound hypsometers (Macfarlane et al. 2010).

As an alternative, light detection and ranging (LiDAR) is a rather recent, but increasingly popular indirect technique for forest inventory (Maltamo et al. 2014). It is based on emitting and scanning high-rate laser pulses sent and received at known positions. Based on the time-of-flight principle, it is then possible to calculate the coordinates of reflecting objects (Lovell et al. 2003). Dense point clouds generated from ground-based (terrestrial) LiDAR can be then used for detailed quantification of canopy height and other forest structure variables (Popescu and Wynne 2004, Evans et al. 2006) of individual trees but not continuously across the landscape scale, being rather spatially restricted to small areas (Liang et al. 2016).

For landscape-scale analysis, LiDAR sensors for canopy height data acquisition can be mounted on aircraft (Alexander et al. 2013, Hyyppa et al. 2001, Moudrý et al. 2023a, Naesset 1997), or, recently, also on UAS (Kuželka et al. 2020, Kellner et al. 2019, Hyyppä et al. 2020). In the case of airborne LiDAR, canopy height is calculated from the first (treetop reflection) and last (ground-level reflection) pulses.

Other airborne and UAS-based techniques for deriving canopy height data involve ranging radar (Hyyppä and Hallikainen 1996) or photogrammetry (Gruen 2012, Ginzler and Hobi 2015). Particularly, the automated photogrammetric algorithm Structure from Motion

(SfM) for matching features across overlapped images and constructing orthophoto mosaics and 3D models (Snavely et al. 2008) has been increasingly used as a cost-effective alternative to LiDAR (Wallace et al. 2016).

On a global scale, recent progress towards creating a planetary forest canopy height map has been made possible by space-borne synthetic aperture radar (SAR) (Chen et al. 2016) or laser scanning programs such as Ice, Cloud, and land Elevation Satellite-2 (ICESat-2; Li et al. (2020), Popescu et al. (2018)) and Global Ecosystem Dynamics Investigator (GEDI; Potapov et al. (2021)).

3.3.4   Canopy density

Forest microclimate is further affected by canopy density. Canopy structure, vertical and horizontal distribution, and the volume of above-ground biomass determine the amount of penetrating light (Campbell 1986), air movement, and ultimately, understorey air and soil humidity and temperature (Geiger et al. 1995). Therefore, the canopy structure can be used as a proxy for mapping associated microclimate variables within and below the canopy (Frey et al. 2016, Greiser et al. 2018, Jucker et al. 2018, Hardwick et al. 2015).

Canopy structure has been estimated by several volumetric indicators, the most common being canopy density (Latifi et al. 2016), canopy cover/gap fraction (Leblanc et al. 2005), canopy closure/openness (Jennings et al. 1999), or the leaf area index (LAI) (Chen and Black 1992, Watson 1947). Principally, all these indicators express a proportion of canopy surfaces per unit of ground area, differing in ways of quantification and in a segment (point-base, vertical projection) over which such information is integrated (Jennings et al. 1999, Woodgate et al. 2015).

Ground-based indirect methods represent one of the possible approaches. They can be classified into two main categories: active sensing, which

uses data from a terrestrial LiDAR (Evans et al. 2006), and optical methods based on the measurement or estimation of light transmission through canopies. Optical methods implement the Beer-Lambert law assuming that the total amount of radiation intercepted by a canopy layer depends on incident irradiance, optical properties, and canopy structure (Monsi and Saeki 1953).

Several optical methods have been proposed and used (Jonckheere et al. 2004). The most common instruments involve line quantum sensors (Pierce and Running 1988) for measuring direct beam transmission (DEMON, TRAC; Chen et al. (1997)) and diffuse radiation (LAI-2000 Plant Canopy Analyzer; Stenberg et al. (1994)). Alternatively, canopy image analysis techniques can be employed, using images acquired by cover photography (Chianucci and Cutini 2013) as well as hemispherical upward- (from beneath the canopy) or downward-looking (placed above the canopy) photography (Fournier and Hall 2017, Rich 1990).

Deriving canopy architecture from one or (usually) several hemispherical photographs is a widely used, valuable, and cheap technique (Leblanc et al. 2005, Jonckheere et al. 2004). It derives the gap fraction distribution from the binary black-and-white RGB (Red-Green-Blue) (Frazer et al. 2000) or near infra-red (Chapman 2007) imageries as a portion of the open sky unobstructed by canopy elements calculated for different zenith and azimuth angles (Jonckheere et al. 2005). It enables more efficient sampling than linear sensors (Welles and Norman 1991), especially when sunshine is too scarce to allow work with the transmission of a direct beam.

Although in situ indirect methods for canopy structure determination are a respected data source in forest inventory, they are usually only point-based and, therefore, spatially limited. In addition, their acquisition and processing are time-consuming and almost unfeasible for large areas. Nevertheless, in situ measurements remain an essential component for the calibration or validation of RS data (Woodgate et al. 2015, Pfeifer et al. 2012) that can, in turn, accurately assess the 3D

canopy structure over larger scales and support the advancement in microclimate research (Zellweger et al. 2019b).

In this respect, the recent surge of airborne and UAS-mounted LiDAR sensors generates many useful datasets and tools. For instance, these techniques provide contiguous and highly detailed datasets on horizontal and vertical canopy structures that can be used to map and parameterize principal ecological phenomena and provide crucial input data to microclimate modelling (Frey et al. 2016, Greiser et al. 2018). Alternatively, UAS-SfM can also produce suitable high-resolution data on canopy structure and heterogeneity that are scale-appropriate for providing new and affordable microclimate insights (Duffy et al. 2021).

The latest addition to the data collection methods is represented by satellite- or spacecraft-borne RS techniques that have estimated forest structure over a range of biogeographic gradients, using both passive optical sensors (Foody 2003) and active sensors, such as SAR (Mitchard et al. 2009), or LiDAR (Mitchard et al. 2012). Each of these technologies has naturally its strengths and weaknesses for mapping canopy structural variables. Nevertheless, especially LiDAR measurements of vertical forest structure are very promising (Hakkenberg et al. 2023). At present, however, the GEDI mission, specifically designed for this purpose, does not by itself provide spatially continuous maps. Unlike gridded imagery, the GEDI's sampling scheme records height measurements in spatially discrete (around 25 m) footprints and the interstitial areas remain unsampled (Duncanson et al. 2022).

The GEDI's discontinuous sampling scheme can be mitigated by statistically aggregating (Dubayah et al. 2022) or interpolating the structural characteristics between GEDI footprints using continuous ancillary satellite RS datasets (Potapov et al. 2021). Multiple factors may, however, influence the accuracy and consistency of maps derived in this way, such as the quality and quantity of LiDAR observations and of ancillary data as well as natural variations in forest structure across ecosystems (Duncanson et al. 2022).

Part II

Research

Chapter 4

Ecologically relevant canopy openness from hemispherical photographs

Lucia Hederová, Martin Macek, Jan Wild, Josef Brůna, **Vít Kašpar**, Tereza Klinerová, Martin Kopecký

Author's contribution: Conceptualization, Methodology, Data Curation, Formal analysis, Investigation, Writing − Original Draft

Abstract

Canopy openness controls forest biodiversity and microclimate. Traditionally, canopy openness was calculated from hemispherical photographs with a 180° angle of view, but photographic equipment providing only narrower angles of view is increasingly used in forest ecology and meteorology. However, it is not known what the predictive ability of the canopy openness calculated from narrower angles of view is, compared to the traditional 180°. To fill this gap, we explore how canopy openness calculated from different angles of view predicts vascular plant species richness and composition, in-situ measured air and soil temperature and photosynthetically active radiation across 115 sites established in three different types of European deciduous broadleaved forests.

Canopy openness calculated from angles of view $< 180°$ was a better predictor of all measured variables than canopy openness from the whole hemispherical photograph. Openness from $80° - 120°$ angle of view best explained plant species richness, community composition, in-situ measured air and soil temperatures, and the photosynthetically active radiation. Moreover, canopy openness from a 100° angle of view predicted all variables except maximum air temperature better than the total radiation site factor. Finally, canopy openness calculated from angles of view $< 120°$ is more comparable between smartphone and specialized cameras than openness from the whole hemispherical photograph.

We found that canopy openness from a complete hemisphere is not required for many ecological applications. Therefore, many consumer-grade cameras and smartphones with an external fisheye lens can provide ecologically relevant canopy openness. Nevertheless, specialized cameras and fisheye lenses should still be preferred even for canopy openness calculation from $< 180°$ angles of view. In summary, ecologists can predict plant assemblages, forest microclimate and understorey light conditions better with canopy openness calculated from angles of view around 100° rather than from the whole hemispherical photograph.

4.1 Introduction

Tree canopies determine the quantity and spectral quality of penetrating solar radiation, which affects air and soil temperature and humidity near the ground (Von Arx et al. 2012). Modified light availability, together with canopy-influenced thermal and moisture microclimates then shapes species diversity, composition and productivity of the forest understorey (Canham et al. 1990, Gravel et al. 2010, Tinya et al. 2009). Two most often used variables capturing canopy effects on understorey light, microclimate, and biodiversity are canopy openness, defined as a fraction of the angular sky area that is unobstructed by vegetation when viewed from a single point and canopy cover, defined as the fraction of unit area covered by vertical projection of the tree crowns (Gonsamo et al. 2013).

Despite its fundamental importance, canopy attributes are still commonly estimated visually during field sampling. However, the visual estimation is subjective and imprecise (Korhonen et al. 2006, Tichý 2016), and is increasingly being replaced by the reproducible calculation of canopy openness from hemispherical photographs acquired by a camera with circular fisheye lens facing upwards (Hill 1924) or by canopy cover estimates from upward facing photographs with very narrow angle of view (Chianucci 2015).

Hemispherical photographs were originally captured with analogue film cameras, but the advance in digital photography facilitated their wider use due to better cost-effeciency (Fournier and Hall 2017). The hemispherical photography have been evaluated in a number of methodological studies and become a standard tool in forest ecology and meteorology. These methodological studies have evaluated differences between canopy openness calculated from analogue and digital hemispherical photographs (Frazer et al. 2001), explored effects of exposure and image resolution (Zhang et al. 2005), developed methods for conversion from colour image to binary canopy/gap image (Chianucci and Cutini 2012,

Glatthorn and Beckschäfer 2014, Nobis 2005) and compared numerical outputs from different programmes used for hemispherical image processing (Fournier and Hall 2017, Jarčuška et al. 2010, Promis et al. 2011).

Wider usage of digital hemispherical photography and the capability of digital image processing facilitated development of various metrics quantifying canopy stuctures (e.g. canopy openness, canopy cover) and understorey radiation regime (e.g. direct-, diffuse-, and total radiation). Among these metrics, canopy openness stands as a robust and intuitive metric that is comparable among different computer programmes and, therefore, across studies (Fournier and Hall 2017). As a result, canopy openness is widely used as a standardized quantitative descriptor of the canopy structure (Chianucci 2020, Fournier and Hall 2017, Gonsamo et al. 2013, Wu et al. 2012).

Canopy openness is routinely calculated as the relative angular area of visible sky from the whole hemisphere − i.e., from an upward-facing hemispherical photograph with a 180° angle of view (AOV, Fig. 4.1). However, areas close to the horizon are more likely obscured by tree trunks and low shrubs because the optical path length penetrating the canopy increases with the zenith angle. Therefore, areas close to the horizon on the hemispherical photograph usually lack canopy gaps, irrespectively of stand density (Gonsamo et al. 2010, Machado and Reich 1999). Higher zenith angles thus usually contribute a little to the total canopy openness and its variability among stands (Bianchi et al. 2017). Moreover, these angles potentially increase the noise in the canopy openness estimates, as optical defects like distortion, loss of sharpness, chromatic aberrations, or vignetting of the fisheye lens tend to be more pronounced at the edge of the image. Further, areas close to the horizon are also affected by topographic shading, which affects the resulting canopy openness when the topographic mask is not applied.
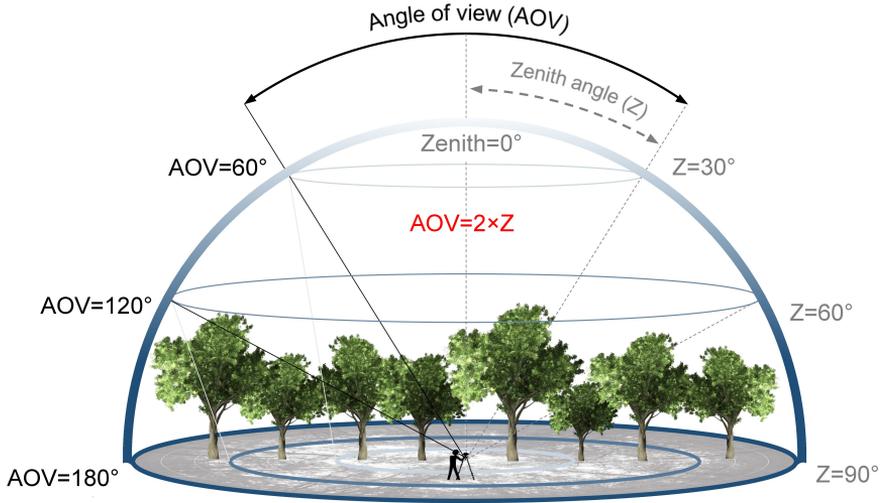
Figure 4.1: The geometry of spherical coordinates associated with the hemispherical photograph. Canopy openness is defined as a proportion of sky visible from a point. Zenith angle (Z) specifies different angles of view (AOV) in the photographs; therefore, AOV=2 × Z. The current standard is to calculate canopy openness from the whole circular hemispherical photograph with the AOV of 180°, but we found that smaller AOVs predict important ecological variables better.

To reduce the influence of areas close to the horizon, canopy openness can be calculated from AOV smaller than 180°, but surprisingly, only a few ecological studies declare such intentional use (Macek et al. 2019, Machado and Reich 1999), and none of them compared the predictive performance of canopy openness calculated from smaller AOV with openness from the 180° AOV. Many studies, however, used smaller AOV unintentionally. For example, hemispherical images are increasingly captured with smartphones equipped with fisheye lenses that do not reach 180° AOV (Bianchi et al. 2017, Davis et al. 2019, Slabejová et al. 2019, Tichý 2016). Widely used LAI-2000/Licor sensor covers only 148° AOV (Chacón and Armesto 2005), and various spherical densiometers cover 80° to 120° AOV, depending on the type (Cook et al. 1995, Lemmon 1956). Finally, an inappropriate combination of fisheye lens and digital camera sensor size (e.g., 8 mm fisheye lens

used on an APS-C camera) produces a cropped image with a AOV of only 120° on the short side of the sensor (Table 4.1).

A number of studies thus use smaller AOV to calculate canopy openness, but it remains unknown how this affects the predictive power of canopy openness and comparability among studies. To fill this knowledge gap, we explored accuracy and the predictive power of canopy openness calculated for sequential sub-sections with AOV ranging from 20° to 180° of the whole hemispherical photograph. To test accuracy of canopy openness estimates at different AOVs, we used artifitial calibration targets with various grid sizes. To test the generality of our results for different applications, we explored the predictive power of canopy openness acquired at variable AOV to multiple response variables, including species richness and composition of understorey vascular plants, in-situ measured air and soil temperatures, and photosynthetically active radiation. We benchmarked the predictive power of canopy openness against the predictive power of radiation site factors calculated from the same hemispherical photographs. Finally, we explored comparability between canopy openness calculated from canopy photographs acquired by DSLR camera and smartphone with an external fisheye lens.

4.2 Material and Methods

4.2.1 Study localities

To explore the ecological relevancy of canopy openness calculated from different AOV, we collected data in three localities, representing different oak-hornbeam forest types typical for a temperate zone of central Europe: thermophilous (49°56'N 14°6'E); acidophilous (50°19'N 15°27'E) and mesophilous (50°30'N 13°55'E). While these localities differed in general environmental settings (Appendix A), the tree species

Table 4.1: Overview of selected lenses with different projection (lens type) combined with full-frame and crop sensor type camera and their resulting diagonal and vertical angle of view (AOV). Combinations of lenses and sensors which provide vertical AOV ≥ 100° are highlighted in grey. According to our results, AOV ≥ 100° is sufficient for many ecological applications.

Lens type*/Lens	Full Frame		Crop sensor) (APS-C or micro 4/3)	
	Vertical AOV	Diagonal AOV**	Vertical AOV	Diagonal AOV
Wide-angle (Rectilinear):				
Samyang XP 10mm f/3.5	100°	130°	77°	110°
Nikon AF-P DX 10-20mm f/4.5-5.6G VR	85°	118°	77°	110°
Laowa 7.5mm f/2 Micro - Micro 4/3	–	–	77°	110°
Fisheye (Circular):				
Sigma 8mm f/3.5 EX DG	180°	180°	120°	180°
Sigma 4.5mm f/2.8 EX DC	180°	180°	180°	180°
Laowa 4mm f/2.8	210°	210°	210°	210°
Meike 6.5mm f/2 MC	190°	190°	–	190°
Fisheye (Diagonal):				
Samyang 12mm f/2.8 ED AS NCS Fisheye	100°	180°	72°	124°
Sigma 15mm f/2.8 EX DG	94°	180°	58°	113°
Canon 15mm f/2.8	91°	180°	58°	107°
Sony 16mm f/2.8 Fisheye	91°	180°	58°	110°
Zenitar 16mm f/2.8 Fisheye	90°	180°	60°	120°
Nikon 16mm f/2.8D AF	100°	180°	58°	107°
Nikon 10.5mm f/2.8G ED AF DX	–	–	89°	180°

* Relation between distance from image center and an angle from optical axis differs between lens types. This affects not only the calculation of AOV, but it implies that each pixel on the image represents a different angular area of the hemisphere (with the exception of equisolid fisheye lenses). Canopy openness can also be estimated by other than circular fisheye lenses (e.g., rectilinear lenses or full-frame fisheye lenses). The crucial point is to correct lens distortion using a proper projection function during image processing to recalculate the image area correctly to the spherical area. ** Lens manufacturers usually provide diagonal AOV, but for ecological applications, vertical AOV is the limiting. Besides lens optical properties, the size of the camera sensor also influences the resulting AOV. Lenses designated primarily for use with full-frame cameras can be used also on cameras with a smaller APS-C sensor, producing a cropped image with reduced AOV (see also Fig. 4.5).

composition was comparable. The dominant tree species were *Quercus petraea*, *Q. robur* and *Carpinus betulus* with admixed *Tilia platyphyllos*, *T. cordata*, *Fagus sylvatica* and less frequently with *Fraxinus excelsior* and *Acer campestre*, *A. platanoides*, *A. pseudoplatanus*. Tree heights ranged from 10 to 30 m.

Our dataset included 37 sampling sites in the thermophilous forest, 39 sites in the acidophilous forest, and 39 sites in the mesophilous forest. All sites were on flat terrain (slope $0-7°$), more than 15 m from the nearest forest edge and more than 30 m apart from each other. Thus, forest structure differed among sites, but other environmental conditions were comparable (Appendix A).

4.2.2 Field data

On each sampling site, we 1) captured hemispherical photograph, 2) measured air, and soil temperature and photosynthetically active radiation (PAR), and 3) recorded plant species composition in two nested vegetation plots centred on the microclimate logger.

4.2.2.1 Canopy sensing

In this study, we compared six algorithms implemented in two open source and three commercial software products that have been increasingly used for ground point classification (Table 4.1).

Following common practice (e.g., Chianucci 2020), we captured three hemispherical photographs at each sampling site on days with overcast skies during the peak of the growing season with fully developed canopy foliage (July in our study region). To simultaneously capture three photographs with different exposure, we used exposure bracketing $(+0.33, -0.66, -1.66$ EV) with the centre-weighted exposure mode (Zhang et al. 2005). We used a digital single-lens reflex (DSLR) camera Canon 40D with a Sigma 4.5mm f/2.8 EX DC Circular Fisheye lens

mounted on a monopod at 1 m height directly above a microclimate logger defining the sampling site. The lens axis was aimed towards the zenith using a two-axis bubble level, and the top of the camera was directed to the north using a magnetic compass. Known camera orientation is needed for subsequent calculation of radiation indices like direct, indirect and total site factors (Anderson 1966).

From the three photographs captured at each sampling site, we selected an image with the best contrast between the canopy and the sky, i.e. the image with the least amount of saturated (overexposed) or completely black (underexposed) pixels (Hale et al. 2009). For each sampling site, we calculated canopy openness from the selected hemispherical photograph with the best contrast. To further enhance the contrast between sky and canopy, we converted RGB photographs to grayscale images with channels weighted as follows: red 100 %, green −100 %, and blue 200 % in Adobe Photoshop CS6 (Chianucci and Macek 2022).

Subsequently, we classified grayscale images into black (canopy) and white (sky) bitmaps, using the automatic thresholding function based on the edge detection algorithm in the Sidelook 1.1 (Nobis 2005, Nobis and Hunziker 2005). In a few cases when the sky was not uniformly overcast, the automatic thresholding misclassified a part of the sky pixels as canopy pixels; these images were manually edited before further processing.

Each classified photograph was analyzed in the WinSCANOPY (Regent Instruments, S.te-Foy, Quebec, Canada), using the lens-specific corrections for lens projection geometry and nine sky zenith rings. We calculated canopy openness (sky area unobstructed by vegetation divided by a total sky area for a given AOV) from the whole hemisphere (AOV 180°) as well as from subsequently smaller parts of the photograph, using AOV of 20°, 40°, 60°, 80°, 100°, 120°, 140° and 160° (Fig. 4.2).

To determine the radiation indices, we calculated the direct site factor

(the proportion of direct solar radiation penetrating forest canopy), indirect site factor (the proportion of diffuse radiation penetrating forest canopy) and total site factor (sum of direct and indirect site factors). Site factors present the proportion of incident solar radiation at a given site compared to the total incident solar radiation in the open calculated over the same period (Anderson 1966). The calculation of site factors, therefore, requires a whole hemispherical photograph, site geographical coordinates, time zone and time period. To calculate site factors, we used default radiation parameters in WinSCANOPY: 0.6 atmospheric transmissivity, 0.15 diffuse radiation fraction and the standard overcast sky model for diffuse radiation distribution (Anderson 1971). We calculated site factors over the growing season with fully developed foliage in the forest canopy (from the 1st of May to the 30th of September).

4.2.2.2 Plant species composition

To assess the relevancy of canopy openness calculated for different AOVs for understorey plant communities, we recorded plant species composition at each sampling site within two nested circular plots centred on the microclimate logger. We sampled vegetation in two nested plots in order to explore whether our results were scale-dependent, and we recorded plant species composition simultaneously with canopy photography in order to capture plant assemblages growing under fully developed canopy foliage. We recorded the presence of all vascular plant species growing in the smaller circular plot (3.14 m^2), and we also estimated the percentage cover of each species growing in the larger circular plot (100 m^2).

4.2.2.3 Microclimate temperature

At every site, we continuously measured air temperature 15 cm above the ground and soil temperature 8 cm below ground every 15 minutes with a Tomst TMS-4 logger (Wild et al. 2019). After downloading, all

temperature measurements were checked for possible errors and then processed to obtain two temperature variables summarizing ecologically relevant temperatures during the growing season (from May to September; Appendix A): (1) the 95th percentile of daily maximum air temperatures, which provides information about temperature extremes, relevant for plant species composition in temperate forest understorey (Macek et al. 2019) and (2) the mean soil temperatures as a determining factor for belowground processes, including root growth, respiration and decomposition (Körner and Paulsen 2004).

4.2.2.4   Photosynthetically active radiation

We measured photosynthetically active radiation (PAR) reaching forest understorey with Minikin QTi loggers (EMS, Brno, Czech Republic). The loggers measured PAR (µmol/m²/sec) every 10 seconds and stored average PAR values in one-minute intervals. At every site, we measured PAR directly above the TMS microclimate logger at height of one meter above the ground during one day at the peak of the growing season (Appendix A). Within each forest type, all PAR measurements were performed under similar weather conditions.

As a proxy of the above-canopy light availability, we also measured PAR simultaneously in a nearby non-forest area (Anderson 1966). Finally, we calculated the relative PAR availability in the understorey as the mean value of the ratios between PAR values measured at the sampling site and reference PAR values simultaneously measured in the non-forest area (Anderson 1966).

4.2.3   Data analyses

We used linear regression to analyze univariate relations between metrics of canopy structure (i.e. canopy openness and radiation site factors) and species richness, air and soil temperature, and PAR. To account

for the differences among the three studied forest types, we standardized the data before the analyses. Specifically, we centred canopy openness, site factors, temperature, and PAR values within forest types by subtracting a mean value for each forest type. To standardize species richness (i.e. the number of the species growing in the plot) for different species pools in each forest type, we divided the species richness of each plot by the mean species richness in the same forest type. To calculate the variation in species richness, temperature, and PAR explained by canopy openness and site factors, we used an ordinary least-square regression in R, version 3.4.2 (R Core Team, 2018). To quantify the relationship between canopy openness from different AOV and site factors, we calculated Pearson correlation coefficients on standardized variables.

To calculate the variation in species composition explained by canopy openness, we used distance-based Redundancy Analysis − dbRDA (McArdle and Anderson 2001), implemented with *dbrda* function from the *vegan* R-package (Oksanen et al. 2013). From the presence-absence data collected in 3.14 m^2 vegetation plots, we calculated compositional differences as Sørensen dissimilarity (Legendre and Legendre 2012). From species cover data collected in 100 m^2 vegetation plots, we calculated compositional differences as Bray-Curtis dissimilarity derived from square-rooted species percentage cover values (Legendre and Legendre 2012).

Compositional variation explained by a multivariate analysis depends on dataset heterogeneity, and it is not comparable among different datasets (Økland 1999). Therefore, we express variation in species composition explained by canopy openness relative to the maximum compositional variation that can be theoretically explained in the same multivariate analysis. To calculate this relative importance, we divided the variation explained by each version of canopy openness by the maximum variation that can be potentially explained by the single predictor in the same multivariate analysis (Macek et al. 2019). To calculate this maximum explainable variation, we used the sample scores from

the first ordination axis of the Principal Coordinates Analysis as a single explanatory variable in dbRDA calculated with the same species composition dissimilarity matrix (Sørensen for smaller plots, Bray-Curtis for larger plots).

To assess the robustness of our results, we calculated uncertainty in the variability explained by canopy openness and site factors for each studied variable. Specifically, we used bootstrap with replacement to randomly sample 1000 subsamples from our dataset. Then we recalculated variability explained by canopy openness calculated with different angles of view and site factors for each random subsample. Finally, we presented the uncertainty of the explained variability as 66 % and 95 % highest density intervals calculated using *ggdist* R package (Kay 2020).

4.2.4   Hemispherical image calibration

To evaluate the accuracy of canopy openness calculated from hemispherical photographs at different AOVs, we used artificial calibration hemispheres with a known proportion of black and white fields (Chianucci 2015). We used three calibration hemispheres (r = 19 cm) with checkerboard pattern with different grid sizes (square side of 3.1 mm, 9 mm, and 19.8 mm; equalling to spherical angle of 0.94°, 2.73° and 6°, or 0.004 %, 0.036 % and 0.175 % of the total hemisphere area, respectively, Appendix B). Hemispherical photographs of calibration hemispheres were taken following the protocol for hemispherical image exposure (underexposure −2 EV, f = 6.3, ISO 400) with lens front element centered at the equatorial plane. Since these photographs of calibration hemisphere have no green foliage to be distinguished, we used only the blue channel for image binarization. Next, we calculated the proportion of white pixels (gap fraction) for separate 10° zenith rings and compared it to the expected true value (i.e. 50 %). We performed this calibration for Sigma 4.5mm f/2.8 EX DC Circular Fisheye lens on Canon 40D DSLR camera. The same procedure was repeated using

smartphone photography using ASUS Zenphone 3 with 180° convertor
to explore the ability of inexpensive smartphone solutions to replace
DSLR cameras in hemispherical photography.

Finally, we evaluated the potential of canopy openness calculation from
photographs captured with a smartphone with the external fisheye
lens convertor in the field conditions (Appendix C). Specifically, we
calculated the correlation between the canopy openness from the corre-
sponding AOV between hemispherical photographs from DSLR camera
and smartphone with the external fisheye lens.

4.3   Results

Canopy openness and its variability among sites decreased with in-
creasing AOV (Fig. 4.2). Canopy openness calculated at 180° AOV
consistently resulted at lowest values (Fig. 4.2). At 180° AOV, mean
canopy openness across all sites was 4.4 %, lowest openness 1.2 % and
highest openness only 9.4 %.

The best predictive power of canopy openness for plant species as-
semblages, understorey temperature, and PAR was achieved at AOV
narrower than 180° (Fig. 4.3). Canopy openness calculated from 100°or
120° AOV performed best for explaining plant species at both vege-
tation plot sizes, as well as for maximum air temperature and mean
soil temperature during the growing season. For understorey PAR and
species composition at both vegetation plot sizes, the best fit with
canopy openness was detected at 80° AOV, with the explained vari-
ation substantially higher than the variation explained by openness
from the whole hemisphere.

The predictive power of canopy openness from narrower angles was
comparable to the indirect site factor and higher than direct and total
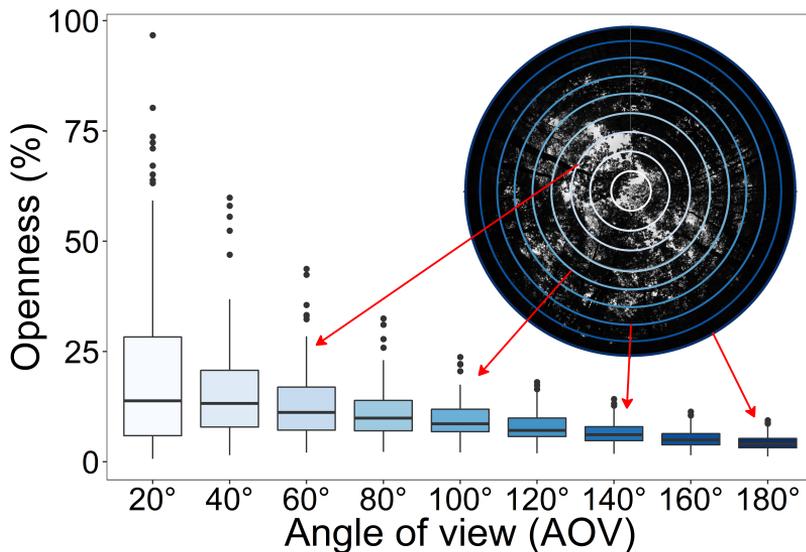
Figure 4.2: Boxplots show canopy openness calculated from identical hemispherical photographs but with different angles of view on 115 sites in European deciduous broadleaved forests. With increasing angle of view, the magnitude of canopy openness and its variability among sites decreases substantially. The area for each angle of view is illustrated as circles on a hemispherical photograph from one study site.

site factors for species richness and composition as well as mean soil temperature (Fig. 4.3). Canopy openness from 80° AOV explained substantially more variation in PAR than the best performing indirect site factor (Fig. 4.3). In contrast, total site factor explained the maximum air temperature better than canopy openness regardless of the selected AOV (Fig. 4.3).

Accuracy evaluation using the artificial calibration hemisphere revealed a minor error in gap fraction (only the ratio of sky pixels to canopy pixels, while canopy openness weights pixels by zenith angle depending on the lens projections, Gonsamo et al., 2013) estimation using the DSLR camera, ranging between +1.73 % and −0.12 % for coarse, and between +2.67 % and -0.57 % for medium checkerboard grids and a moderate tendency for gap fraction overestimation at lower zenith angles (ranging from +5.73 % to +0.36 %) for the finest grid (Fig. 4.4). Evaluated

smartphone (ASUS Zenphone 3) with 180° lens convertor reached only 140° AOV and produced images with lower contrast between black and white squares with more pronounced chromatic aberration (Appendix B, Fig. B.3). Worse image quality resulted in inconsistent error rates with the $0 - 10°$ zenith band gap fraction overestimated by 3.94 %, 4.38 % and 4.54 % for fine, medium and coarse grid size and image quality deterioration at higher AOV, resulting in significant gap fraction underestimation by -42.5 %, 20.51 % and -6.65 % for the $60 - 70°$ zenith band. In the field conditions, we found relatively strong correlations between canopy openness from DSLR and smartphone hemispherical photography (Pearson r > 0.8) for canopy openness at 40, 60, 80 and 100° AOV, but weaker correlations (r $= 0.78$ and 0.75) when canopy openness was calculated at AOV 120° and 140° (Appendix C).

4.4 Discussion

Canopy openness from hemispherical photographs is routinely calculated from the whole hemisphere (180° AOV), but we found that canopy openness from narrower zenith angles better explained plant species assemblages and understorey microclimate. For a wide range of ecological applications, canopy openness calculated from 100° AOV thus seems to be sufficient or even optimal in terms of explanatory power and standardization between different optical solutions. On the other hand, explanatory power at AOV narrower than 80° quickly deteriorated, indicating that crown (sky) area sensed within the restricted AOV is too low. This questions the ability of cover photography with restricted angle of view to satisfactory describe canopy properties using a single image per site.

There are several possible reasons why canopy openness from narrower angles performs better. First, the light transmittance near the horizon

is very low because of a longer solar beam path through the dense forest interior with almost a complete light absorption (Canham et al. 1994, Welles and Norman 1991). As a result, the sky near the horizon is usually almost completely obscured by trees, so this area contributes a little to total variability in canopy openness and to the total irradiation of the forest floor. Moreover, the light that penetrates the canopy near the horizon contributes a little to the total irradiance of the soil surface due to the high solar incidence angle and generally lower luminance of sky regions near the horizon under common atmospheric conditions.

Second, canopy openness calculated for narrow AOVs is more variable because it reflects only a part of the hemisphere, obstructed only by the nearby trees (Hennon et al. 2010). In the conditions of our sampling sites, the AOV of 100° reflects the canopy characteristics in a radius from 12 to 36 meters, depending on the stand height. This area thus corresponds to an area within which trees also affect other ecologically relevant factors such as microclimate near the ground, precipitation throughfall, litterfall, or belowground interactions (Kašpar et al. 2021, Wang et al. 2018) and is therefore more comparable to vertical crown projection (canopy cover).

The explanatory power of the canopy openness calculated from 100° AOV was comparable to radiation estimates accounting for direct and diffuse light penetrating the canopy from different angles. The indirect site factor (diffuse light), which is less anisotropic than the direct radiation, was closely correlated with canopy openness calculated from 100° AOV (r = 0.99). Both variables explained similar variations in plant species composition and richness. However, in contrast to canopy openness, the calculation of indirect site factor requires site-specific parameters of sky illuminance and a full hemispheric image. Unfortunately, site-specific parameters are rarely known because the luminance of sky regions depends on actual atmospheric conditions (Igawa et al. 2004). Imprecise photograph orientation due to insufficient magnetic compass calibration may also considerably bias this estimate, while the canopy

openness estimate is independent of azimuthal photograph orientation (Novakova and Pavlis 2019). The mismatch between measured PAR levels and direct and total site factors illustrates how sensitive these estimates are. In contrast, canopy openness at 80°AOV and indirect site factor provided a reasonable fit to PAR. The optimal AOV for PAR was slightly narrower than for vegetation or temperature indices. This difference may reflect that penetrating radiation is more localized than a temperature of flowing air mass and that vegetation is also affected by broader surrounding due to mass effects.

Therefore, canopy openness is a robust and accessible predictor of plant assemblages, but radiation site factors are better for modelling maximum air temperatures in the forest understorey.

4.4.1 Implications for canopy sensing in the field

Here we showed that the canopy openness calculated from the whole hemisphere is not necessary for some ecologically relevant information about canopy structure. This finding broadens the spectra of cameras and lenses potentially suitable for estimating canopy openness, as the AOV of 100° can be obtained not only with the circular fisheye lenses but also with some wide-angle lenses (Table 4.1). The diagonal fisheye lens, which circumscribes the hemisphere around the camera sensor, reaches the AOV of 180° only on the diagonal (Fig. 4.5). The diagonal fisheye lenses thus reduce the effective AOV for canopy openness calculation, but they can still provide an AOV above 100° on the short (vertical) side of the sensor (Table 4.1). For rectilinear lenses, a maximal focal length of 10 mm is needed to reach 100° AOV on the short side of the full-frame camera sensor (Fig. 4.5).

The hemispherical photography obtained by a circular fisheye lens should still be preferred, as it allows the calculation of the whole spectra of canopy indices needed for different applications. For example, we found that radiation calculated as the total site factor performs

better for predicting maximum air temperature. The circular fisheye lens became reasonably priced (e.g., the new Laowa 4mm f/2.8 cost around 200 €, used Sigma 4.5mm f/2.8 EX DC around 300 €), and hemispherical photographs obtained by these high-quality lenses provide the user with the widest options. On the other hand, our results showed that an ecologically relevant canopy openness is accessible to more users as the 80 - 100° AOV can be reached by more wide-spread wide-angle lenses when combined with a full-frame sensor.

Our finding also encourages the wider use of smartphones with fisheye/wide-angle lens converters. These inexpensive instrumentations have the potential to revolutionize field sampling of canopy structure because local canopy openness value can be obtained in real-time (e.g. Tichý 2016). Several studies have shown that the canopy characteristics calculated from smartphones and from standard hemispherical photographs are comparable (Bianchi et al. 2017, Smith and Ramsay 2018). The wider use of smartphone hemispherical photography in scientific research is, however, still hampered by technical limitations. First, the external fisheye lenses for smartphones often have undocumented and inhomogeneous mapping functions and projections, which makes the calculation of angular pixel area on a plane image difficult. The lens contertor which we have tested even did not reach declared 180° AOV, producing image with 140° AOV. Second, external "Clip-On" lenses currently available for smartphones have no standard mounting. Therefore, it is almost impossible to align the optical axes of the fisheye lens and the built-in optics of the smartphone. Finally, optics used in external fisheye lenses often have image quality issues like glaring, low sharpness, colour aberrations and vignetting. All these technical issues can lead to significantly biased canopy openness estimates, especially at higher AOV's and decrease the reproducibility of the results (Lusk 2022).

In our case study, we found a reasonable correlation between canopy openness calculated from a smartphone and from hemispherical photography using DSLR APS-C camera and Sigma 4.5mm circular fisheye

lens as a "gold standard" (Appendix C). Canopy openness from smartphone and classical hemispherical photography correlated substantially more when calculated from 100° AOV (Pearson r = 0.83) than when calculated from a maximum AOV provided by the smartphone (140° AOV, r = 0.75). This bias can be assigned to problematic image quality of smartphone lens, particularly at high AOV, as we demonstrated on gap fraction estimates for artifitial calibration targets (Appendix B). Canopy openness from classical and smartphone hemispherical photographs is, therefore, more comparable when calculated from smaller AOV. However, absolute differences between canopy openness estimates from classical DSLR and smartphone cameras taken simultaneously at the same sites can still be substantial even at low AOV (Appendix C). Therefore, we cannot recommend smartphone hemispherical photography for research applications, but we acknowledge that this may change with further technological advancement.

A promising alternative to smartphone fisheye photography is spherical panoramic images derived from smartphone photography using its built-in optics (Arietta 2022). This new technique stitches together multiple exposures taken in different directions and thus circumvents the limitations of the optical lens properties on the cost of computation complexity (Arietta 2022). However, the predictive performance of spherical panoramic images remains to be tested.

4.5   Conclusion

Our results showed that canopy openness calculated from around 100° AOV is optimal for a range of ecological applications, at least in the conditions of European deciduous broadleaved forests. This finding opens up the possibility of obtaining ecologically relevant canopy openness with substantially broader spectra of cameras and lenses, including smartphones with attached fisheye lenses that do not provide 180° AOV.

Smartphones and consumer-grade cameras with a wide-angle lens can thus be a reasonable and cost-effective alternative for the estimation of ecological relevant canopy openness derived from lower AOV. However, a DSLR camera with a high-quality fisheye lens is still needed to get reliable and reproducible canopy openness. Unfortunately, fisheye lenses for smartphones have substantially lower optical quality, and they are not yet able to fully substitute the hemispherical photography from DSLR cameras. Nevertheless, users of smartphones with external fisheye lenses can obtain canopy openness estimates more comparable to estimates obtained with specialized equipment if they calculate canopy openness with AOV < 120°.

In summary, we found that canopy openness calculated from hemispherical photographs with angles of view around 100° better predicts plant assemblages, forest microclimate and understorey light conditions than traditionally used canopy openness from a 180° angle of view. Moreover, canopy openness calculated from a smaller angle of view have similar predictive abilities as the best radiation site factors, which require hemispherical photography with the full 180° angle of view. These results thus provide robust background for the canopy openness calculation from a wide range of available cameras and lenses and therefore pave the road toward more accessible, standardized, and reproducible canopy openness calculation in forest ecology and meteorology.

Supplementary materials

Supplementary material associated with this article can be found, in the online version, at doi:10.1016/j.agrformet.2023.109308.
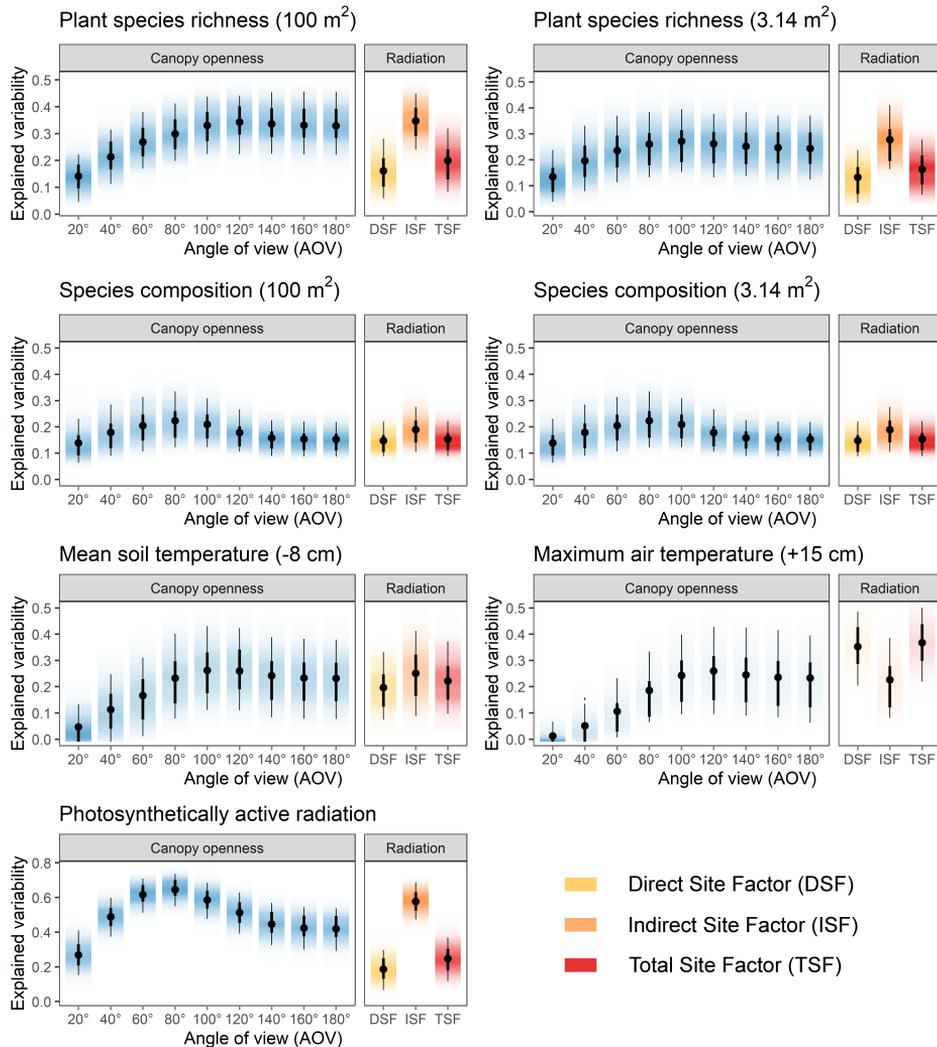
Figure 4.3: Canopy openness calculated from different angles of view explained different amounts of variability in species richness and composition of vascular plants as well as in maximum air temperature, mean soil temperature and photosynthetically active radiation (PAR). For comparison with canopy openness, we also plotted direct, indirect, and total radiation site factors. The black points represent the mean variability explained over 1000 bootstrapped datasets, the thick lines show the corresponding 66 % highest density intervals, and the thin lines paired with shading show the 95 % highest density intervals. For univariate variables, explained variability is the adjusted R^2 from the linear regression model. For species composition, explained variability is the proportion of explained variability from the maximum variability that a single predictor can theoretically explain in the same dbRDA model.
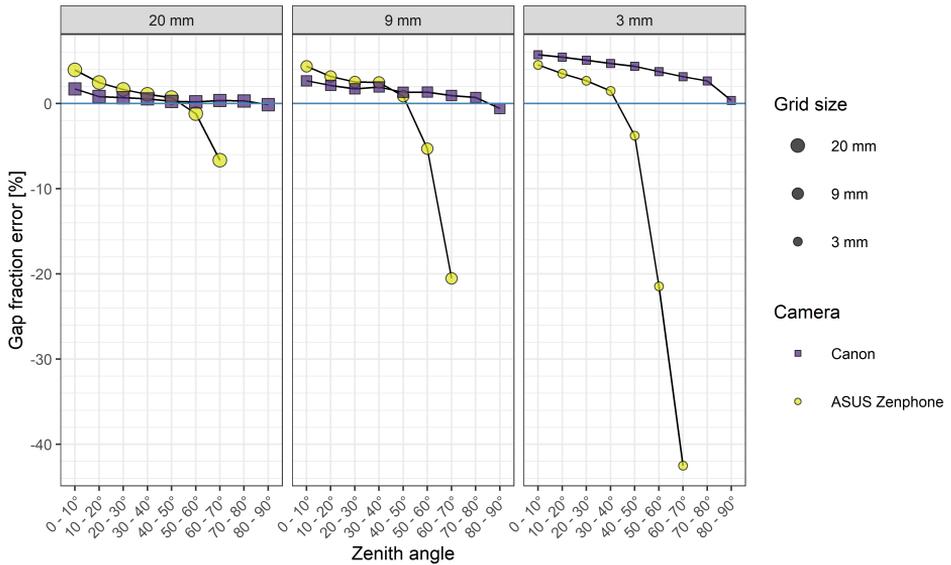
Figure 4.4: Assesment of measurement accuracy at different zenith angles using Canon DSLR camera with Sigma 4.5mm fisheye lens (squares) and smartphone ASUS Zenphone 3 with 180° lens convertor (circles), faceted according to calibration checkerboard grid size. Gap fraction error (in %) plotted on y-axis is estimated gap fraction minus expected true value (i.e. 50 %). Canon DSLR provided consistently slightly overestimated gap fraction values over whole range of zenith angles and checkerboard grid sizes, while smartphone photography did not reach declared 180° AOV and provided strongly biased gap fraction estimates at higher zenith angles, in particular for the finer grid sizes.
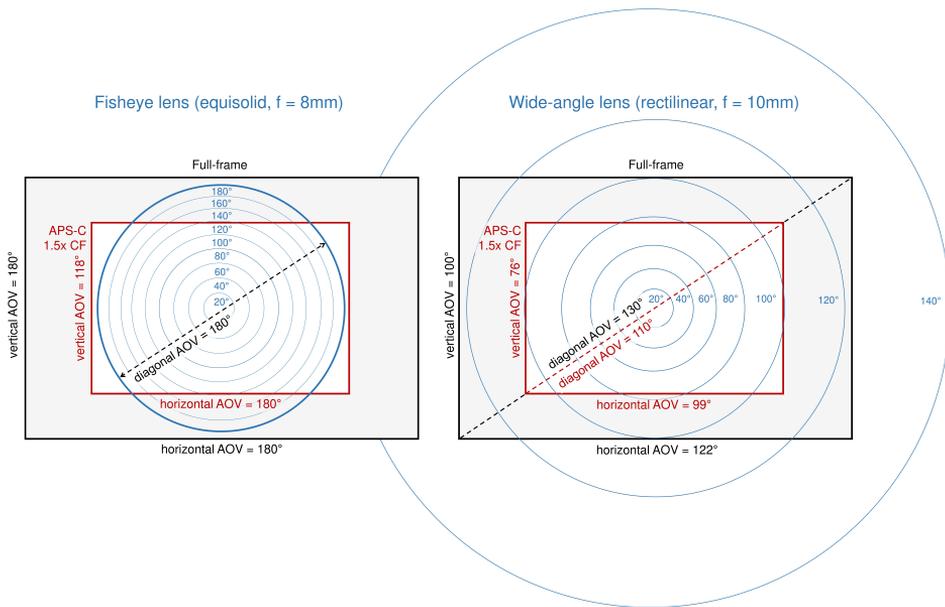
Figure 4.5: Not all fisheye lenses used for hemispherical photography provide 180° AOV. The figure shows fisheye lenses with equisolid and rectilinear projections paired with a full-frame and APS-C sensor (crop factor = 1.5) cameras. While the circular fisheye lens (left scheme) displays the whole hemisphere on the fullframe sensor (180° AOV in all directions), the circular fisheye lens on the APS-C sensor displays only part of the hemisphere (118° vertical AOV). The right schema also shows that a wideangle, rectilinear lens can display 100° vertical AOV on the full-frame sensor (for details, see Appendix D).

Chapter 5

Temperature buffering in temperate forests: Comparing microclimate models based on ground measurements with active and passive remote sensing

Vít Kašpar, Lucia Hederová, Martin Macek, Jana Müllerová, Jiří Prošek, Peter Surový, Jan Wild, Martin Kopecký

Author's contribution: Conceptualization, Methodology, Data Curation, Formal analysis, Investigation, Writing − Original Draft and Review, Visualization

Abstract

The ability of a forest to buffer understorey temperature extremes depends on the canopy structure, which is often measured from the ground. However, ground measurements provide only point estimates, which cannot be used for spatially explicit microclimate modeling. Canopy structures derived from airborne light detection and ranging (LiDAR) can overcome these limitations, but high point-density LiDAR is expensive and computationally challenging. Therefore, we explored whether unmanned aerial systems (UAS) processed with the structure-from-motion (SfM) algorithm could serve as an alternative source of canopy variables for forest microclimate modeling. Specifically, we compared the performance of the canopy cover and height derived from the ground measurements and passive (UAS-SfM) and active (UAS-LiDAR) remote sensing as predictors of air and soil temperature offsets (i.e. differences between the forest understorey and treeless areas).

We found that the maximum air temperatures were substantially lower inside than outside the forest, with differences ranging from 9.0 to 12.5 °C. The soil temperatures under the canopy were also reduced, but the soil temperature offsets were lower and ranged from 1.1 to 2.8 °C. The air and soil temperature offsets both increased with increasing tree height and canopy cover. However, the prediction ability of tree height and canopy cover differed if they were ground-based or remotely sensed. The remotely sensed canopy indices explained air temperature offsets better (UAS-SfM: $R^2 = 0.59$, RMSE = 0.75 °C; UAS-LiDAR: $R^2 = 0.57$, RMSE = 0.76 °C) than ground measurements ($R^2 = 0.51$, RMSE = 0.80 °C). Ground-based metrics explained soil temperature offsets better ($R^2 = 0.37$, RMSE = 0.36 °C) than passive remote sensing approach (UAS-SfM: $R^2 = 0.27$, RMSE = 0.39 °C), but comparably to active one (UAS-LiDAR: $R^2 = 0.35$, RMSE = 0.37 °C).

Our results suggest that both UAS-SfM and UAS-LiDAR can substitute ground canopy measurements for air temperature modeling, but soil temperature modeling is more challenging. Overall, our results show that forest microclimate can be modelled at a very high spatial resolution using UAS equipped with inexpensive optical cameras. The increasingly available UAS-SfM approach can thus provide fine-resolution microclimatic data much needed for biologically relevant predictions of species responses to climate change.

5.1 Introduction

Ecological models forecast large changes in species distributions and community composition as a result of anthropogenic climate change (Lenoir and Svenning 2015) . However, these predictions rely on coarse scale climate data interpolated from standard meteorological measurements that reflect a climate of open areas (macroclimate) and not the habitat-specific conditions (microclimate) in which organisms live (Nadeau et al. 2017). Modeling exercises based on coarse-scale climatic data thus often predict alarming extinction rates (Thomas et al. 2004) regardless of the ability of microclimate heterogeneity to buffer the effects of climate change (Suggitt et al. 2018, Scherrer and Koerner 2010).

The discrepancy between the substantial species redistribution predicted by models and actual shifts observed in biological communities is particularly evident in forest understories (Ash et al. 2017, Bertrand et al. 2011, Zhu et al. 2012). In forests, trees absorb solar radiation, reduce air mixing and cool the air by transpiration (Geiger et al. 1995). Organisms living in forest understories thus experience lower annual and diurnal maximum temperatures and higher minimum temperatures than those residing in treeless habitats (Aussenac 2000, Geiger et al. 1995, Morecroft et al. 1998). Forest canopies thus buffer especially the temperature extremes which affect organisms more than the temperature averages (Gardner et al. 2019, Körner and Hiltbrunner 2018). Since climate warming likely intensifies extreme weather events (IPCC 2013), forest temperature buffering has the potential to reduce forest species exposure to climate change (De Frenne et al. 2019). Therefore, incorporating offsets between ambient macroclimate temperature and understorey microclimate temperature into ecological models can not only refine their predictive ability (Lembrechts et al. 2019), but also more realistically estimate the severity of warming impacts on forest biodiversity and functioning (Davis et al. 2019, Zellweger et al. 2020).

The microclimatic effects of forest canopy structure have mostly been studied locally with ground-measured canopy height and cover (Kovács et al. 2020, Von Arx et al. 2012, Von Arx et al. 2013). While this approach is useful for obtaining mechanical insights into the structural drivers of the understorey microclimate, it is impossible to implement it over large and spatially continuous areas. This hampers spatially explicit interpolations of field microclimate measurements in sufficiently high resolution or downscaling of coarse-grained macroclimate data to the biologically relevant scale needed to improve predictions of species redistribution under climate change (Lembrechts et al. 2019, Franklin et al. 2013, Suggitt et al. 2018).

Remote sensing (RS) has considerable potential to enhance microclimate models by providing detailed, spatially continuous information about forest structure (Zellweger et al. 2019b). Especially active sensors based on airborne light detection and ranging (LiDAR) mounted on low-altitude unmanned aerial systems (UAS-LiDAR) enable quantification of the three-dimensional forest canopy structure in ultrahigh detail (Kuželka et al. 2020, Neuville et al. 2021, Wallace et al. 2012). While the LiDAR has been successfully used to explore the relationship between understorey temperature and canopy structure (Frey et al. 2016, Tymen et al. 2017, Broadbent et al. 2014, Davis et al. 2019, Greiser et al. 2018, Jucker et al. 2018), the major commercial products are still expensive, and data processing is computationally challenging (Bode et al. 2014, Kellner et al. 2019).

Passive RS instruments in the optical spectrum represent an economical and more accessible alternative to LiDAR and may potentially address some of the LiDAR limitations (Moudrý et al. 2019, Wallace et al. 2016). UAS optical imagery processed with the structure-from- motion (UAS-SfM) algorithm allows the detailed assessments of canopy structure (Puliti et al. 2015) and can thus be used in ecological studies focused on understorey vegetation (Bagaram et al. 2018) and microclimate modeling (Milling et al. 2018).

The performance of canopy cover and height as predictors of under-storey temperatures measured by different sensing approaches (i.e., ground measurements; active or passive remote sensing) has not yet been compared. Therefore, it is unknown whether these alternative approaches are complementary and which is best suited for forest microclimate modeling. To fill this gap, we used microclimate loggers to measure in situ air and soil temperature in temperate broadleaved forest and derived the local canopy cover and height through ground sensing (hemispherical photography and tree height measurements) and active (UAS-LiDAR) and passive (UAS-SfM) remote sensing. Here, we used these data to answer the following questions:

1) How much the local variation in canopy height and cover influences the temperature offsets between forest understorey and treeless areas?

2) How well can we model these temperature offsets with the canopy height and cover derived from passive (UAS-SfM) and active (UAS-LiDAR) remote sensing compared to ground measurements?

5.2   Methods

5.2.1   Study Area

We measured the microclimate in the Koda National Nature Reserve, which is located in the Bohemian Karst Protected Landscape Area, Czechia (49°56'N, 14°6'E). The climate is temperate, with a long-term annual average temperature $7-8$ °C, a long warm summer of $40-50$ days with a maximum daily air temperature above 25 °C, and moderately cold winter. Most precipitation falls as autumn rains, averaging approximately $550-600$ mm annually. The average annual cloud cover ranges between 60 and 65% (Tolasz et al. 2007).

The study area (approximately 35 ha) represents a topographically flat plateau lying between 355 and 395 m a.s.l. The study area is underlain by limestone bedrock with patches of gravel alluvium on old river terraces. The typical soils are Cambisols with a silt-loam texture.

The area is covered by a temperate broadleaved deciduous forest with structurally different patches ranging from younger stands with vertically uniform structures to older stands with canopy gaps (Supp. Fig. 1). The dominant tree species are *Quercus petraea* and *Carpinus betulus*, which are interspersed with *Acer campestre*, *Fagus sylvatica*, *Sorbus torminalis*, and *Tilia cordata*.

5.2.2   Field sampling

In March 2017, we established 23 forest measuring sites using a random sampling with following constrains: a distance between the sites greater than 30 m, a distance of at least 60 m from the nearest forest edge, a maximum terrain slope of 5°, and a southern inclination. Two reference sites were placed in the adjacent treeless area with the same flat topography.

Under the tree canopy, even differential Global Navigation Satellite System (GNSS) receivers are usually not sufficient to achieve submeter precision in measured geographic coordinates (Næsset and Jonmeister, 2002). Therefore, we first obtained precise positioning with a differential GNSS Trimble R8–2 (Trimble Inc.) in the adjacent treeless area. Subsequently, we positioned all measuring sites relatively to this treeless site using a total station TS Trimble 5503DRS (Trimble Inc.). All measuring sites were thus positioned with sub-decimeter horizontal accuracy.

5.2.3 Temperature data

To measure the climatic conditions experienced by the organisms living in the forest understorey, we installed one Temperature and Moisture Sensor (TMS) logger at each site (Wild et al. 2019). Each TMS logger recorded the air temperature 15 cm above the ground and soil temperature 8 cm below ground every 15 min from 5th May 2017 to 30th September 2017. We measured the temperatures during the growing season, as these are more important drivers of forest plant species distribution than yearly temperatures (Lenoir et al. 2013). All sensors were shielded by a standardized white plastic shield (Wild et al. 2019), to minimize the bias caused by direct sunlight and subsequent overheating, as well as to provide proper ventilation (Erell et al. 2005). We placed each TMS logger in a wire cage (Supp. Fig. 1) to protect it against wild animals like wild boars (Wild et al. 2019).

As air temperature offsets, we used the 95th percentile of daily differences between maximum air temperatures measured inside and outside the forest. Similarly, for soil temperature offsets, we used the 95th percentile of daily differences between maximum soil temperatures measured inside and outside the forest. We focused on maximum rather than on mean temperatures because they are more relevant for forest plants (Macek et al. 2019), as well as for other organisms, such as ectotherms (Huey et al. 2012). Offsets in maximum temperature thus determine the exposure of understorey organisms to climate extremes (Scheffers et al. 2014). Nevertheless, we also provided analyses based on mean daily differences in maximum temperatures in Supplementary Material B.

To calculate temperature offsets between forest understorey and open landscape, we first averaged simultaneous measurements from two TMS loggers placed in the treeless area (Fig. 5.1). Then, we subtracted the daily air and soil temperature maximums measured at each site below the forest canopy from the daily air and soil temperature max-

imums in treeless areas. Finally, we calculated the 95th percentile of these daily offsets to capture ecologically relevant temperature extremes (Table 5.1). While the 95th percentile was chosen arbitrarily, it does not rely on the most extreme values in the dataset, but still captures ecologically meaningful microclimatic extremes (Supp. Fig. 2). For this reason, it is commonly used in the ecologically-oriented microclimatic studies (Ashcroft and Gollan 2013, Lesser and Fridley 2016).
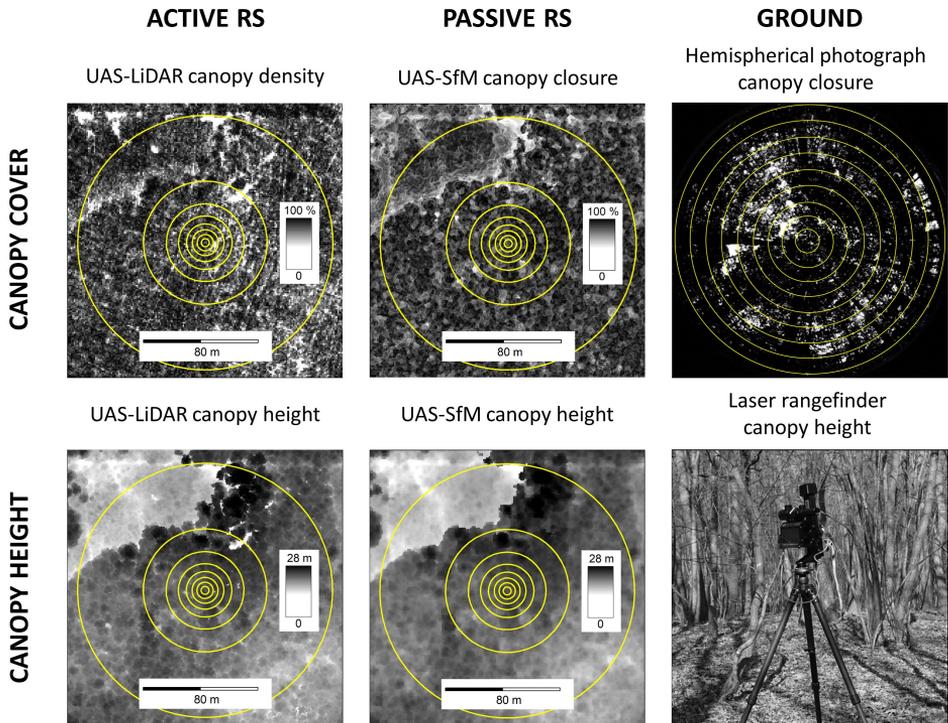
Figure 5.1: Summary of predictors divided into three groups according to approach. Yellow circles illustrate the different buffers from which the values for each predictor were extracted. (For interpretation of the references to colour in this figure legend, the reader is referred to the web version of this article.)

5.2.4 Canopy structure

We selected canopy height and canopy cover as temperature predictors because both variables strongly affect forest microclimate (Frey et al.

Table 5.1: Summary of canopy structure predictors used to model temperature offsets between the treeless areas and below canopy temperature measured at 23 sites within the temperate deciduous forest. Air temperatures were measured 15 cm above the ground, and soil temperatures were measured 8 cm below the ground every 15 min during the growing season (May − September 2017).

	Temperature offsets	Unit	Description	Range (mean)
	Air temperature offsets	°C	95th percentile of daily differences between the maximum air temperature inside and outside forest	−12.5 to −9.0 (−11.5)
	Soil temperature offsets	°C	95th percentile of daily differences between the maximum soil temperature inside and outside forest	−2.8 to −1.1 (-1.9)
	Predictor	Unit	Description	Range (mean)
CANOPY COVER	GROUND − Canopy closure	%	The proportion of the hemispherical photograph obscured by vegetation, viewed from a single point below canopy	86.1−94.8 (91.8)
	PASSIVE RS − Canopy closure	%	The proportion of the sky hemisphere unobscured by SfM-derived canopy surface	66.5−75.8 (73.0)
	ACTIVE RS − Canopy density	%	The proportion of all UAS-LiDAR point cloud returns from above 3 meters to all returns	75.9−90.1 (84.3)
CANOPY HEIGHT	GROUND − Canopy height	m	Canopy height measured in situ	14.3−22.8 (18.5))
	PASSIVE RS − Canopy height	m	Canopy height model from UAS-SfM	10.6−18.7 (15.9)
	ACTIVE RS − Canopy height	m	Canopy height model from UAS-LiDAR	11.6−19.2 (16.7)

2016, Greiser et al. 2018, Jucker et al. 2018). To compare the performance of differently derived predictors, we measured the canopy height and cover on each site through three independent approaches:

ground measurements and remote sensing based on passive UAS-SfM and active UAS-LiDAR (Fig. 5.1). For clarity, we use the general term canopy cover for all three approaches, but we acknowledge that estimates from hemispherical photographs are usually referred to as canopy closure (Jennings et al. 1999).

5.2.4.1   Ground measurement

To estimate the canopy cover from the ground measurements, we captured hemispherical photographs at the height of one meter directly above each TMS logger using the Canon 40D camera with a Sigma 4.5 mm F2.8 EX DC Circular Fish-eye lens. First, we converted the photographs to grayscale by using double weight for the blue channel to intensify the contrast between the sky and canopy. Then, we classified the converted images into black (canopy) and white (sky) pixels using an automatic thresholding function from Sidelook 1.1 (Nobis and Hunziker 2005). Finally, we calculated the fraction of sky hemisphere obstructed by vegetation directly above each TMS logger (GROUND – Canopy Closure) using WinSCANOPY® software (Regent Instruments Inc.). For each photograph, we computed canopy closure from delimited sphere areas of sequentially increasing zenith angles ($10-90°$). As the second in situ predictor (GROUND $-$ Canopy height), we used the mean height of the dominant canopy trees growing in the 11.28 m radius ($400\,\mathrm{m}^2$) around each TMS logger. To measure tree height, we used a TruePulse 200X laser rangefinder and inclinometer.

5.2.4.2   Passive remote sensing

To estimate the canopy cover and height through passive remote sensing, we applied the SfM algorithm to optical imagery obtained from a UAS-borne RGB camera. Fully automated UAS mapping missions were controlled by the APM ArduPlane/PixHawk autopilot and carried a lowcost camera Sony Alpha A5100 with an APS-C sensor (Müllerová

et al. 2017). Because of the dense canopy, detection of the ground by the optical-based method was problematic. Therefore, the summer flight mission conducted under leaf-on conditions during the peak of the growing season (August 2017) was supplemented by a winter mission under leave-off conditions (February 2018). In total, 361 RGB images for summer and 354 for winter mission were obtained with an overlap and sidelap ranging between 80 % and 85 %, which was sufficient for the SfM procedure (Supp. Table 1).

To enhance the georeferencing accuracy for both missions, we used five ground control points situated in open fields that were positioned by a differential GNSS Trimble GeoExplorer 6000 Series (Trimble Inc.). The measurements were differentially post-processed to achieve a onedecimeter accuracy. The RGB imagery was processed in Agisoft PhotoScan Professional, ver. 1.4.2.6205 (Agisoft LLC) by using the SfM algorithm and modeling the three-dimensional structure from the spectral scene (Dandois and Ellis 2010).

As a proxy for canopy height (PASSIVE RS – Canopy height), we used the canopy height model (CHM) that was calculated as the difference between the digital surface model (DSM), which represented the elevation of the highest points in leaf-on conditions, and the digital terrain model (DTM), which was created by triangulation of the classified ground points inferred during the leaf-off season.

In dense forest stands, the SfM algorithm did not allow ground capture, and we were therefore not able to directly derive canopy cover with the SfM method. We tried several published methods (Getzin et al. 2014, Zielewska-Büttner et al. 2016), but none of them provided estimates of canopy cover significantly correlated with the ground-measured canopy closure (Supp. Fig. 3). Therefore, we developed a new method based on geomorphometry. The idea is that CHM from UAS-SfM represents the micro-topography of the forest canopy surface, and the concave depressions in this surface represent canopy gaps allowing more light to reach the ground (Supp. Fig. 4). To numerically

represent this micro-topography of the canopy surface, we calculated the percentage of the visible sky, i.e. a portion of the hemisphere that was unobscured by the surrounding canopies, using the Sky View Factor tool from SAGA GIS, ver. 2.3.2 (Conrad et al. 2015). This measure thus represents an estimate of local canopy closure, and the more unobscured the focal pixel is, the higher the local canopy closure. To obtain reliable estimates of the unobscured sky hemisphere for each pixel of the CHM, we set the maximum search radius for the Sky View Factor to 50 m and integrated it over 360 one-degree sectors (Böhner and Antonić 2009). The resulting PASSIVE RS − Canopy closure was reasonably correlated with the canopy cover indices derived from the ground measurements as well as from the active RS (Supp. Fig. 3).

5.2.4.3 Active remote sensing

To estimate the canopy cover and height by active RS, we used UAS-borne LiDAR. The flight campaign of the UAS RiCOPTER (Riegl Laser Measurement Systems GmbH) was performed in August 2018 at a phenological stage that was comparable to that during the passive RS summer mission (Supp. Fig. 5). The scanning sensor was a RIEGL VUX- 1UAV laser scanner with a set maximum scan angle of 60°, which enables sufficient overlapping and reduces computation complexity (Supp. Table 1). To derive and georeference the preliminary LiDAR point clouds, we used POSPac MMS8 (Applanix) and RIPROCESS (Riegl Laser Measurement Systems GmbH).

Because of the unequal LiDAR pulse distribution, we thinned the point cloud using the function *homogenize* in lidR package 2.1.2 (Roussel et al. 2020), which reduced the point cloud to the average point density of 57.1 returns per 1 m^2. This processing step, although degrading point cloud density in some areas, is often used (Kuželka et al. 2020, Wedeux et al. 2020), does not affect the accuracy of predicted forest structures at high point densities (Jakubowski et al. 2013) and did not

bias our results (Supp. Fig. 6).

To extract the ground surface points from the thinned point cloud, we used the *lasground* tool from LAStools software (Rapidlasso GmbH). First, we excluded all points exceeding a $\pm$ 1 m difference from the average elevation in a 5 $\times$ 5 m grid. Subsequently, we calculated the height of all points above the triangulated surface of the classified ground points. Finally, we calculated a 0.5-m resolution raster of CHM (ACTIVE RS – Canopy height) by triangulating and rasterizing the highest return above the ground points in cell size 0.5 $\times$ 0.5 m, using the lasgrid tool from LAStools.

As the UAS-LiDAR canopy cover, we used the *lascanopy* tool to calculate the canopy density (ACTIVE RS − Canopy density), which was defined as a percentage of all point cloud returns above a threshold of 3 m height from all returns in a 1 m cell. The 3 m threshold was chosen because it roughly corresponded to the height of the taller shrubs at our study area and was best correlated with canopy

5.2.4.4   Selection of buffer radius

Since the understorey microclimate is influenced by the forest canopy in the wider surroundings (Frey et al. 2016), the RS canopy indices should consider not only the value from a particular pixel but also neighboring values in a certain buffer radius (Bode et al. 2014). To explore which buffer provided the most relevant information, we compared the predictive performance of several buffer radii calculated from canopy height above each site and tangents of different fields of view α ranging between 10 and 80° (Bode et al. 2014) as follows:

$$\text{buffer radius} = \frac{\text{canopy height}}{\tan 90°\text{-} \alpha}$$

The values of each RS predictor were averaged and extracted (Davis et al. 2019) within the delimited buffer (Fig. 5.1, Supp. Table 2). For each

predictor, we choose only the value with the highest explained variability (R^2) of microclimate response (Supp. Fig. 8), when R^2 indicated a distinctive peak (e.g., PASSIVE RS – Canopy height, ACTIVE RS – Canopy height). In other cases, we evaluated the predictors within the same buffer radius for both RS approaches (e.g., for air temperature offsets PASSIVE RS – Canopy closure according to ACTIVE RS – Canopy cover) to maintain comparability.

We used a similar selection for the canopy closure data derived from the hemispherical photographs (Supp. Fig. 8), where we first calculated canopy closure from nine zenith angles ($10-90°$) and then selected the canopy closure with the best predictive performance (60°).

5.2.4.5 Statistical analysis

We used multiple linear regression to explain the offsets in the air and soil temperatures using canopy height and canopy cover. Initially, we also considered the interaction between canopy height and cover, but models with the interaction explained similar variance and have substantially higher AIC (Supp. Table 3). Therefore, we decided not to include the interaction in the final models.

For each temperature offset, we fit three models, each based on canopy height and cover derived by a different sensing approach. To test for possible spatial autocorrelation of the model residuals, we explored Moran's correlograms, which were calculated with the *ncf* package in R (Bjørnstad 2019). To test whether the distances from the treeless reference or the nearest forest edge influenced the temperature offsets, we used linear regression.

To obtain robust estimates of the predictive ability of each approach, we used bootstrapping (Fieberg et al. 2020). Specifically, we recalculated each model 1000 times; each time with a different dataset of 23 sites created by random sampling with replacement. As a robust estimate of the model fit, we calculated the mean R^2 from the 1000 bootstrapped

models. To further evaluate the predictive performance of the fitted models, we also calculated root-mean-squared error (RMSE) based on leave-one-out cross-validation implemented with the *caret* package for R (Kuhn 2008).

To explore the relative importance of the canopy height and cover in each fitted model, we partitioned the explained variance among the canopy height, cover, and their shared effect with the *varpart* function from the *vegan* package in R (Oksanen et al. 2013). The shared effect in variation partitioning means that both explanatory variables are able to explain the shared part of the explained variation when used alone.

5.3 Results

5.3.1 Temperature offsets

The air temperature offsets ranged between $-12.5\,°C$ and $-9.0\,°C$ (mean $-11.5\,°C$), whereas the soil temperature offsets were substantially lower and ranged from $-2.8\,°C$ to $-1.1\,°C$ (mean $-1.9\,°C$) (Fig. 5.2). Neither the air nor soil temperature offsets were spatially autocorrelated (Supp. Fig. 9), nor were they related to the distance from the treeless reference (air temperature offsets: $R^2 = 0.04$, p-value $= 0.39$; soil temperature offsets: $R^2 = 0.11$, p-value $= 0.13$) or the nearest forest edge (air temperature offsets: $R^2 = 0.03$, p-value $= 0.42$; soil temperature offset: $R^2 = 0.01$, p-value $= 0.76$).

5.3.2 Modeling temperature offsets

The RS-derived canopy height and cover explained slightly more variance in air temperature offsets than those assessed by ground measurements (Table 5.2, Supp. Fig. 10). The bootstrapped models achieved in average even higher explained variance compared to simple regression
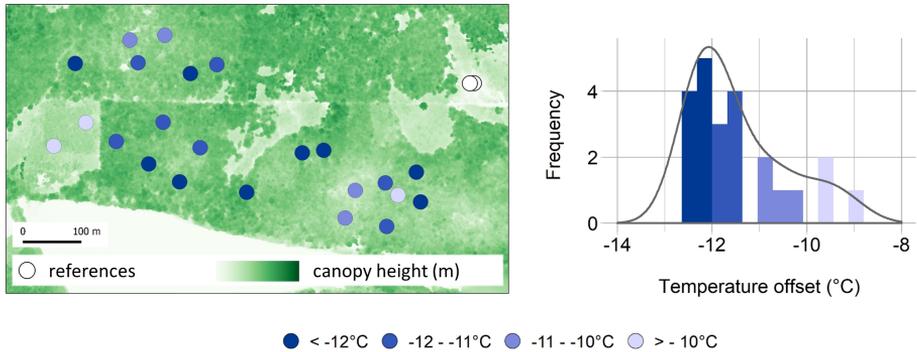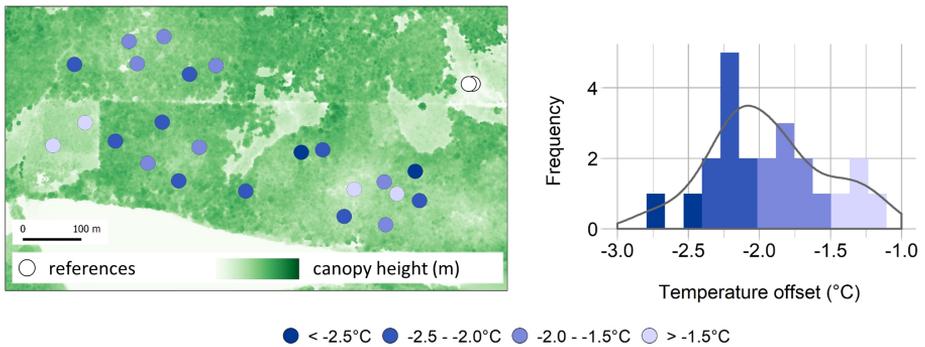
Figure 5.2: Spatial pattern and distribution of the 95th percentile of daily temperature offsets between the maximum temperature inside and outside the forest, calculated separately for air (15 cm) and soil (−8 cm) temperatures. The background map represents the canopy height model. The darker the hue is, the higher the tree layer.

models (PASSIVE RS - average bootstrapped $R^2 = 0.61$; ACTIVE RS - average bootstrapped $R^2 = 0.60$; GROUND - average bootstrapped $R^2 = 0.54$). Both active and passive RS approaches had similar prediction abilities, although models using passive RS data performed slightly better (Fig. 5.3). In all three models, the residuals were spatially independent (Supp. Fig. 9).

The soil temperature offsets were best predicted by ground-based metrics, followed by the model based on UAS-LiDAR indices, which ex-

plained slightly less variance in soil temperature offsets (Table 5.2). The regression model based on UAS-SfM predictors had the lowest R^2 and was not statistically significant (Table 5.2). The bootstrapped models explained more variance on average (GROUND - average bootstrapped $R^2 = 0.41$, ACTIVE RS - average bootstrapped $R^2 = 0.39$; PASSIVE RS - average bootstrapped $R^2 = 0.32$); however, there was high R^2 variability among the RS models (Fig. 5.3). In all three models, the residuals were spatially independent (Supp. Fig. 9).

Table 5.2: Summary of multiple regression models predicting 95th percentile of offsets between the daily maximums of air and soil temperatures inside and outside the forest by canopy height and cover derived by GROUND measurements, ACTIVE and PASSIVE remote sensing.

Temperature offset	Measurement	R^2	RMSE (°C)	F model	p-value
Air temperature offsets	GROUND	0.51	0.800	10.55	0.0007
	ACTIVE RS	0.57	0.758	13.25	0.0002
	PASSIVE RS	0.59	0.746	14.15	0.0001
Soil temperature offsets	GROUND	0.37	0.363	5.97	0.0092
	ACTIVE RS	0.35	0.368	5.43	0.0130
	PASSIVE RS	0.27	0.390	3.78	0.0405

5.3.3 Importance of individual predictors

The relative importance of the predictors differed according to the sensing approach (Fig. 5.4). For the RS proxies, the canopy height explained substantially more variance in the air temperature offsets than the canopy cover. This contrasted with the ground-estimated canopy indices, where the canopy height effect was lower and was shared mainly with that of canopy cover (Fig. 5.4). On the other hand, the effect of the canopy cover proxies derived from RS was smaller compared to hemispherical photography, both absolutely and relatively within the group. In the case of passive RS, the effect of canopy cover was especially small (Fig. 5.4).
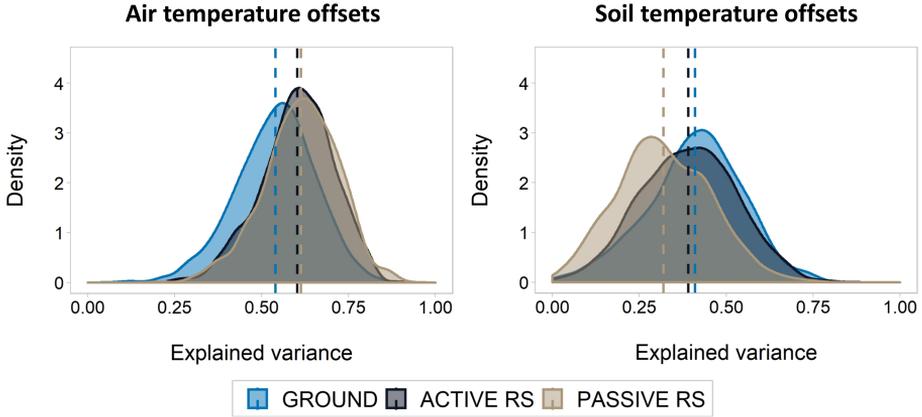
Figure 5.3: Explained variance in the 95th percentile of offsets between the daily maximums of air and soil temperatures inside and outside the forest by 1000 bootstrapped multiple regression models derived from RS canopy structure proxies (ACTIVE RS or PASSIVE RS) and ground-based canopy structure proxies (GROUND). While both RS approaches predicted air temperature offsets better than the ground measurements of forest canopy structure, in case of soil temperature offsets, the ground measurements were better predictors compared to the RS approaches, especially the PASSIVE one.

Compared to air temperature offsets, soil temperature offsets were relatively more affected by canopy cover, especially by canopy cover derived from hemispherical photographs (Fig. 5.4). Canopy height predicted soil temperature offsets best when it was inferred by RS, while its effect was mostly shared with canopy cover when it was derived from ground measurement (Fig. 5.4). Similarly, as in case of air temperature offset, canopy cover derived by passive RS was only a weak predictor.

5.4   Discussion

The forest canopy substantially buffered the near-ground air and soil temperature maximums during the growing season. Our study design eliminated the effect of terrain topography on understorey temperatures, but we still found surprisingly high spatial variation in the temperature offsets even in topographically uniform and geographically small areas.
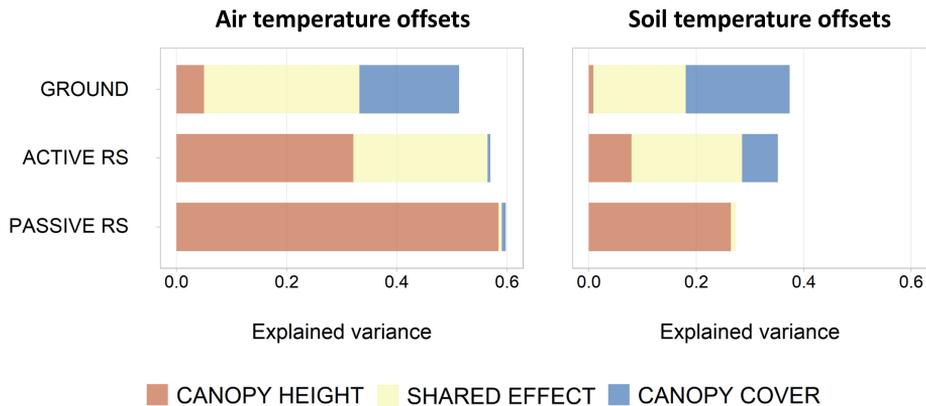
Figure 5.4: Variance in the air and soil temperature offsets between the forest understorey and tree-less area explained solely by canopy cover, solely by canopy height, and jointly by both variables derived through ground measurements (GROUND), passive (UAS-SfM), and active (UAS-LiDAR) remote sensing.

Local variation in canopy cover and height thus created substantial microscale heterogeneity in understorey temperatures (see also Jucker et al. 2018, Zellweger et al. 2019a), differing from ambient macroclimate distinctively as temperatures became more extreme (De Frenne et al. 2019). Buffering capacity of forest canopies, so far mostly neglected in ecological models, can probably also compensate for the warming impacts on the understorey plant communities (Zellweger et al. 2020). Incorporating reliable estimates of canopy attributes across space and time into ecological modeling is therefore crucial in order to make a more accurate assessment and prediction of forest species responses to anthropogenic climate change. Here, we found that UAS-based indices of canopy structure could serve as a sufficient and effective solution, and can advance forest microclimate modeling towards continuous coverage at a resolution relevant to the organisms living in the forest understorey.

While many studies give strong emphasis on canopy cover as a dominant driver of understorey microclimate (e.g. Zellweger et al. 2019a),

the importance of tree height is increasingly recognized (Jucker et al. 2018). Despite partial co-linearity between canopy height and cover (Supp. Fig. 11), we found that canopy height has a unique effect on forest microclimate. The probable reason for this effect is that a higher canopy allows less vertical mixing of warm air downward to the forest floor due to the greater distance for turbulent eddies to penetrate (Hardwick et al. 2015).

Interestingly, both the passive and active UAS-RS showed similar predictive abilities in our study. In open forest stands, LiDAR and SfM photogrammetry can extract comparable information about tree height (Wallace 1878). However, in closed-canopy forests, the SfM approach lacks information about the ground that is needed to derive DTM. To overcome this drawback, the DTM can be obtained from increasingly available national LiDAR products. However, in many countries, such products lack sufficient point density, and are still not freely accessible. Therefore, we used leaf-on UAS campaigns to derive a digital surface model and leaf-off UAS campaigns to derive a digital terrain model. Our results showed that this UAS-SfM approach could provide a canopy height model with a predictive ability that was fully comparable with the canopy height model derived from LiDAR (see also Moudrý et al. 2019).

Both the UAS-RS metrics of canopy height were superior to the ground-measured tree heights. We attribute this to the continuous spatial coverage of RS, which allowed us to obtain the canopy heights for a broader radius around the temperature sensors compared to the ground-measured canopy heights, which were available for only several trees at each site. Indeed, the understorey temperatures were more affected by the stand height in the broader area around the microclimate loggers than by the height of the trees that was estimated directly above the logger (Supp. Fig. 8). This agrees with other studies reporting stronger microclimatic effects of the forest structure integrated over a broader scale than the local stand structure (Davis et al. 2019, Frey et al. 2016).

The reasons could be the influences of more distant small patches of canopy gaps or high-contrast edges at different heights of forest stands, which are wind-exposed and tend to be more susceptible to temperature changes (Vanwalleghem and Meentemeyer 2009). These findings further stress the potential of increasingly available high resolution canopy height models from RS in spatially-explicit modeling of understorey microclimate.

In contrast to the strong effects of canopy cover that were calculated from the hemispherical photographs, the canopy cover derived from UAS-SfM was only a weak predictor of temperature offsets. While many studies covering wide gradients of canopy cover reported a significant relationship between canopy cover derived from hemispherical photography and that from UAS-SfM (Abdollahnejad et al. 2018, Bagaram et al. 2018, Getzin et al. 2014, Chianucci et al. 2016), our study area covered only a relatively narrow gradient of canopy cover. Nevertheless, such a range is typical for temperate broadleaved forests in Central Europe (Macek et al. 2019). Moreover, we tried several published methods to derive canopy cover from UAS-SfM (Bagaram et al. 2018, Chianucci et al. 2016, Getzin et al. 2014, Zielewska-Büttner et al. 2016), but no method provided estimates that were significantly correlated with the ground-measured canopy closure (Supp. Fig. 3). Therefore, we developed a new method based on geomorphometry, which provided estimates of canopy closure that were strongly correlated with UAS-LiDAR (Supp. Fig. 3). Since the effect of passive RS canopy closure in our dataset was mostly shared with the impact of canopy height, it did not affect the overall predictive ability of our models. However, the estimation of canopy cover with the UAS-SfM deserved further investigation, as no currently used methods provide good results in closed-canopy forests. To further increase the performance of the canopy cover derived from UAS-SfM, flight missions should (i) be conducted under cloudy conditions without direct sunlight (Getzin et al. 2014); (ii) combine two flights – the first before and second after the solar noon - to create

orthomosaics with diverging shadow orientations (Rahman et al. 2019); and (iii) use the image overlap up to 90% to increase canopy penetration (Dandois et al. 2015, Hirschmugl et al. 2007).

Soil temperature offsets were more difficult to predict than the air temperature offsets, chiefly due to the lower influence of the canopy height. Variance in soil temperature offsets were mainly explained by canopy cover, but its relative importance differed according to the sensing approach. While canopy cover derived from UAS-SfM was not an important factor, canopy cover measured from the ground or from UAS-LiDAR was more important. This is consistent with the results of Hennon et al. (2010), who found comparable effects of cover estimated from hemispherical photographs and airborne LiDAR on soil temperatures. Minor difference of predictive power in our study can be potentially attributed to higher height threshold used for estimating the cover from LiDAR, which thus did not include low shrubs and tall herbs that also affect the soil temperatures (Paul et al. 2004). However, we decided for a 3 m threshold because the canopy cover calculated with this threshold correlated the best with the canopy cover from hemispherical photographs (Supp. Fig. 7), and because the lower shrub layer was sparse in our study area (Supp. Fig. 1). Therefore, we think that a more likely explanation lies in the combination of a large off-nadir scan angle, a high laser-pulse repetition rate and the size and reflectivity of the targets. Because we used a high laser-pulse repetition rate, the point density increased, but the energy per emitted laser pulse decreased (Kellner et al. 2019). As a result, the pulses were scanned at high angles with low energy and increased footprint size can miss small leaves in the upper parts of the canopy (Liu et al. 2018) and probably reflect woody obstacles such as tree trunks, which have higher reflectivity than branches. Thus, the canopy cover derived by UAS-LiDAR was slightly underestimated, which can potentially explain its lower effect on temperature offsets. For future studies, we thus recommend planning UAS-LiDAR missions with flight lines closer to

each other to avoid using large off-nadir scan angles and high laser-pulse repetition rates.

Overall, none of the approaches was able to explain more than half of the observed variability in soil temperature offsets. This unexplained variability may be caused by variable soil properties, microtopography, litter cover or herb layer density (Ford et al. 2013, Giuggiola et al. 2018, Pfeifer et al. 2019). While we did not investigate these effects in our study, the full waveform LiDAR can potentially distinguish between ground and herb reflections (Latifi et al. 2016). Similarly, UAS-SfM method can use several flights corresponding with phenological stages to overcome the canopy obscuration and enable to detect contrasted ground vegetation (Hernández-Clemente et al. 2019). Nevertheless, our results indicate that modeling soil temperature offsets with UAS-RS methods remains challenging.

We found that passive RS with a high-resolution RGB camera combined with the SfM algorithm can be suitable for predicting temperature offsets between open areas and forest understories. Using the affordable UAS-SfM method thus opens up the possibility for microclimate modeling at very high spatial detail over whole forest stands. The low costs of UAS campaigns and automatic user-friendly mission planners allow repetitive operations, accessible data acquisition and optimization revisit time. Therefore, the UAS-SfM can be used to explore how temperature buffering under forest canopies acts under different phenological stages or meteorological conditions. Using the UAS-SfM method to model understorey temperatures can thus substantially improve the assessment of climate change impacts and lead to more realistic forecasts of species distribution and community composition.

5.5   Conclusion

Here, we explored the buffering effects of canopy structure assessed by three different approaches on air and soil temperature offsets inside and outside the forest. We found that the canopy height and cover amplified the temperature differences near the ground between forest understories and open areas, emphasizing a discrepancy between standard meteorological data and the conditions experienced by understorey organisms. For air temperature modeling, our results suggested that UAS-based remote sensing can advance forest microclimate modeling towards a high spatial resolution and continuous coverage, which was needed for relevant predictions of the species responses to environmental change. Moreover, we showed, the performance of UAS-SfM derived metrics can be comparable to those obtained by UAS-LiDAR. In the modeling of soil temperature offsets, the predictive ability of UAS-based canopy structure metrics was low, and the soil temperature modeling with RS thus remains a challenge.

Supplementary materials

Supplementary material associated with this article can be found, in the online version, at https://doi.org/10.1016/j.rse.2021.112522.

Chapter 6

Unmanned aerial systems for modelling air pollution removal by urban greenery

Vít Kašpar, Miloš Zapletal, Pavel Samec, Jan Komárek, Jiří Bílek, Stanislav Juráň

Author's contribution: Conceptualization, Methodology, Data Curation, Formal analysis, Investigation, Writing − original draft, review & editing, Visualization

Abstract

Urban greenery plays an important role in reducing air pollution, being one of the often-used, nature-based measures in sustainable and climate-resilient urban development. However, when modelling its effect on air pollution removal by dry deposition, coarse and time-limited data on vegetation properties are often included, disregarding the high spatial and temporal heterogeneity in urban forest canopies.

Here, we present a detailed, physics-based approach for modelling particulate matter (PM_{10}) and tropospheric ozone (O_3) removal by urban greenery on a small scale that eliminates these constraints. Our procedure combines a dense network of low-cost optical and electrochemical air pollution sensors, and a remote sensing method for greenery structure monitoring derived from Unmanned aerial systems (UAS) imagery processed by the Structure from Motion (SfM) algorithm.

This approach enabled the quantification of species- and individual-specific air pollution removal rates by woody plants throughout the growing season, exploring the high spatial and temporal variability of modelled removal rates within an urban forest. The total PM_{10} and O_3 removal rates ranged from 7.6 g m^{-2} (PM_{10}) and 12.6 g m^{-2} (O_3) for mature trees of *Acer pseudoplatanus* to 0.1 g m^{-2} and 0.1 g m^{-2} for newly planted tree saplings of *Salix daphnoides*.

The present study demonstrates that UAS-SfM can detect differences in structures among and within canopies and by involving these characteristics, they can shift the modelling of air pollution removal towards a level of individual woody plants and beyond, enabling more realistic and accurate quantification of air pollution removal. Moreover, this approach can be similarly applied when modelling other ecosystem services provided by urban greenery.

Keywords: dry deposition, ground-level ozone, leaf area index, particulate matter, Structure from, motion, unmanned aerial systems

6.1 Introduction

Urban greenery represents a nature-based solution for reducing health risks (Nowak et al. 2006) and providing opportunities for a better quality of life and well-being (Noszczyk et al. 2022) in ever-expanding cities (United Nations, Department of Economic and Social Affairs 2019). Among other services, greenery removes air pollution by dry deposition of particulate matter (PM_x) on plant surfaces (Beckett et al. 1998) and by absorption of gasses, such as tropospheric ozone (O_3), through leaf stomata (Laisk et al. 1989). Greenery planting and its maintenance have, thus, become popular measures strongly supported by the public and councils (Eisenman et al. 2021). However, the considerable costs that are and will be spent on urban greenery growth should be based on a rational cost-benefit assessment using relevant data (Sicard et al. 2018), which include site-specific air pollution concentration and spatially-focused but extensive information on the greenery structure (Morani et al. 2011).

Air pollution is standardly monitored by governmental institutions. The layout of monitoring station networks is typically sufficient to map regional differences in air quality, but it often fails to describe processes and conditions on an urban or street scale (Britter and Hanna 2003). The knowledge of pollutant concentrations in a particular location is, however, essential for the quantification of air pollution removal by urban parks, alleys or individual trees (Tiwari et al. 2019). Additionally, fine-grain air quality data should be also taken into account when choosing locations and species for planting, as the sensitivity to local air pollution and the capability to remove it varies significantly among plant species (Yang et al. 2015). Nowadays, portable, low-cost air pollution sensors and wireless communication systems enable densification of the current monitoring networks and the capture of tempo-spatial air pollution variability in cities (Kumar et al. 2015). Long-term measurement by well-placed sensors can, for instance, reveal the difference

in the air quality before and after planting greenery and, thus, monitor its direct effect on air purification (Srbinovska et al. 2021).

Greenery structure, most commonly characterized by the Leaf Area Index (LAI), is another important determinant of air pollution removal. Although this indicator reduces the overall foliage complexity (Jonckheere et al. 2004), it is a crucial parameter in modelling air pollution removal (Janhäll 2015), which emphasizes the need for its accurate determination (Sicard et al. 2018, Tiwary et al. 2009). Traditionally, the LAI of urban greenery has been estimated indirectly from allometric species-specific relationships with other ground-measured structural parameters (Nowak and Crane 2000, Nowak 1996). Over larger scales, however, such an approach is extremely time-consuming, labour-intensive and problematic to scale up, which makes the mapping of LAI spatial and temporal dynamics difficult. Additionally, if species metrics are not available, generic LAI values over the whole urban forest of the same type (e.g. broadleaf or coniferous) are applied (Tallis et al. 2011, Tiwary et al. 2009).

Remote sensing techniques, on the other hand, meet these challenges, enabling repeatable monitoring of vegetation phenology with extensive and spatially continuous coverage (Tillack et al. 2014). Therefore, remote sensing based on airborne Light detection and ranging (LiDAR) (Bottalico et al. 2017) or aerial and satellite imageries (Manes et al. 2016, Fusaro et al. 2017) has been already used in several studies quantifying the role of vegetation in air pollution removal. Nevertheless, while air- and space-borne passive remote sensing may be feasible for modelling air pollution removal in areas of homogeneous land cover on a coarse scale, analysis of the detailed structure of individual trees is beyond their distinctiveness. Airborne LiDAR, on the other hand, allows precise canopy structure quantification (Moeser et al. 2014), but the data acquisition costs may be prohibitive for the local authorities.

Passive sensors onboard Unmanned aerial systems (UAS) address some of the airborne LiDAR limitations (Dandois et al. 2015), offering a com-

promise between the costs and spatial detail. UAS optical imagery processed using the Structure from motion (SfM) algorithm allows high-resolution assessment of greenery structure (Puliti et al. 2015) in the extents of up to several square kilometres, which is suitable for evaluating ecosystem services of urban greenery in public spaces and parks. Despite the recent application of UAS-SfM in urban forest inventory (Isibue and Pingel 2020, Wang et al. 2021), this approach remains neglected in modelling air pollution removal by urban greenery.

This study aims to implement cost-effective sensors and remote sensing methods based on UAS-SfM for evaluating air pollution removal by urban greenery. In particular, by combining PM_{10} and O_3 concentration data from a dense monitoring network and remotely-sensed vegetation indices at a high spatial resolution, we aim to (1) characterize the heterogeneity of canopy structure properties in an urban area and, using these parameters, (2) to model the air pollution removal by woody plants through dry deposition and (3) to explore the spatial and temporal variability of modelled air pollutant removal rates among various life stages and woody plant species of urban greenery.

6.2 Materials and Methods

6.2.1 Study Area

The study area (1.1 ha) is situated at the transition between the residential area and urban forests (Fig. 6.1) in Ostrava − Radvanice, Czechia (49.804°N, 18.337°E). The area lies within a broad topographically flat basin between 252 and 241 m above sea level. The local climate, at the border between the oceanic (Köppen: Cfb) and humid continental (Dfb) types, features hot and humid summers and relatively mild winters, with a long-term average annual temperature of 9.3 °C (January: −1.6 °C, July: 19.5 °C) and average annual precipitation of

about 580 mm.

The broader area represents an example of a heavily industrialized conurbation with a high population density. Local air quality is notably worsened by nearby smelter and ironworks facilities (about 1 km westward), heavy traffic (about 150 m westward) and regional transboundary pollution transport. Air pollution limits in the area are repeatedly exceeded (Pokorná et al. 2015) and the entire area is considered to be one of the European air pollution hot spots (Kozáková et al. 2019).

To reduce air pollution, local authorities initiated the planting of new urban greenery in the study area. The assemblage composition (Table A1) and its configuration (Fig. 6.1) were designed in accordance with the previously suggested principles (Barwise and Kumar 2020, Abhijith et al. 2017), considering urban context and local environmental conditions while prioritising native species tolerant to the high pollution load and those with potentially higher efficiency in air pollutant removal (Sæbø et al. 2012). Newly planted tree saplings complemented structurally different patches of temperate broadleaved deciduous trees and shrubs in various life stages (Fig. 6.1). The dominant woody plant species are *Alnus glutinosa*, *Acer pseudoplatanus* or *Salix caprea* (Table A1).

6.2.2 Greenery classification

To distinguish between the efficiencies of air pollution removal through dry deposition by woody plants (hereinafter, we will refer to this simply as "air pollution removal") at different life stages and plant species, we performed a field survey (Table A1) and classified each individual woody plant in the study area into three categories: (1) tree saplings, (2) shrubs and small trees and (3) mature trees (Fig. A1).

The tree saplings category (Fig. 6.1, category 1) comprised 122 newly planted broadleaf trees around three metres high, with a maximum
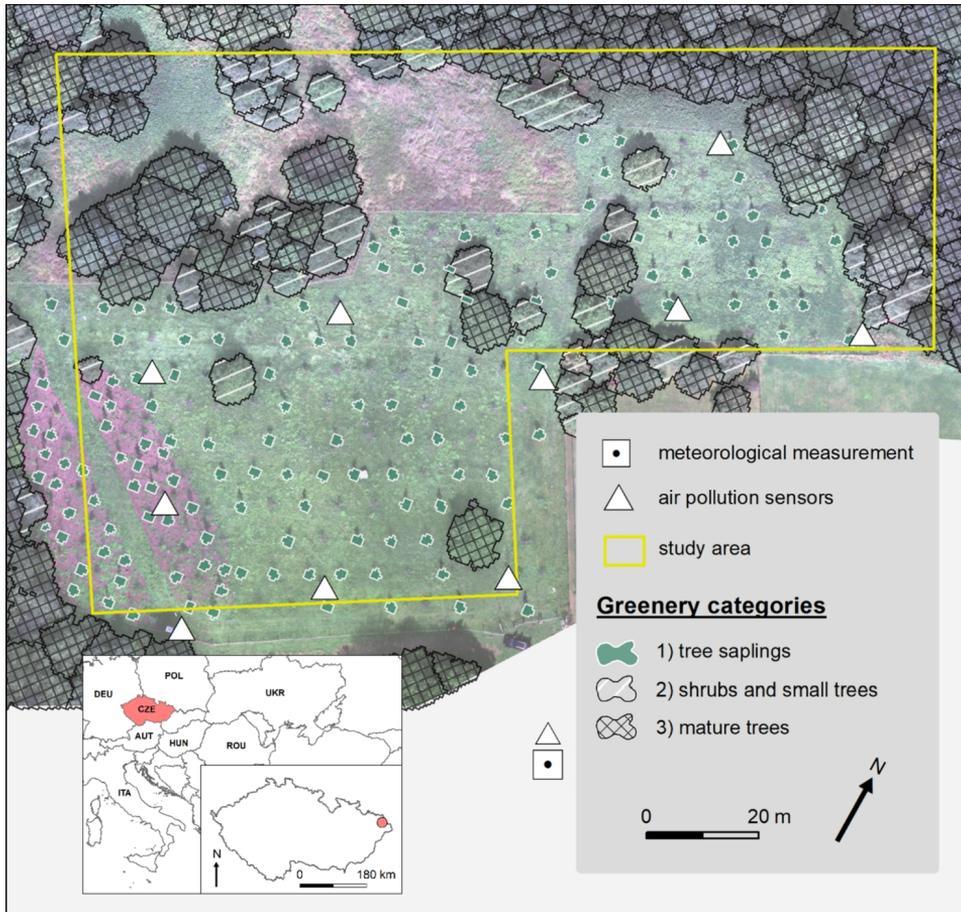
Figure 6.1: Map of the study area with individual tree crowns of different greenery categories. The background represents a UAS-based orthomosaic. Meteorological measurement and one air pollution sensor were located several tens of meters beyond the study area (i.e. outside the orthomosaic)

crown radius of one metre. For original broadleaf woody plants preexisting in the area before planting the saplings, the classification was based on the treetop height (Fig. 6.1). Taking into account local vegetation characteristics, we set the thresholds between 1.5 and 8 m for the category of shrubs and small trees, with all higher treetops classified as mature trees. In this way, we recognized 33 individuals of scattered shrubs and small trees (2) and 64 mature trees (3).

6.2.3 UAS parameters and flight mission

Our modelling approach consisted of several distinct steps (Fig. 6.2). Firstly, we mapped the study area by the UAS. The flight mission was carried out on July 22, 2021, using the DJI Phantom 4 Multispectral, equipped with a multispectral camera measuring the visible to near infrared part of the electromagnetic spectrum. The UAS was operated in a fully automated autopilot-controlled mapping mission mode at the flight altitude of $70-80$ m above the ground. In total, 384 images with an 85 % overlap were taken in each measured part of the spectrum.
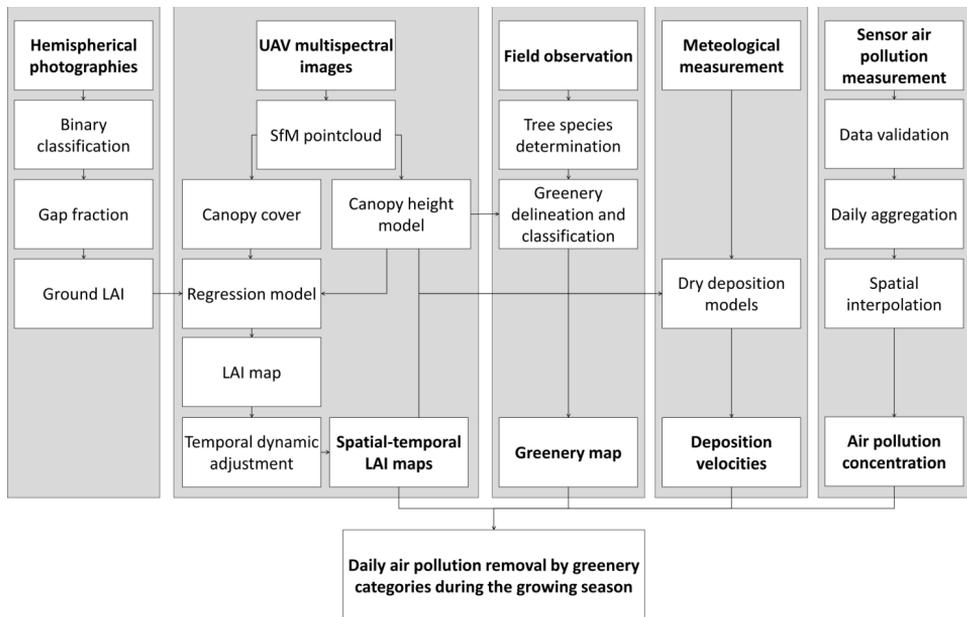
Figure 6.2: The workflow of the study.

Images were matched by MultiView Stereo and SfM methods (Snavely et al. 2008) in Agisoft Metashape, ver. 1.4.2.6205 (Agisoft LLC, St. Petersburg, Russia) into a radiometrically calibrated orthorectified mosaic. The mosaic was georeferenced by four ground control points equally distributed in open areas and surveyed by real-time kinematic positioning (RTK) combined with Global Navigation Satellite Systems (GNSS) Trimble R8s and TSC3.

We processed the point cloud in ultrahigh quality and with two different depth filtering modes. To get the best visual detail of tree saplings (Tinkham and Swayze 2021), we disabled filtering within their area to preserve tie points at their sparsely leafed branches that would be otherwise detected as noise. In all other areas, moderate depth filtering was applied. Finally, we generated a point cloud with a density of 681 points per square metre, further classified into the ground and non-ground points, as fully described by Zhang et al. (2019).

6.2.4 Greenery characteristics

For modelling air pollution removal, we mapped and estimated LAI and canopy height from UAS-SfM data as greenery parametres further incorporated into the dry deposition models. Firstly, we derived in-field LAI from hemispherical photographs and then scaled up these point values into a continuous map based on a multilinear regression model with UAS-based vegetation indices.

Hemispherical photographs were taken at 16 locations using the Canon EOS 7D digital camera with a Sigma 4.5 mm F2.8 EX DC 180° hemispherical lens following standard methodological recommendations (Zhang et al. 2005). The position of each location was surveyed by Trimble R8s and TSC3 with RTK correction.

At each location, we took a series of eight upward-looking hemispherical photographs at about 1 m above the ground, corresponding to established practices (Jonckheere et al. 2004). Hemispherical photographs were pre-processed by converting true colours into grayscale and then classified into binary photographs by applying an automatic thresholding algorithm from Sidelook 1.1 (Nobis and Hunziker 2005). Resultant photographs were processed using the free canopy analysis software CAN-EYE v6.49 (Weiss and Baret 2010), analysing, in accordance with Pfeifer et al. (2012), a limited field of view using angles up to 60° only. The LAI was then acquired by inversion of the exponential expression

of the gap fraction according to the Poisson model (Bréda 2003):

$$P(\theta) = e^{-G(\theta,\alpha) \times LAI / \cos(\theta)} \tag{6.1}$$

where θ is the field of view; α is the leaf angle; $P(\theta)$ is the gap fraction; $G(\theta,\alpha)$ corresponds to the fraction of foliage projected on the plane normal to the zenith direction and equals to 0.5.

To upscale the point value of LAI into spatially continuous coverage, we used two UAS-based structural indices that were previously reported to correlate with LAI from hemispherical photographs − namely, canopy height and canopy cover (Zhang et al. 2019). We also tested the relationship with other metrics and vegetation indices (Fig. A2), but none of those provided as good a fit as the aforementioned two while having low collinearity. Besides, a larger number of predictors would likely lead to model overfitting.

The canopy height model (CHM) was calculated as the difference between a digital terrain model (DTM) and a digital surface model (DSM) at a 0.05 m resolution. Both models were created by interpolation and rasterization of the generated point cloud by SfM algorithm. For DTM, we used only ground points, whereas DSM was interpolated from points classified as vegetation. Canopy height was used both as one of the LAI predictors and independently in the dry deposition ozone model (Erisman et al. 1994).

In addition, *vmf* and *mcws* functions from the R package *ForestTools* (Popescu and Wynne 2004) were applied to the CHM to detect all treetops and delimitate their tree crowns. Firstly, the algorithm scanned the CHM and detected treetops as the highest cells within the moving windows. Then, it implemented the watershed algorithm over the inverted CHM, considering detected tree tops higher than 1.5 m as pour points. In this way, each individual tree crown within the study area was delineated (Fig. 6.1) and for each raster cell, the second LAI predictor, canopy cover, was calculated as a ratio between the area

covered by tree crowns and a total area within a 15 m buffer (Zhang et al. 2019).

Since LAI of the temperate broadleaf trees strongly varies throughout the year (Greco and Baldocchi 1996), we upscaled the LAI grid (Fig. A3) in time. As UAV data were acquired at the peak of the growing season (Fig. A4), the LAI grid derived from the UAV data was considered to represent the maximum values. LAI values for the remaining periods were proportionally calculated from this maximum value and the LAI temporal series curve, which was generated using the *laifromhabitat* function of the *microclima* package in R (Maclean et al. 2019). This function models a temporal LAI variation on hourly basis by fitting a Gaussian curve calibrated using satellite MODIS LAI data for a particular type of habitat, climate and latitude (Yang et al. 2006). The course of thus acquired LAI curve was, in addition, verified through comparison to the NDVI time series trend derived for our study area and period from the Harmonized Landsat and Sentinel-2 surface reflectance dataset (Claverie et al. 2018) (Fig. A4).

6.2.5   Meteorology and air pollution

Meteorological data on air temperature (°C), wind speed (m s^{-1}), air pressure (hPa) and relative humidity (%) from 1st April to 30th September 2021 were based on hourly measurements recorded in the immediate vicinity of the study area (Fig. 6.1). The characteristics of global irradiation (W m^{-2}) in an hourly step were generated from actual weather conditions data using solar radiation time-series of the Copernicus Atmosphere Monitoring Service (CAMS) (Qu et al. 2017).

Air pollution data on O_3 and PM_{10} were measured at 10 min intervals by 11 Cairsens sensors for O_3 (Envea, Poissy, France) and 11 Alphasense OPC-N3 sensors for PM_{10} (Alphasense, Ltd., Braintree, UK), equally distributed within and outside the study area (Fig. 1). Their position was measured by a differential GNSS Trimble R8–2 with RTK correc-

tions. The distance between the sensors was about 20 m. The sensors, embedded in protective boxes, were installed on poles about 4 m above the ground.

The sensors were calibrated by the producers. Additionally, in the beginning, and then repeatedly throughout the measurement, the sensors were validated by on-site reference using a mobile air quality monitoring station based on standard 24-h simultaneous measurements, as documented by Bílek et al. (2021).

To further increase air pollution data reliability, we aggregated PM_{10} and O_3 concentrations from each sensor to hourly averages and then interpolated them within the study area based on the ordinary kriging method of the *gstat* function (Gräler et al. 2016) in the R software. The variogram function used to fit the spatial correlation of the observed concentrations was adjusted for each hour based on the automatic interpolation of the *autofitVariogram* curve of the *automap* package (Hiemstra et al. 2008).

6.2.6   Air pollution removal by dry deposition

To calculate the spatial-temporal series of hourly removal of PM_{10} and O_3 by dry deposition to urban greenery during the growing season (April to September) 2021, we used the equation (Janhäll 2015, Sicard et al. 2018):

$$Q = LAI \times V_d \times C \times t \tag{6.2}$$

where Q was the amount of a particular air pollutant removed by a certain area of greenery (g) in a given hour; LAI was the leaf area index ($m^2 \ m^{-2}$) specific for the hour and day of the year; V_d was the dry deposition velocity (cm s^{-1}); C was the interpolated mean hourly PM_{10} and O_3 concentration (µg m^{-3}); and t was the number of seconds per hour (i.e., 3 600).

Deposition velocity for PM_{10} was modelled according to the Canadian Aerosol Module (CAM) (Zhang et al. 2001), expressed as:

$$V_d = V_g + 1/(R_a + R_s) \qquad (6.3)$$

where V_g was the gravitational settling velocity; R_a was the aerodynamic resistance above the canopy; and R_s was the surface resistance. The aerodynamic resistance R_a was quantified as:

$$R_a = \frac{\ln(z_R/z_0) - \Psi_H}{\kappa} \times u_\star \qquad (6.4)$$

where z_R was the reference height; z_0 was the roughness length; Ψ_H was the stability function; κ was the Von Karman constant and $u_\star$ was the friction velocity, which was calculated from the horizontal wind speed measurements. Here, we distinguished z_R values for different greenery categories, which corresponded to their average canopy heights in the study area ($z_{R(\text{tree saplings})} = 2.5$ m; $z_{R(\text{shrubs and small trees})} = 6$ m; $z_{R(\text{mature trees})} = 15$ m).

The surface resistance R_s, based on atmospheric conditions and surface properties, was calculated as:

$$R_s = (\varepsilon_0 \times u_\star \times (E_B + E_{IM} + E_{IN}) \times R_1)^{-1} \qquad (6.5)$$

where E_B, E_{IM}, and E_{IN} were collection efficiencies from Brownian diffusion, impaction and interception. The value of the empirical constant ε_0 was set to 3 for all greenery categories (Zhang et al. 2001). For other parameters used in the CAM model, we applied values of deciduous broadleaf trees (for mature trees), and shrubs and interrupted woodlands (for shrubs and small trees as well as for saplings) in a midsummer season with lush vegetation (Zhang et al. 2001). The resuspension of the particles after the impact on the surface was modelled by adjusting the overall collection efficiency using a factor of R_1, which represents

the proportion of particles adhering to the surface (Slinn, 1982).

Deposition velocity for O_3 was calculated using the standard resistance analogy, following, e.g., Zapletal et al. (2011):

$$V_d = (R_a + R_b + R_c)^{-1} \qquad (6.6)$$

where R_a was the aerodynamic resistance calculated from micrometeorological relations for the turbulent layer (Baldocchi et al. 1987) and R_b was the laminar layer resistance for the quasi-laminar layer (Baldocchi et al. 1987). For R_c, we used the following equation (Emberson et al. 2001):

$$R_c = (\frac{LAI}{R_{sto}} + \frac{SAI}{R_{ext}} + \frac{1}{R_{inc} + R_{soil}})^{-1} \qquad (6.7)$$

where R_{sto} was the species-specific leaf stomatal resistance to the O_3 uptake through stomata; R_{ext} was the resistance of the external plant parts to the uptake of O_3; R_{inc} was the in-canopy aerodynamic resistance to O_3 transport towards the soil and lower parts of the canopy; R_{soil} was the soil resistance to destruction or absorption of O_3 at the ground surface. The surface area index (SAI) was considered equal to LAI in the growing season.

The in-canopy resistance was modelled based on the formula (Erisman et al. 1994):

$$R_{inc} = \frac{b \times LAI \times h}{u_\star} \qquad (6.8)$$

where h was the vegetation height (m) derived from CHM, b was an empirical constant taken as 14 m^{-1} and $u_\star$ was a friction velocity (m s^{-1}).

Leaf stomatal resistance was calculated according to Emberson et al.

(2000):

$$R_{sto} = \{g_{max} \times g_{phen} \times \max[g_{min}, (g_{light} \times g_{temp} \times g_{VPD} \times g_{SWP})]\}^{-1}$$

(6.9)

where g_{max} was the average maximum stomatal conductance (mmol O_3 m^{-2} s^{-1}) expressed on total leaf surface area. The parameters g_{phen}, g_{light}, g_{temp}, g_{VPD}, and g_{SWP} were expressed in relative terms between 0 and 1, and represented the modification of g_{max} due to phenological changes, light (µmol m^{-2} s^{-1}), air temperature (°C), vapour pressure deficit (kPa), and soil water potential (MPa), respectively. g_{min} was the minimum stomatal conductance that occurred during the daylight period. Full details on parameters and functions used to relate stomatal conductance to environmental variables are given in Emberson et al. (2000).

6.3   Results

6.3.1   Air pollution concentration

Over the growing season (April to September 2021), the mean hourly concentration at the 11 sensors was 26.7 µg m^{-3} for PM$_{10}$ and 80.9 µg m^{v-3} for O_3, respectively. The maxima of PM$_{10}$ and O_3 were 120 µg m^{-3} and 221 µg m^{-3}, respectively. The limit value (50 µg m^{-3}) for 24-h mean PM$_{10}$ concentration was exceeded in 10 days. The daily maximum of 8-h running average of O_3 exceeded the legislative standard for the protection of human health (120 µg m^{-3}) in 54 cases.

Seasonal and diurnal cycles of PM$_{10}$ and O_3 concentrations (Fig. 6.3) well capture the long-term and daily trends of these types of pollution with high concentrations of PM$_{10}$ in the heating season (here reflected by higher values in April) and high concentrations of O_3 in summer in response to the photochemical reactions. The relationship between

O_3 concentrations, air temperature and solar radiation resulted in O_3 buildup around noon with a decrease in the night and the lowest value in the early morning.
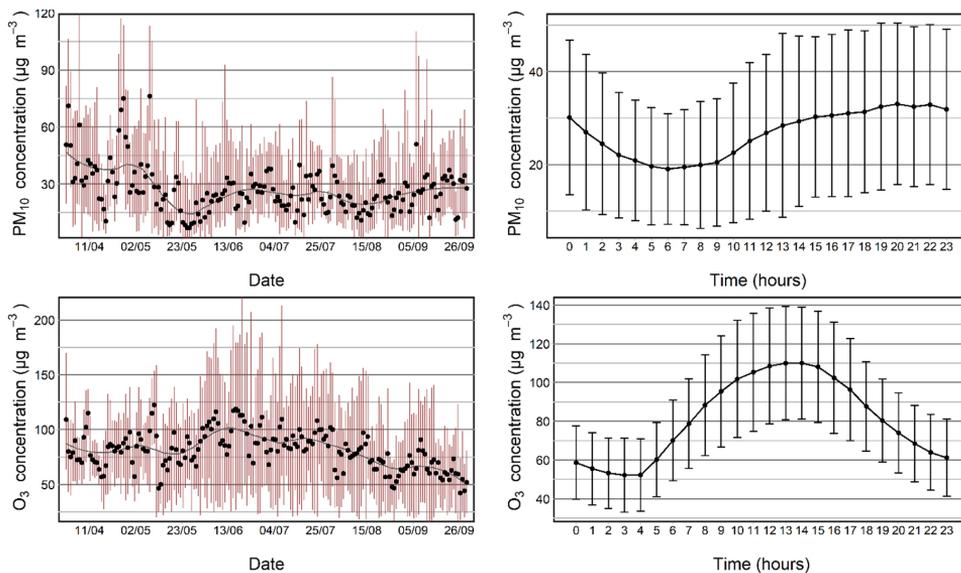
Figure 6.3: Seasonal (left) and diurnal (right) trends of PM_{10} (upper) and O_3 (bottom) concentrations in the study area. Left: Trend of daily means (black dots), minimum and maximum (red scatters) concentrations. The black line indicates the rolling seven-day average. Right: Average 24-hour concentrations. The hourly variability of the values indicates one standard deviation around the mean (error bars). Time is given in the local standard clock time (Central European Summer time).

6.3.2 Leaf area index

LAI values derived from hemispherical photographs ranged between 0.2 and 4.3 m^2 m^{-2} (Fig. A3). Low values were observed in open canopies or crown edges of tree saplings. High values were, on the other hand, observed under canopies of mature trees. The linear regression model expressing LAI as a function of canopy height and canopy cover as predictor variables produced highly correlated results with Adj. $R^2 =$

0.82 (p < 0.005), RMSE = 0.58 for the generated regression function:

$$LAI = 4.156 \times \text{canopy cover} + 0.174 \times \text{canopy height} \qquad (6.10)$$

The spatially continuous LAI map, modelled on the basis of this equation, captured the distribution of individual greenery categories well (Fig. A3). In the peak season, the highest modelled LAI values (8.8) were observed in closed-canopy stands of mature trees, while the lowest (0.3) were found in the sparse foliage of tree saplings (Fig. 6.4). However, considerable LAI variability was documented within greenery categories and over the growing season, especially among individual mature trees (Fig. 6.4).
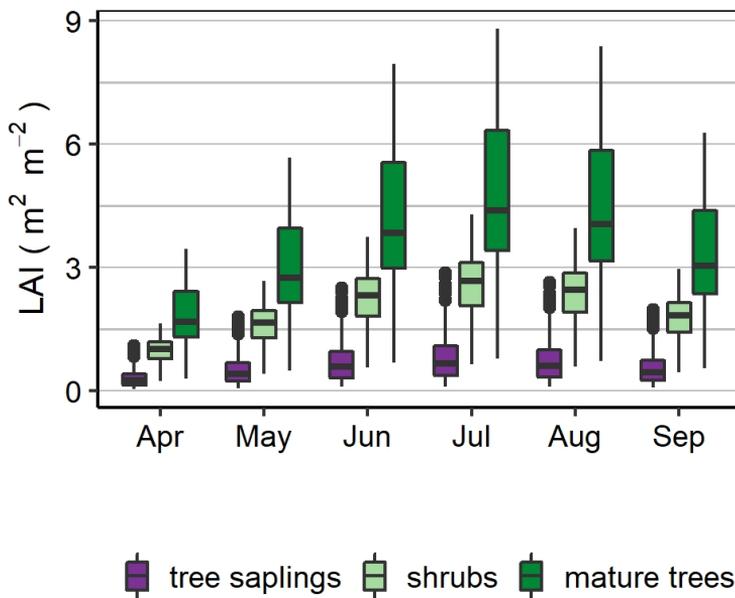
Figure 6.4: Temporal dynamics of monthly mean LAI (m^2 m^{-2}) by greenery categories modelled by fitting the UAS-derived LAI (acquisition in the peak season) to the habitat, climate and latitude-dependent Gaussian curve of the LAI time series calibrated by satellite MODIS data (Maclean et al. 2019) and further validated by NDVI phenology from the Harmonized Landsat and Sentinel-2 surface reflectance data set (Claverie et al. 2018) for a given study area and period (Fig. A4).

6.3.3 Air pollution removal by different greenery categories and plant species

The PM_{10} and O_3 removal by dry deposition during the growing season within the study area totalled 17.6 kg and 25.9 kg, respectively. Mature trees, due to their higher total leaf area and overall higher deposition velocity, achieved the highest total removal rates per plant cover (Table 6.1). On the other hand, saplings showed the lowest total removal rates, mainly due to the significantly lower total leaf area compared to other categories.

When differentiated by woody plant species (Table 6.2), the highest removal rates were calculated for mature trees of *Acer pseudoplatanus* (PM_{10} - 7.6 g m^{-2}, O_3 - 12.6 g m^{-2}), *Alnus glutinosa* (PM_{10} - 6.4 g m^{-2}, O_3 - 9.8 g m^{-2}) and *Fraxinus excelsior* (PM_{10} - 6.2 g m^{-2}, O_3 - 9.6 g m^{-2}).

Conversely, the lowest removal rates were recorded for tree saplings of *Ulmus laevis* (PM_{10} - 0.3 g m^{-2}, O_3 - 0.2 g m^{-2}) and *Salix daphnoides* (PM_{10} - 0.1 g m^{-2}, O_3 - 0.1 g m^{-2}). These values were, however, determined rather by the structural quantities of individual canopies than by species-specific leaf properties, and, thus, considerably differed also among individuals of the same species in different life stages (Table 6.2).

6.3.4 Spatial and temporal dynamics of air pollution removal

The daily averages of PM_{10} and O_3 removal rates showed very different temporal patterns (Fig. 6.5). While values of removal rates in PM_{10} did not follow any apparent trend and were characterized by relatively smaller differences among greenery categories, and by abrupt inter-day changes, daily removal rates of O_3 corresponded to the seasonal

changes in LAI (Fig. 6.4) and O_3 concentrations (Fig. 6.3) and featured a distinctive peak between mid-June to end-July, when removal rates among categories differed most.

While absolute values of total removal varied according to air pollutants and greenery categories, the spatial patterns of both PM_{10} and O_3 removal rates were similar (Fig. 6.6) because the main determinants, i.e. LAI and woody plants distribution, remained unchanged. Fig. 6.6 shows a spatial pattern of total removal rates, clearly distinguishable according to greenery categories. While the highest total removal rates were modelled in the northern part of the study site with the dominance of mature trees, the lowest values corresponded to the irregular network of the newly planted tree saplings. Due to high spatial resolution, it was further possible to distinguish the differences in removal rates even within individual tree crowns (Fig. 6.6). The highest removal rates roughly corresponded to the central parts of the tree crowns and then decreased towards the tree crown edges, where LAI also decreased (Fig. A3).
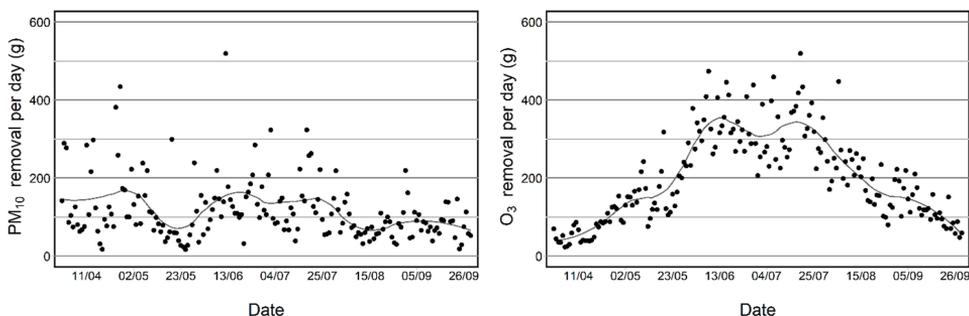
Figure 6.5: Temporal dynamics of daily PM_{10} (left) and O_3 (right) removal rates per square meter of plant cover (g m^{-2}) of different urban greenery categories in the study area. The lines indicate the rolling 7-day average.
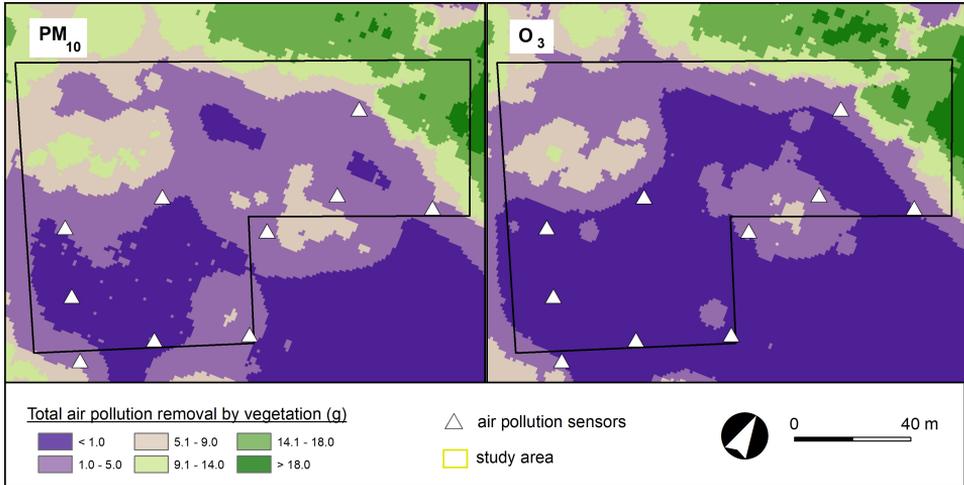
Figure 6.6: Total removal rates (g m^{-2}) of PM$_{10}$ (left) and O$_3$ (right) per square meter of plant cover in a 1 × 1 m grid during the growing season 2021.

6.4 Discussion

Based on physical models of dry deposition processes (Emberson et al. 2001, Zhang et al. 2001), the presented study evaluates the removal of the particulate matter and tropospheric ozone by several woody plant species in different life stages in a highly polluted area. We applied a spatially explicit approach (Fig. 6.2) based on the integration of high-resolution UAS-SfM products with GIS analysis (Fig. A3) and spatial interpolation of air pollution concentration data (Fig. 6.3) measured by low-cost optical and electrochemical sensors (Fig. 6.3). This enabled modelling of the deposition processes in more detail and, thus, shifted the estimation of air pollution removal by urban greenery from land-cover scheme towards species- (Table. 6.2) and individual-specific levels (Fig. 6.6).

The resulting air pollution removal by urban greenery (Fig. 6.5) was determined as an interaction of air pollutant concentrations, micrometeorological conditions, and vegetation properties (Yang et al. 2008). Our results confirmed that high and dense canopies of mature trees capture

air pollutants better than sparse and low shrubs and tree saplings (Yang et al. 2008). This was mainly due to large differences in LAI (Fig. 6.4) and deposition velocities (Table 6.1), the latter being, besides other factors, driven by differences in surface roughness (Zhang et al. 2001) as well as surface and in-canopy resistances (Emberson et al. 2000). As the leaf area changed over the growing season, so did the differences in modelled air pollution removals among greenery categories; this was particularly pronounced in the mid-summer when large canopies featured lush foliage (Fig. A4).

Comparing our results with those of other studies in corresponding climate zones (Table. 6.3), standardized removal rates mostly fell within reported ranges with slightly higher values for O_3 due to the generally higher O_3 concentrations (Fig. 6.3), confirming the severity of the local air quality in the European context (Pokorná et al. 2015). Additionally, our results were characterized by relatively high variability of PM_{10} and O_3 removal rates, with both lower minima and higher maxima than in available studies shown in (Table. 6.2). Such a wide range may be mainly attributed to the higher variance of the LAI parameter (Table. 6.2) which enters the model separately (Eq. 6.2) and plays an important role. Unlike in our study, the methods used to derive the total leaf area in previous papers mostly assigned constant LAI values to entire forest stands, regardless of their spatial variability and seasonal changes (Nowak et al. 2006, Tallis et al. 2011). Disregarding this LAI heterogeneity might have led to the greater uniformity of calculated removal rates, reflected in narrower ranges of values (Sicard et al. 2018). In contrast, because of the high spatial resolution of UAS-SfM derived vegetation indices, we were able to extract fine structural characteristics from individual trees and even within their crowns. Thus, we could, for instance, differentiate between the marginal air pollution removal on sparsely leafed edges of tree crowns from considerably higher capture in dense, multi-layered centres of tree crowns (Fig. 6.6).

Vegetation properties were further involved in modelling deposition ve-

locities (Emberson et al. 2001, Zhang et al. 2001), influencing the roughness length (Hicks et al. 1987) and, even more significantly, the surface resistance and leaf surface efficiency (Zhang et al. 2001), as well as the leaf stomatal resistance to O_3 uptake (Emberson et al. 2000). Most commonly, these processes are modelled according to land cover types (Emberson et al. 2001, Zhang et al. 2001, Zapletal et al. 2011); however, deposition velocities strongly differ also with plant species (Mitchell et al. 2010). Therefore, reported deposition velocities vary between studies, depending on the assumed parameters and complexity of the deposition model used. In our study, vegetation parameters derived from UAS-SfM were used for modelling processes dependent on the plant macromorphology (e.g. R_{inc}); however, generic values proposed by Zhang et al. (2001) and Emberson et al. (2000) were used for other components of surface resistance determined by leaf traits (e.g. R_s and R_{sto}). Although, deposition velocities calculated from our models were within the range reported in the literature (Yang et al. 2008, Zapletal and Chroust 2007), we are aware of the shortcomings resulting from the leaf surface parameters used in models. Therefore, our results should not lead to hasty conclusions concerning the selection of plant species according to their removal efficiency modelled in our study. For these purposes, we refer to other studies (Sæbø et al. 2012).

Canopy architecture of urban greenery thus controls both the dry deposition velocity and air pollution removal (Table. 6.1). This emphasizes the crucial need to incorporate greenery's spatial detail and temporal variation in the modelling of urban forest impacts on air quality (Sicard et al. 2018). Here, we demonstrated a remote sensing approach that addresses these requirements by photogrammetric reconstruction of canopy height and upscaling ground-based LAI measurement through UAS-SfM-derived vegetation indices. In contrast to similar studies in which satellite imagery (Manes et al. 2016) or aerial LiDAR (Bottalico et al. 2017) were used for modelling air pollution removal, this study showed that the UAS-SfM approach offers: (1) greater operational

flexibility that allows weather or task-based timing, (2) efficient and affordable data collection and processing suitable for periodic inventory monitoring by urban planners and municipal authorities and (3) finer spatial resolution (several cm) allowing the capture of fine structures within canopies and the detection of small vegetation patches or individual trees, typical for urban areas. Acquisition of vegetation parameters at such a high detail may lead to more realistic estimates of air pollution removal as the deposition-modelling algorithms will newly reflect spatial heterogeneity of urban canopies.

Another great advantage of UAS-SfM, considering its low acquisition costs, is the opportunity to sense imageries during the year repeatedly and so to monitor plant phenology and seasonal changes in LAI (Klosterman and Richardson 2017). Temporal LAI variation was simulated using many approaches (Tallis et al. 2011, Alonso et al. 2011), but none of them described LAI seasonal changes continuously. In our study, we determined the time-dynamic LAI from the LAI data curve calibrated by MODIS data, the spatial resolution of which may seem too coarse this case. However, it was based on inferred changes in the spectral reflectance of vegetation in a particular habitat and latitude and further validated by NDVI phenology from the Harmonized Landsat and Sentinel-2 surface reflectance dataset (Claverie et al. 2018) for a given study area and period (Fig. A4), which, in our opinion, justifies this choice. Still, we would like to emphasize the possibility of repeated UAS flights throughout the growing season for future studies, which may provide a near-continuous observation of seasonal variation in LAI and other vegetation parameters. Taking such inputs into account would further clarify the temporal dynamics of removal rates, particularly among phenologically variable woody plant species.

These UAV-SfM benefits are mostly well-known, but we would like to point out that our study shed light also on some limitations. One of these was the detection of very small objects, such as low and sparsely leafed tree saplings, which may be considered random noise by

the filtering algorithm and removed when generating a point cloud. This issue led to difficulties in DSM construction, undervalued canopy heights and, ultimately, to the calculation of negligible air pollution removal in the areas with tree saplings (Table. 6.2). Disabling the filtering mode during point cloud processing partially solved this problem; however, for some species (*Ulmus laevis*) of tree saplings, the overall removal rates were, in comparison with reported values (Sicard et al. 2018), still lower (Table. 6.3). A potential solution for better quantification of low vegetation may lie in changing the flight mission setting (Isibue and Pingel 2020) and off-nadir (oblique) image acquisition (Díaz et al. 2020). Therefore, UAS-SfM may seem far more suitable for mapping mature trees since dense foliage facilitates the matching of detected features across the images. However, in closed-canopy forests, incorrect detection of the gaps between and within canopies can pose a problem leading, ultimately, to the canopy cover and canopy height overestimation. UAS-mounted LiDAR sensor provides a potential solution in these conditions thanks to its ability to penetrate through the canopies (Kašpar et al. 2021), but the use of this technology significantly increases the acquisition costs. On the other hand, urban greenery is typically formed rather by scattered solitary high trees such as alleys, parks and English landscape gardens rather than dense forests. In such environment, even the SfM method can be highly suitable for woody plant mapping or even the classification of individual species of plants (Komárek et al. 2018), which may allow a complete substitution of the laborious field inventory.

Apart from the quantification of structural variables of tree canopies, the UAS approach may be potentially used to acquire micromorphological features of individual leaves (Duffy et al. 2021). Parameters of leaf properties, such as leaf size, surface roughness or leaf distribution are required for accurate modelling of micrometeorological processes as well as surface and leaf stomatal resistances (Eqs. 6.5, 6.9). Despite the first promising studies exploring the measurement and acquisition

of leaf traits from UAS-derived products (Brewer et al. 2022, Kim et al. 2018), further technological progress in sensors and research expansion into urban forestry applications will be needed. Additionally, with the potential emergence of the methods for mapping detailed leaf arrangement and morphologies, new species-specific modifications in dry deposition models, especially in the surface resistance component, will be also required (Sicard et al. 2018).

Despite these challenges, UAS-SfM elevates the modelling of air pollution removal by urban greenery from the level of land cover to the level of species and beyond. Combined with the low-cost sensors for air pollution monitoring (Kumar et al. 2015), the decision-making of urban planners and local authorities can now rely on data that is both detailed and spatially extensive.

6.5 Conclusions

Our study presents a novel approach that incorporates local-scale and seasonal variability of canopy structure into modelling of urban greenery's impact on air quality. We demonstrated that UAS-SfM-based remote sensing enabled deriving of high-quality data on urban greenery, respecting differences in LAI and canopy height values within crowns of woody plants. Combined with a dense network of PM_{10} and O_3 air pollution sensors, these inputs advanced the modelling of deposition velocities and air pollution removal by urban greenery towards speciesand individual-specific levels. Thus, our results revealed a high spatial heterogeneity of modelled air pollution removal rates among various species and life stages of woody plants as well as substantial temporal dynamics determined by changes in phenology, air pollution concentration and meteorological conditions. For urban applications, where the vegetation often consists of individual solitaire trees or shrubs, detection of small vegetation features by UAV may provide a more

accurate and realistic estimation of air pollution removal by urban greenery. Spatially-focused but extensive information on the removal rates may further help urban planners and municipal authorities to, for instance, make the right decisions regarding tree selection and greenery planting for air pollution reduction in cities worldwide.

Supplementary materials

Supplementary material associated with this article can be found, in the online version, at https://doi:10.1016/j.ufug.2022.127757.

Table 6.1: *Summary of the calculated LAI (m^2 m^{-2}) and total leaf area (m^2) values, as well as the PM_{10} and O_3 mean deposition velocities (cm s^{-1}) and removal parameters over the study period (totals in kg and rates per square meter of plant cover in g m^{-2}) by the different categories of urban greenery in the study area. The LAI column indicates the mean and range of LAI for each greenery category at the peak of the growing season. The total leaf area represents a maximum value for each category at the peak of the growing season (note, however, that these two values vary over time, see Fig. 6.4)).*

| Greenery category | LAI | total leaf area | PM$_{10}$ | | | O$_3$ | | |
| | | | deposition velocity | removal rate | total removal | deposition velocity | removal rate | total removal |
	(m^2 m^{-2})	(m^2)	(cm s^{-1})	(g m^{-2})	(kg)	(cm s^{-1})	(g m^{-2})	(kg)
tree saplings	0.8 (0.3 − 2.9)	309.1	0.20	0.52	0.19	0.04	0.52	0.19
shrubs and small trees	2.6 (1.6 − 4.3)	2367.8	0.27	2.19	1.97	0.10	3.06	2.75
mature trees	4.8 (2.4 − 8.8)	13,590.0	0.37	5.49	15.45	0.14	8.15	22.93

Table 6.2: Summary table of canopy height (m), LAI ($m^2\ m^{-2}$), total leaf area (m^2) and the PM_{10} and O_3 removal characteristics (totals in g and rates in g m^{-2} per square meter of plant cover) for different woody plant species. Values of canopy height and LAI indicate the means and ranges (in brackets) within plant species at the peak of the growing season. Canopy height is expressed as the maximum treetop height of each individual derived from the UAS-SfM-based canopy height model. The total leaf area represents a maximum value for each category at the peak of the growing season. Greenery category: TS – tree saplings, S ˅ shrubs and small trees, M ˅ mature trees. Species with less than four individuals were excluded.

Plant species	number of individuals	greenery category	canopy height (m)	LAI ($m^2\ m^{-2}$)	total leaf area (m^2)	PM_{10} removal rate ($g\ m^{-2}$)	PM_{10} total removal (g)	O_3 removal rate ($g\ m^{-2}$)	O_3 total removal (g)
Acer negundo	6	S	6.5 (4.9 – 7.6)	3.8 (3.0 – 4.5)	745.7	2.3	503.5	3.2	701.0
Acer pseudoplatanus	25	TS	2.8 (1.3 – 4.6)	1.1 (0.3 – 2.9)	116.2	0.6	40.4	0.6	44.7
Acer pseudoplatanus	9	M	19.1 (8.8 – 26.5)	7.1 (4.6 – 8.8)	1938.7	7.6	1895.1	12.6	3156.0
Alnus glutinosa	29	M	16.4 (9.9 – 21.6)	6.2 (3.9 – 7.7)	3686.2	6.4	3374.4	9.8	5183.1
Crataegus monogyna	6	S	5.3 (3.4 – 6.2)	2.8 (1.6 – 4.3)	283.8	1.7	199.4	2.0	240.4
Fraxinus excelsior	6	M	17.8 (9.5 – 25.5)	6.0 (4.3 – 8.1)	3165.7	6.2	3262.4	9.6	5047.2
Juglans regia	8	M	9.9 (8.0 – 13.4)	3.6 (2.4 – 4.9)	1310.8	3.1	1269.8	3.4	1406.2
Populus nigra	17	TS	1.4 (1.2 – 1.8)	0.7 (0.3 – 2.0)	38.6	0.4	17.6	0.3	14.1
Prunus spp.	12	S	6.2 (4.9 – 7.6)	3.2 (1.9 – 4.5)	713.1	2.4	454.0	3.4	653.8
Quercus petraea	46	TS	2.1 (1.2 – 3.4)	1.0 (0.3 – 2.8)	201.1	0.6	80.1	0.6	82.0
Salix caprea	10	M	10.9 (8.1 – 21.1)	4.9 (3.8 – 7.7)	3355.9	4.9	3316.8	6.7	4562.9
Salix daphnoides	5	TS	2.0 (1.3 – 3.9)	0.4 (0.3 – 0.6)	7.4	0.1	2.4	0.1	1.0
Tilia platyphyllos	23	TS	2.4 (1.2 – 6.0)	1.1 (0.4 – 2.5)	107.1	0.6	39.8	0.7	44.7
Ulmus laevis	6	TS	1.9 (1.3 – 4.2)	0.5 (0.3 – 1.3)	13.9	0.3	4.8	0.2	2.8

Table 6.3: The comparison of modelled annual air pollution removal rates per square meter of plant cover (g m^{-2}) and standardized to the mean concentration (g m^{-2} per ppb) in several world cities. In our study, removal rates indicate values for the growing season only. However, the dry deposition is severely limited in the leaf-off season, and, hence, with a certain simplification, the growing season values can be considered equal to annual ones. Only cities with similar climate types (Cfb or Dfb) are listed in this table.

City	Climate	Model	Plant cover (ha)	PM$_{10}$ removal rate (g m^{-2})	PM$_{10}$ removal rate (g m^{-2} per ppb)	O$_3$ removal rate (g m^{-2})	O$_3$ removal rate (g m^{-2} per ppb)	References
Berlin (DE)	Cfb	i-Tree Eco	38,048	4.4	0.15	5.1	0.11	Baró et al. (2015)
London (GB)	Cfb	Tiwary	31,265	2.7 − 6.8	–	–	–	Tallis et al. (2011)
Roanoke (US)	Cfb/Cfa	UFORE	–	1.6 − 6.3	–	1.1 − 5.8	–	Nowak et al. (2006)
Rotterdam (NL)	Cfb	i-Tree Eco	3343	3.1	0.11	2.5	0.07	Baró et al. (2015)
Strassbourg (FR)	Cfb	i-Tree Eco	1342	0.6 − 6.9	–	2.8 − 7.0	–	Selmi et al. (2016)
Buffalo (US)	Dfb/ Dfa	UFORE	–	0.8 − 3.3	–	0.9 − 4.3	–	Nowak et al. (2006)
Salzburg (AT)	Dfb	i-Tree Eco	1878	2.4	0.10	0.1	0.00	Baró et al. (2015)
Stockholm (SE)	Dfb	i-Tree Eco	8093	2.9	0.10	3.4	0.06	Baró et al. (2015)
Ostrava (CZ)	Cfb/ Dfb	CAM/ Emberson	0.4	0.1 − 7.6	0.00 − 0.28	0.1 − 12.6	0.00 − 0.16	this study

Chapter 7

From orbit to forest understorey: Spatial-temporal relationships between canopy surface temperature and air and soil temperatures in the forest interior

Vít Kašpar, Lucia Hederová, Martin Kopecký, Jan Wild

Unpublished manuscript

7.1 Introduction

Forests are complex ecosystems that play a critical role in regulating the Earth's climate and supporting the world´s biodiversity (Nakamura et al. 2017). The microclimate of a forest is a key factor in its functioning as it influences numerous ecological processes, such as photosynthesis, transpiration, and decomposition (Geiger et al. 1995). Understanding the microclimate of a forest is therefore crucial for predicting how it will respond to climate change and for developing effective management strategies (De Frenne et al. 2021, Suggitt et al. 2018).

Remote sensing (RS) has become an increasingly applicable tool for studying forest microclimate (Bramer et al. 2018, Zellweger et al. 2019b), as it allows researchers to gather data over large areas and across different temporal and spatial scales. Previous studies have used topographic and vegetation RS-derived indices to upscale in situ microclimatic loggers (Jucker et al. 2018, Greiser et al. 2018, Davis et al. 2019) or downscale macroclimate reanalysis based on weather station records (Haesen et al. 2021, Lembrechts et al. 2022). To do so, they mainly used spectral or structural data on forest canopy properties derived from passive or active RS sensors (Kašpar et al. 2021).

Another source of information represents thermal infrared RS data, which allows the measurement of land surface temperature (LST) at the canopy surface, which is an important indicator for understanding the mechanisms that govern energy exchange between the atmosphere and the forest ecosystem (Jarvis and McNaughton 1986). Thermal-derived LST can be obtained from various RS data, such as aerial surveys (Junttila et al. 2017, Zakrzewska et al. 2022), or satellite imageries (Neteler 2010, Metz et al. 2017), and allows capturing the spatial variability of canopy temperature over large spatial scales.

Nevertheless, this data has been rather neglected in forest microclimate modelling so far, although it can be a valuable determinant for

modelling understorey temperature (Maclean and Klinges 2021). Moreover, the favourable open data policy of the European Space Agency or NASA provides satisfactory products, such as MODIS, which enable monitoring of almost daily surface temperatures in remote and difficult-to-access areas (Meyer et al. 2016). Some previous studies have attempted to explore the relationship between temperatures below and at the forest canopy (Laskin et al. 2017). However, this link is more complex and not sufficiently well understood as it is influenced by a range of factors, such as solar radiation, wind speed, and vegetation structure (Leuzinger and Körner 2007, Richter et al. 2021).

Furthermore, these studies mainly focused on the temperature at only one level below the forest canopy (Haesen et al. 2021) and neglected substantial vertical temperature variation inside forests. Below-canopy temperature gradients vary enormously over short vertical distances and during the day (Hardwick et al. 2015, Davies-Colley et al. 2000), as vegetation elements affect radiation fluxes into and out of forests as well as decrease the turbulent air mixing (Chen et al. 1993, 1999).

Additionally, they mostly modelled daily (Laskin et al. 2017, Hengl et al. 2012) or seasonal temperature means (Zellweger et al. 2019a), despite their questionable biological meanings (Körner and Hiltbrunner 2018). For a description of habitat conditions, temperature extremes can be more appropriate, driving responses in species diversity and distribution (Macek et al. 2019).

This study aims to address some of these issues by exploring the spatial-temporal pattern of differences in temperature extremes between canopy surfaces derived by satellite RS and multiple in situ measurements within forest understorey. Specifically, we will attempt to find answers to the following questions:

1) What is the relationship between above-canopy and below-canopy temperatures? How do temperature differences change during the day and season and depending on the position measured under the forest canopies?

2) How do remotely sensed factors of canopy structure and topography influence these temperature differences, especially during seasonal temperature extremes?

7.2 Materials and Methods

7.2.1 Study area and T_{bc} observation plots

Below-canopy temperature (T_{bc}) was observed in 56 evenly distributed observation plots located throughout Czechia, covering an area of nearly 79,000 km² (see Fig. 7.1). The plots were placed along an elevation gradient (214 – 1,029 m a. s. l.) to encompass an array of temperature variability, and this distribution ensured a diverse range of slope (0 – 32°), canopy openness (5 – 37 %), and forest composition types (dominant species: *Picea abies*, *Pinus sylvestris*, *Fagus sylvatica*, *Quercus sp.*).

Within each plot, four sub-canopy TMS sensors (Wild et al. 2019) – in the soil (-8 cm), on the ground (2 cm), near the ground (15 cm) and above (2 m) were placed to record temperatures at 15-minute intervals throughout the year 2018 (Fig. 1). Firstly, all time series were plotted and visually checked for obvious outliers biased by temporary device malfunction or misplacement. Then, we aggregated the hourly temperature data to derive two daily temperature statistics: the 5th percentile of minimum, and the 95th percentile of maximum daily temperatures for each plot and each vertical position separately. We used rather percentile values instead of potentially biased absolute extreme values

in accordance with ecologically-oriented microclimatic studies (Ashcroft and Gollan 2013, Macek et al. 2019). These aggregated daily temperatures measured below the forest canopy were subsequently compared with the temperature at the canopy surface derived by satellite RS.
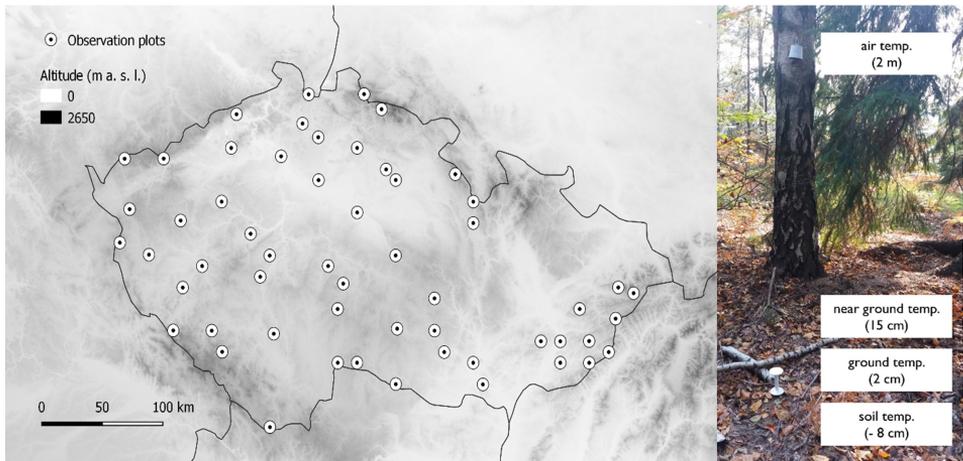
Figure 7.1: The map of all 56 observation sites within Czechia. In the background, the digital terrain model illustrates an elevation gradient at which sites were located (left). At each site, four below-canopy temperatures in different vertical positions were measured (right).

7.2.2 Satellite-derived canopy surface temperature

In the next step, thermal satellite products were processed in the Google Earth Engine (GEE) platform that combines a multi-petabyte catalogue of satellite imagery and geospatial datasets with planetary-scale analysis capabilities (Gorelick et al. 2017). We processed an image collection of MODIS Terra and Aqua products (Aqua MYD11A1; Terra MOD11A1; level V006). These satellite products by NASA provide LST in a 1000 x 1000 meter grid since the year 2000 and with a four-time per-day time step (https://lpdaac.usgs.gov/products/mod11a1v061/).

All pixels with an LST error > 3 K and emissivity error > 0.02 were filtered out using the corresponding MODIS LST QA layers (quality assurance layers), similar to (Laskin et al. 2017, Metz et al. 2017). We

used this rather liberal threshold because preliminary tests showed that a lower threshold for LST error would also discard LST values that appear to be correct (Metz et al. 2017). Therefore, we decided to keep potentially valid LST values at the expense of including more outliers. Outlier filtering was performed at the final stage.

Because the time of LST observation was given in local solar time that slightly differs from clock time used in T_{bc} measurements, it had to be modified by (1) the relationship between the local time zone and the local longitude, (2) daylight savings time, and (3) the earth's slightly-irregular motion around the Sun (Laskin et al. 2017). The median time records of LST at all localities were thus 2:18 (AQUA night), 11:12 (TERRA day), 12:48 (AQUA day), 21:54 (TERRA night) UTC+1. Since T_{bc} were recorded in a 15-minute step, we rounded LST times to the nearest quarter of an hour.

A problematic step when working with satellite data is the frequent cloud cover, which does not allow the capture of LST in every single observation (Laskin et al. 2017, Neteler 2010). Because of cloud cover and the defined threshold for LST error, in 67.1 % of cases, LST values were missed (Supp. Fig. 1), mainly in the winter months. Similarly to Laskin et al. (2017), Metz et al. (2017), we filled the time series by temporal interpolation of neighbouring values. An algorithm was developed to search the 5 days preceding and following a date with a cloud gap, separately for day and night records. A Gaussian average was then used to impart more weight to dates closer in time to the gap being filled (Supp. Fig. 1).

Finally, we converted the individual measurements to daily temperature statistics when AQUA night LST values equalled minimum daily temperatures, and TERRA day LST values were considered as maximum daily temperatures.

7.2.3 Differences between above and below canopy temperatures

To explore differences between above- and below-canopy temperatures, we subtracted LST from daily T_{bc} records. To eliminate a misused of outliers, we removed values that were 1.5 standard deviations below the average minimum and maximum temperature for that month (Metz et al. 2017), which originated as an appendix of temporal interpolation or liberal quality criteria of satellite imageries (Supp. Fig. 1). Temperature differences were then aggregated into monthly average differences (Zellweger et al. 2019a) to quantify seasonal in temperature buffering of forest canopies.

7.2.4 Environmental predictors of temperature differences during seasonal extremes

In the second part, we tried to explore how RS factors of canopy structure and topography influence temperature differences between LST and T_{bc} during seasonal extremes. We calculated the 95th percentiles of daily maximum temperatures in T_{bc} during vegetation season (May – September), as representatives of relatively short episodes with high relevance for forest plant distribution and composition (Ashcroft and Gollan 2013, Macek et al. 2019). Subsequently, we calculated the difference between these 95th percentiles of daily maxima in T_{bc} and TERRA day LST, hereafter referred to as T_{max} differences.

We tried to explain T_{max} differences by several environmental predictors using stepwise linear multivariate regression. To avoid model overfitting, we used only six predictors based on their relevance according to the literature (Greiser et al. 2018) and data availability from only public sources at maximal geographical extent. For each model, an additional sub-choice of predictive variables was carried out by bidirectional AIC

selection using *stepAIC* function from R package *MASS* (Ripley et al. 2013).

For a topographic factor of elevation (Table. 7.1), we used the digital elevation model (DEM) over Europe EU-DEM v1.1. in 25-metre spatial resolution (EU-DEM, 2018). From this dataset, we further derived two topographic factors using SAGA GIS software (Conrad et al., 2015) - slope radiation and topographic position index (TPI) calculated as the difference between plot elevation and the mean elevation of the surrounding terrain within 250 m. Whereas solar radiation estimates potential incoming solar energy considering surface inclination and orientation, shadows cast by terrain features and local coordinates (Böhner and Antonić 2009), TPI analyses a DEM to locate flat valley bottoms and concave areas where cold-air pools are likely to form (Curtis et al. 2014).

Vegetation factors included both spectral and structural parameters of the tree canopy (Table. 7.1). We used the 2018 high-resolution (20 m) Copernicus maps of tree cover density (%), which referred to the percentage of tree cover per raster cell. For canopy height (m), we utilized a new 30-m spatial resolution global forest canopy height map based on the integration of the Global Ecosystem Dynamics Investigation (GEDI) and Landsat analysis-ready data time series (Potapov et al. 2021). The third parameter included a standard NDVI index derived from satellite data of the Sentinel-2 mission in 10-metre pixels to express health status and phenology. We calculated a median reflectance value of red and near-infrared bands between June and August 2018 from cloud-masked imageries processed in the GEE code editor.

To explore the relative importance of the topographic and vegetation factors in each fitted model, we partitioned the explained variance among these predictor groups and their shared effect with *varpart* function from the *vegan* R package (Oksanen et al. 2013).

Table 7.1: Summary of environmental predictors, their description and range of values.

	Predictor	Unit	Description	Range (mean)
TOPOGRAPHY	Elevation	m	Elevation above sea level	215.1−1030.1 (538.1)
	Solar radiation	-	An indicator of potential incoming solar radiation	0.01−0.56 (0.16)
	Topographic position index (TPI)	-	Relative topographic position describing the plot elevation in relationship to the surrounding elevations	-3.12−3.42 (0.30)
VEGETATION	Normalized vegetation index (NDVI)	-	An indicator of the vegetation greenness by spectral bands proportion	0.28−0.92 (0.81)
	Canopy height	m	Forest canopy height developed through the integration of the GEDI LiDAR forest structure measurements and Landsat time-series (Potapov et al. 2021)	3.0−31.0 (23.39)
	Canopy density	%	The proportion of an area in the ground that is in vertical projection covered by the crown of trees	62.0−99.0 (82.5)

7.3 Results

7.3.1 Differences between above- and below-canopy temperatures

On average, daily maximum temperatures were higher above the canopy than below. Differences in daily maximum temperatures averaged 0.7 °C for air, 0.1 °C for near ground, 1.5 °C for ground, and 4.6 °C for soil temperatures. Conversely, daily minimum temperatures were, on average higher below the canopy, reaching -0.9 °C for air, -0.7 °C for near ground, -2.0 °C for ground, and -4.1 °C for soil temperatures,

on average.

However, temperature differences between LST and T$_{bc}$ highly varied during the year and depending on the height of measurement in the understorey (Fig. 7.2). The highest variability in temperature differences was recorded in the soil, ranging between -15.4 °C and 6.7 °C for daily minimum and -15.3 °C and 23.4 °C for daily maximum temperatures. The difference in other temperature characteristics was lower and reached (according to the descending range) between -9.5 °C and 5.7 °C for daily minimum and -9.3 °C and 12.8 °C for daily maximum ground temperatures; between -7.6 °C and 6.1°C for daily minimum and -10.0 °C and 10.4 °C for daily maximum near ground temperatures; between -7.6 °C and 5.7 °C for daily minimum and -8.6 °C and 10.3 °C for daily maximum air temperatures.
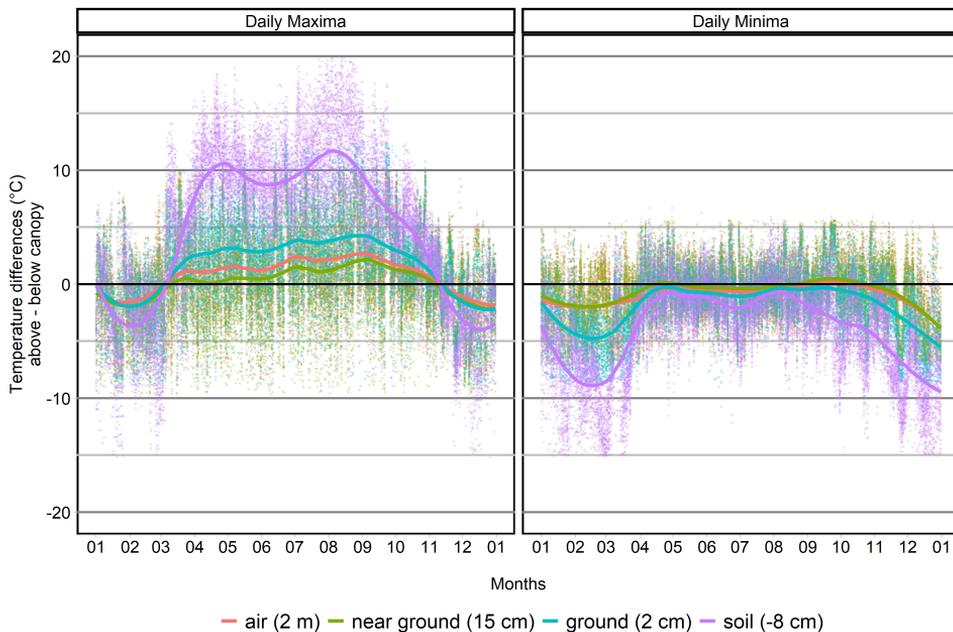
Figure 7.2: Temporal dynamics of temperature differences in daily maxima (left) and in daily minima (right) between above and below canopy in various vertical levels. The lines indicate the rolling 7-day smoothing average.

The temperature differences, when aggregated per month, showed a clear pattern during a year (Fig. 7.3). The effect of the forest canopy on

temperature buffering in the understorey was most pronounced during summer months (from April to September) for maximum temperatures and during winter months (November and February) for minimum temperatures (Fig. 7.3).
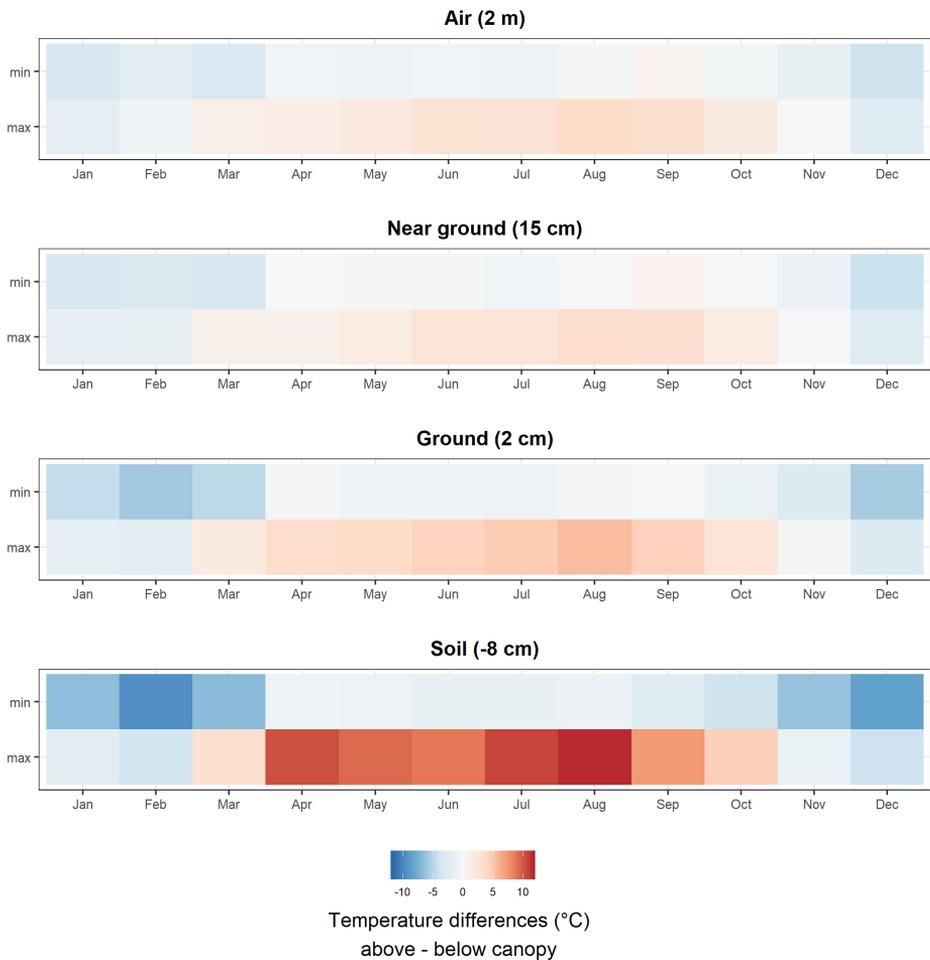
Figure 7.3: A variability in daily minima and maxima temperature differences between above and below canopy (in °C), aggregated to monthly means per position of measurement.

7.3.2 Environmental predictors of temperature differences during seasonal extremes

T_{max} differences between LST and T_{bc} ranged between -2.0 °C and 9.2 °C (mean 3.3 °C) for air temperature; between -2.6 °C and 8.6 °C (mean 2.3 °C) for near ground temperature; between -2.8 °C and 11.7 °C (mean 5.5 °C) for ground temperature; and between 7.3 °C and 21.1 °C (mean 14.4 °C) for near soil temperature.

All models of T_{max} differences performed significantly well with adjusted R^2 between 0.26 and the best score of 0.40 obtained T_{max} differences in soil (Tab. 7.2. The model mostly included two or three topographic variables.

Table 7.2: Microclimate regression model parameters for T_{max} differences. All models have p-values < 0.001.

Variable	Intercept	Elevation	TPI	Radiation	NDVI	Height	Density	Ajd. R^2
Air	6.420	-0.006	0.539	n.s.	n.s.	n.s.	n.s.	0.263
Near ground	2.071	-0.003	n.s.	n.s.	12.099	-0.340	n.s.	0.360
Ground	0.323	-0.007	n.s.	n.s.	10.822	n.s.	n.s.	0.283
Soil	20.261	-0.009	-0.573	-7.510	n.s.	n.s.	n.s.	0.402

The relative importance of predictors differed according to the position of below-canopy measurements (Fig. 7.4). Topographic factors were significant predictors in most of T_{max} difference models. Vegetation factors mostly explained only a small portion of the variance in T_{max} difference models. Their influences were profound in the near ground and ground temperatures (Fig. 7.4). The most important vegetation factors were canopy height and NDVI, whereas canopy density had neglected influence.
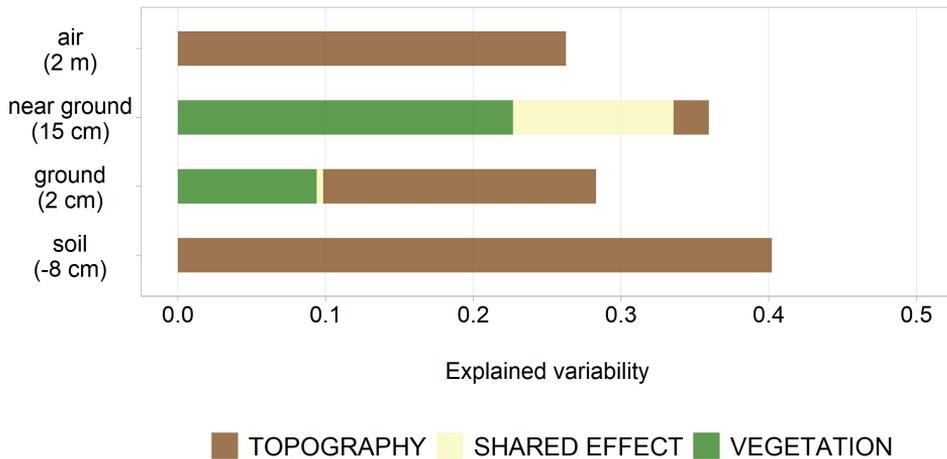
Figure 7.4: Variance in T_{max} differences explained solely by topographical factors, solely by vegetation factors and jointly by both variable groups distinguished according to the position of below-canopy measurements.

7.4   Disccusion

Our findings have demonstrated that temperate forests act as thermal insulators, cooling the understorey during hot ambient temperatures and offering warmth to the understorey during cold periods (De Frenne et al. 2019, Haesen et al. 2021). However, our study has revealed that the temperature differences within the forest environment relative to above-canopy temperature vary significantly depending on the position of the measurement in the vertical understorey gradient (Fig. 7.4). We found that soil temperatures experienced the largest buffering effect, while the smallest effect was seen for air temperature records. This implies that organisms living in the soil experienced lower temperature variability and less severe impacts of the temperature extremes than those residing closer to the forest canopies. Therefore the height of in situ temperature measurement below the forest canopy should be adequately considered when predicting the responses of forest biodiversity and functioning to climate change (Zellweger et al. 2020).

Notably, our study found fundamental differences between soil tem-

peratures and above-canopy temperatures (Fig. 7.2), with substantial buffering against summer heat and winter freeze events (Fig. 7.3). During temperature extremes, this effect was predominantly driven by topographic variables (Fig. 7.4), in accordance with Lembrechts et al. (2022). This buffering effect on soil temperature could affect various soil processes, such as thawing-freezing cycles (Hu et al. 2013), determining soil water availability, and contributing to the dynamics of forest ecosystems (McDowell et al. 2011).

Surprisingly, our study found that vegetation variables were less effective predictors for temperature extremes in the air and in the soil. For near ground and ground T_{max} differences were influenced by NDVI and partly canopy height, but canopy density was less good predictor. This finding was in agreement with Haesen et al. (2021), even though the structure of the forest canopy has been proven to fundamentally affect the forest microclimate (Zellweger et al. 2019a). Small effects of canopy density could be attributed to the indicator used and the processing of data. Canopy density variable originated from passive sensors onboard the Sentinel-2 platform that does not reflect volumetric values but only spectral information that could be biased by clouds and atmospheric aerosols and gases. To enhance its explanatory power, other products based on active remote sensing techniques, such as LiDAR or radar (Frey et al. 2016, Greiser et al. 2018), could be a valuable source of data for further research. Secondly, despite their high spatial resolutions (20 m), it is probably still too coarse (Kašpar et al. 2021). Finally, the lower explained variability by vegetation factors could be due to the linear model used instead of more complex methods that would reveal the non-linear nature of interactions between variables (Zellweger et al. 2019a).

Despite these limitations, our study highlights the potential of using thermal infrared satellite remote sensing data to capture the spatial variability of canopy temperature over large spatial scales and its importance for modelling understorey temperature. Contrary to some

existing studies, which are either sample-based (Zellweger et al. 2019a) or spatially or temporally limited (Kašpar et al. 2021, Davis et al. 2019, Richter et al. 2021), our regional analysis improves on existing knowledge of forest temperature buffering by (i) being spatially explicit (Supp. Fig. 2), (ii) quantifying temperature differences on a diurnal scale and over a long time span, (iii) using only publicly available products, and (iv) being derived through an internally consistent approach that is exempt from the vagaries of different definitions, methods, and data inputs. Especially its potential to be extended globally and further downscaled to finer resolution by other satellite products promises future application in microclimatic analysis or species distribution modelling.

7.5   Conclusion

In this study, we have demonstrated diurnal and seasonal temperature differences between surface canopy derived by thermal remote sensing and in situ below-canopy measurements. Our results showed the ability of the forest to buffer daily temperature extremes, but the effects varied during the seasons depending on the measurement height in the forest undergrowth and the local arrangement of topographic and vegetation factors. The highest variability of temperature differences was recorded in the soil, which maintained relatively stable temperatures throughout the year, while air and ground temperatures more closely followed changes in the canopy surface temperature. Our study, which is based on remote sensing data, offers new possibilities for forest microclimate modelling across broad spatial scales and over long time spans using publicly available satellite products. In particular, our study highlights the potential of using thermal infrared remote sensing data to capture the spatial variability of canopy temperature over large spatial scales and its importance for modelling understorey temperature.

Supplementary materials

Supplementary material associated with this manuscript can be found at https://doi.org/10.6084/m9.figshare.22340602.v1.

Chapter 8

Discussion and Summary

The following part of the dissertation thesis consists of comments on each of the research topics, as well as a summary of the whole dissertation. Since the in-depth discussions and conclusions of the individual studies are detailed in previous parts, this chapter will summarize the findings and discuss how the dissertation's goals were achieved. Some limitations or recommendations that arose from individual articles are discussed further in separate subsections. Finally, future research directions in the field of forest microclimate modelling using indirect methods are also proposed.

Each of the studies focused on a different aspect of the forest environment. The first one (**Study I**) examined several ecologically relevant parameters, including the diversity and abundance of plant species at the forest floor level. **Study II** focused exclusively on temperature characteristics and their extreme manifestations during the growing season. The third study (**Study III**) was, compared to the others, specific – it focused on the urban environment, and the vegetation parameters derived by indirect methods entered physical models for calculating the surface resistance, wind regime, and, ultimately, dry deposition. The last study (**Study IV**) also analyzed temperatures, but this time, it evaluated the vertical profile throughout the understorey measured at different heights.

All studies were rather methodological. They demonstrated the use of indirect, field-based, and RS approaches, their specifics and advan-

tages, and compared their explanatory power and relationships with ground-measured microclimatic variables (**Study II**). **Studies I** and **I** proposed new ways of using these methods in different contexts of modelling the inner microclimatological processes within the forest canopies.

Studies differed in their spatial extent. Their coverage was gradually expanding, starting from site-specific, local relationships (**Study I**) to detailed but already spatially continuous modelling at a small scale (**Study II**, **III**) and, finally, to a regional study using approaches that can be analogically applied globally (**Study IV**). As the spatial extent changed, so did the used methods, from HP and UAS to satellite data. Each method had a different spatial and temporal resolution and other specifics.

Both passive and active, ground-based as well as RS sensors were investigated. HP taken on the ground served as a method of assessing the canopy structure and its relationship to various ecological parameters (**Study I**), for comparison with other RS methods (**Study II**), and for the extrapolation of UAS-derived vegetation indices (Study III). In the case of passive RS sensors, vegetation characteristics were derived from spectral (**Study II**), multispectral (**Study III**), and thermal data (**Study IV**) for the calculation of spectral indices as well as of 3D canopy structures generated using the SfM photogrammetric method. Studies have shown that in certain contexts, individual methods can be comparable (**Study II**) or complementary (**Study III**).

The presented studies explored a relationship between meteorological variables and vegetation properties, with a main focus on macrostructural characteristics (such as canopy height, canopy cover, and canopy openness). On the other hand, micromorphological traits (e.g. stomatal density, leaf size, surface roughness) are mostly neglected in the studies in this field despite their reported importance for stomatal conductance and transpiration in forest canopies, for instance, Drake et al. (2013). Where they are considered, they are mostly only parameterised based

on species composition – this approach was also applied in **Study III**. In the future, the increasing detail of RS-derived data may potentially provide these parameters and become a valuable component of microclimate models.

The interactions between vegetation and microclimate have been investigated in different types of forests, ranging from natural stands with minimal human influence (**Studies I**, **II**) to urban greenery, parks, and other anthropogenic forests (**Study III**). The type and properties of the particular forest environment determined which methods were most suitable for its description. For example, passive RS methods (**Study III**) were more appropriate for scattered and sparser forest stands because the use of these methods for the detection of the forest floor under a closed canopy is complicated (**Study II**).

The microclimate-related vegetation properties and the method chosen for their acquisition brought several other important points to my attention, which will be further discussed in detail in separate chapters. In particular, these include the temporal and spatial fusion of various RS approaches, the comparison of deterministic and mechanistic modelling, the spatial extent of vegetation proxy variables and the positional accuracy of in situ measurements.

8.1 Spatial fusion of remote sensing methods

Most presented studies (**Studies I**, **II**, **III**) dealt with the modelling of spatial-temporal dynamics of microclimate characteristics on a small scale. They proved that UASs may provide microclimate-related information comparable to HP (**Study II**) and can be used for upscaling point-limited ground observations from the HP (**Study I**) to spatially continuous surfaces of vegetation characteristics (**Study III**). However, for higher applicability, for instance in species distribution modelling

or in downscaling regional climate datasets, RS methods with larger spatial coverage that allow the scaling of forest microclimates over large areas will be needed (**Study IV**). Studies on regional (Greiser et al. 2018) or even continental (Haesen et al. 2021, Laskin et al. 2017) scales have recently outlined further progress in this field. Although such studies represent a significant step forward in capturing the forest microclimate, their spatial resolution is probably still too coarse to capture the fine variability in the forest canopy (**Study II**). New RS methods should in the future facilitate the consideration of microclimate spatial heterogeneity (**Studies II**, **III**) while operating at a broader extent.

Although some satellite data (e.g. Maxar, WorldView-3, Planet SkySat) provide stereo images at very high (sub-meter) resolutions, these are mostly commercial satellites, the data of which are unavailable for scaling ground measurements across large extents such as, for example, Europe. A potential compromise between desired detail of mapping and large spatial coverage may lie in multi-source data fusion that reduces the constraints of a single sensor and effectively integrates the advantages of multiplatform complementary observation (Zhu et al. 2018).

Integration of various satellite data with different temporal, spatial, and spectral resolutions (Moosavi et al. 2015, Gao et al. 2006) or fusion with aerial products (Siok et al. 2020) are the most commonly used combinations in data fusion techniques. However, in the context of modelling the forest interior, the fusion of complementary UAS and satellite data could represent a significant breakthrough. Nonetheless, few studies focus specifically on the integration of UAS and satellite data. Moreover, the UAS and satellite data combinations were mostly utilized in precision agriculture and crop monitoring and estimation (Gevaert et al. 2014, Hassan-Esfahani et al. 2017, Jenerowicz and Woroszkiewicz 2016). In forest applications, however, the fusion of UAS and satellite-based data is still lacking.

The second development direction, especially for monitoring forests in outlying areas and modelling internal fluxes of energy and matter exchange globally, is represented by space-borne LiDAR (e.g. GEDI), or SAR (e.g. TanDEM-X) sensors optimized for vegetation mapping. As they may derive vertical canopy structure on a global extent, these data may offer a wide spectrum of vegetation characteristics (e.g. stem density, leaf area density, basal area, or tree height) on a planetary level. However, both techniques have some limitations that constrain their solo use. While SAR backscatter limits retrieving biomass densities above about 100 – 200 Mg/ha, depending on the signal wavelength (Montesano et al. 2013), GEDI data are, on the other hand, obtained discontinuously along transects only, and the resolution of the gridded datasets reflects the across-track distance between these transects (1 km). Therefore, a fusion of space-borne SAR and LiDAR data with other ancillary datasets (Qi et al. 2019) is necessary for producing contiguous global forest canopy maps at finer resolution and with improved accuracy. Already, a fusion of GEDI data with Landsat satellite data (Potapov et al. 2021) highlights the potential of this approach for future developments. Although such datasets produce a contiguous global forest canopy at a 30 m spatial resolution, this is still probably too coarse for capturing all micrometeorological processes. To facilitate the study of these processes, further development of algorithms that appropriately fuse space-borne SAR and LiDAR data with other RS data on forest structural properties in higher spatial resolution will be required (Lang et al. 2022).

8.2 Temporal fusion of remote sensing techniques

The assumption that forests and their characteristics are stable over time is one of the common shortcomings in some previous publications

(Frey et al. 2016) as well as in the presented studies (**Studies I**, **II**).The current common practice is to acquire one dataset, usually at the peak of the growing season (**Studies I**, **II**), for characterizing the canopy parameters and using them to model the microclimate over the entire growing season (**Studies I**, **II**) or even the whole year (Greiser et al. 2018). However, temperate forests experience natural foliage dynamics throughout the year, seasonally affecting the quantity and quality of forest cover. Moreover, a significant part of Europe's forests is systematically managed throughout the year, which makes the need for continuous or at least more frequent collection of vegetation data even more urgent.

For these reasons, it is still rather unknown if and how the buffering capacity of forests varies depending on phenological variation over time. Although **Studies I** and **II** showed that data taken at the peak of the growing season correlate with aggregated thermal variables, they are not sufficient for modelling the microclimate response at, for example, a monthly time step. Similarly, the effects of microclimate on phenology and the importance of temperature buffering in influencing phenological responses to climate change are also poorly explored. In order to understand these mechanisms and model the forest microclimate continuously throughout the season, multitemporal information about the canopy structure is needed.

Time-consuming terrestrial RS methods are rather unsuitable for repeated monitoring (**Study I**), and aerial multispectral or LiDAR imaging is usually carried out only once in several years due to the high acquisition costs. UAS may represent a potential solution for repeated data collection (Ge et al. (2023); **Studies II**, **III**). By acquiring at least two datasets (one in the leaf-on and another in the leaf-off phases of the year), it is possible, for example, to resolve the constraints of the use of the SfM method for generating vegetation characteristics in dense canopies (**Study II**). However, despite UAS democratization, time flexibility, and low acquisition costs, it is still quite unlikely that

the acquisition of images would in practice take place more often. In order to capture seasonal changes in the foliage, UAS-derived data may fuse with satellite data with a higher acquisition frequency.

So far, only relatively few studies focus on temporal fusions of these two types of datasets (Alvarez-Vanhard et al. 2021). They mostly focus on precision agriculture (Liu et al. 2019, Sagan et al. 2019); no study has, however, specifically focused on forestry application. A temporal fusion of UAS and satellite data was carried out in **Study III**, when a gridded LAI map from a single time point was upscaled over the entire growing season. It was based on fitting the UAS data to the latitude-, year- and habitat-modified LAI curve calibrated on the MODIS data and further validated using site-specific Harmonised Landsat and Sentinel 2 (Claverie et al. 2018) NDVI time series. Although such an approach contained considerable simplifications, it might still better reflect vegetation characteristics compared to time-independent (constant) parameters, and due to the relatively simple workflow, this approach might represent a welcome advance for some modelling studies. However, further comparison with already existing algorithms of satellite data fusion (e.g. Gao et al. (2006), Zurita-Milla et al. (2008)) and validation with in situ measurements are necessary.

Looking forward, a multiscale approach based on the fusion of multiple RS platforms (including fine-scale data from UAS) alongside field measurements for the validation or calibration of such data will likely be the most productive approach to microclimate modelling. Incorporation of comprehensive, multi-sensor, and microclimate-informed datasets with high spatial and temporal resolutions into (for instance) species distribution models may reveal more accurate insights into various processes underlying species vulnerability to climate change, including climate change exposure, sensitivity, adaptability, and dispersal (Pacifici et al. 2015).

8.3 Mechanistic or deterministic models

To explore the inner forest microclimate and model it in a spatially explicit manner, two main types of modelling approaches are referred to in the scientific literature: mechanistic and deterministic approaches. The presented study used both modelling methods either based on known physical mechanisms (**Study III**) or on exploring statistical relationships between the canopy structure properties and meteorological variables measured in the forest understorey (**Studies I**, **II**, **IV**).

The use of these approaches is partly defined by scientific disciplines. Many principles of forest microclimate modelling applying basic physical laws of turbulent mixing have a long-standing tradition in fields other than ecology (Monin and Obukhov 1954, Monteith 1965). Ecological studies, however, rather tend to derive microclimatic elements using statistical approaches (Fick and Hijmans 2017, Meineri and Hylander 2017) based either on spatial interpolations of microclimate measurements by loggers installed within a forest (e.g. Ashcroft and Gollan (2013)) or on downscaling macroclimate from free-air weather stations or coarse-grained climate grids (e.g. WorldClim or CHELSA data: Hijmans et al. (2005), Karger et al. (2017)). To do so, a large variety of statistical methods is applied, ranging from simple linear (**Study I**) or multilinear (**Studies II**, **IV**) regression to progressive techniques based on machine learning (Haesen et al. 2021). More advanced methods or artificial intelligence may uncover nonlinear relationships as well as handle multicollinearity among covariates, and thus, maximize model fitting. No matter what statistical approach is used (microclimate interpolation or macroclimate downscaling), accurate high-resolution data of topographic and vegetation predictors (**Studies II**, **III**), computing power, and a dense network of measurements are required.

Most of these limits have been overcome by the development of computing capacity and the availability of variables derived from various RS techniques (**Study II**). Likewise, the recent development of afford-

able and easy-to-use data loggers (Wild et al. 2019) effectively solved the traditional lack of meteorological measurements from the forest environment and enabled, for example, the creation of the global SoilTemp database (Lembrechts et al. 2020). Thanks to these innovations, the deterministic approach revealed explanatory power of various vegetation characteristics derived in different ways (**Studies I**, **II**, **IV**), and opened new opportunities for monitoring of spatial heterogeneity in the forest microclimate (Haesen et al. 2021). Yet, the extrapolation of these statistical relationships into habitats and regions largely not covered by in situ measurements (particularly in Africa and Asia) and projecting them into the future, under changed conditions, is somewhat disputable (Evans 2012).

The other approach used in this work was based on mechanistic modelling (**Study III**). Although it still required inputs from weather stations or climate models, the downscaling process relied on physical principles rather than on the use of interpolation algorithms and spatial statistics. Therefore, mechanistic modelling of the microclimate enabled, in contrast to the deterministic approach, a more reliable spatial extrapolation (**Study III**) and prediction of future scenarios upon changed macroclimatic variables (Maclean 2020).

Classic works on microclimate models mostly investigated the physical processes using ground-measured variables (Campbell 1986). However, when including currently available data from a regional climate reanalysis (ERA5-Land, Muñoz Sabater et al. (2019)) or future climate simulations (ENSEMBLES, Hewitt (2004)) as driving parameters, we can achieve improvements in the model extent. Similarly, RS data can represent a welcome enhancement in the spatial and temporal detail involving vegetation phenology and canopy heterogeneity (**Study III**). As demonstrated here, high-quality data on vegetation characteristics can be involved in the calculation of surface resistance, stomatal conductance and surface roughness (**Study III**), determining wind flow, evapotranspiration and gas fluxes within canopies (Emberson et al.

2000, 2001). However, a number of other microclimatic parameters derived from RS, such as shortwave radiation reflected by canopies (Levy et al. 2018) can be used as well. The incorporation of such characteristics with ever-expanding spatial and temporal resolution may potentially lead to improving model accuracy and more realistic results (Duffy et al. 2021).

Recently, mechanistic modelling of microclimate in ecology draws growing attention, augmented by the development of several R packages. For instance, the widely used microclimate model by Porter et al. (1973) was translated into the R package *NicheMapR* (Kearney and Porter 2020). Similarly, based on the model of Bennie et al. (2008), Maclean et al. (2019) released the R package *microclima*, designed for modelling gridded open-air microclimate estimates. From the perspective of the forest environment, major progress is represented by the package *microclimc* (Maclean and Klinges 2021), which is capable to quantify a within-canopy wind regime and transport of the heat and water vapour. By default, the model works with vegetation parameters derived from literature typical for the given habitat. Since the model enables simple user-specified parameterization, it could be improved by including additional RS-derived characteristics (similarly to **Study III**). Testing the model sensitivity to chosen RS vegetation variables, to their spatial details and the frequency of their acquisition could constitute another interesting research direction.

8.4 Spatial extent used to derive forest canopy characteristics in microclimate modelling

Although many studies confirm the role of canopy structure in influencing the microclimate in the forest understories (Jucker et al. 2018, Macek

et al. 2019), the question remains at what spatial extent vegetation properties are relevant to the microclimate. The scale of the spatial buffer for vegetation variables derived from RS that best explain the microclimate in a given point is, therefore, another unexplored field of research (**Studies I**, **II**).

Solving this riddle is especially crucial with the increasingly high and ultra-high spatial resolution of RS sensors (**Studies II**, **III**), which provide pixel size often with higher detail than the likely spatial extent at which forest microclimate operates (Frey et al. 2016). Some studies have already discussed this issue, investigating various constantly increasing large buffer sizes (Smith-Tripp et al. 2022, Atkins et al. 2020). They found that canopy height averaged within a radius of 15 to 20 m around microclimatic loggers performed best in explaining near-ground and soil temperatures (Smith-Tripp et al. 2022). However, as suggested by Bode et al. (2014), the size of the surroundings, which determines the radiation reaching the forest floor and ultimately thermal conditions in any given place can't be arbitrarily defined. The reason lies in the fact that it depends on various dynamic parameters, including the interaction of the ever-changing sun position and site-specific canopy height obstructing sunlight.

Accordingly, a similar approach was applied in **Study II** showing that canopy height best explained the variability of the microclimate response when derived within an area corresponding to 32 – 62 meters of buffer radii (see Supplementary at https://doi.org/10.1016/j.rse.2021.112522). In contrast, the canopy cover predictor explained the highest variability of air and soil temperature offsets when averaged at the buffer radii of 10 – 19 meters. This implies that various forest canopy predictors may have different effects when derived at different buffer radii and, thus, their scale extents used in microclimate modelling may vary.

Moreover, **Study I** demonstrated that the spatial extent probably depends also on the microclimate variable considered. When canopy openness was calculated across a larger angle of view (AOV) of HP, mod-

els explained the variability in mean soil and maximum air temperatures better than the variability in PAR. PAR estimation, on the other hand, was most successful when canopy openness was evaluated in a smaller area (i.e., with a smaller angle, in our case 80° AOV); for the thermal characteristics, however, it is better to evaluate the canopy openness in larger surroundings (100° – 120° AOV). Similarly, Smith-Tripp et al. (2022) documented that canopy structure measured across smaller scales (5 meters) better explained soil moisture. This is likely because microclimatic variables are controlled by different driving processes, which, in addition, operate at different spatial extents and are, therefore, influenced by vegetation at different distances. For instance, while near-ground air temperatures are governed by total incoming solar radiation, PAR on the forest floor is mostly controlled by radiation directly incident above that point (Canham et al. 1994).

The fact that an even larger spatial extent is sufficient for the determination of certain microclimatic variables may favour the usage of datasets with coarser spatial resolution, e.g. from Landsat or Sentinel satellites, for their modelling (Zellweger et al. 2019a, Haesen et al. 2021). However, it is necessary to keep in mind that aggregated canopy structure data originating from finer spatial resolution may result in different spatial patterns based on the aggregation method, such as the averaging, central-pixel resampling etc. (Bian and Butler 1999, Moudrý et al. 2023b). Therefore, coarse satellite and aggregated UAS-based data on vegetation characteristics are not interchangeable.

8.5   GNSS positioning under forest canopies

It is well known that the precision and accuracy of GNSS positioning is reduced under forest canopies (Hasegawa and Yoshimura 2003, Yoshimura and Hasegawa 2003, Naesset and Jonmeister 2002) as vegetation obstacles tend to degrade the satellite signal reaching the GNSS

receiver on the ground. In conditions of sparse canopies with large gaps or openings (**Study III**), differential GNSS with RTK corrections may be sufficient to achieve sub-meter precision in obtained coordinates (Naesset and Jonmeister 2002). However, under closed canopies (**Studies I**, **II**), the positioning error increases and, depending on the used GNSS technology, atmospheric conditions, number of satellites, positioning time and canopy density may exceed ten meters (Feng et al. 2021). To mitigate the problem of combining spatially detailed vegetation characteristics from UAS with inaccurate positioning of ground measurements, several types and settings of GNSS instruments were tested in the pre-processing phase of **Study II**. The large disparities of geographical coordinates obtained using different GNSS approaches finally led to a time-consuming but accurate re-measurement using differential GNSS in an adjacent treeless area and a survey of all locations using a total station. Comparison of the total station measurements to those from several GNSS receivers revealed a wide range of spatial inaccuracies in all GNSS methods under the canopy, with none having at least sub-meter maximal accuracy (Fig. 8.1).

The accuracy requirements will always mirror the purpose and aims of a particular research. When modelling forest microclimate using spatially coarse data from satellite products, the issue of ground sensor location can be neglected (Laskin et al. 2017, Lembrechts et al. 2022). However, with the ever-increasing high spatial resolution of aerial or UAS-derived data, laborious measurement by a total station, as suggested in **Study II**, seems necessary for adequate positioning. When using other GNSS technologies, the spatial discrepancy between the below-canopy meteorological sensors and RS data may arise despite the corrections used, long-term positioning, and spatial accuracy referred to by the GNSS equipment manufacturer (usually related to unobstructed conditions). However, this fact tends to be overlooked in many studies investigating the forest microclimate and its determination by RS data, which could lead to analyses of imprecisely positioned ob-
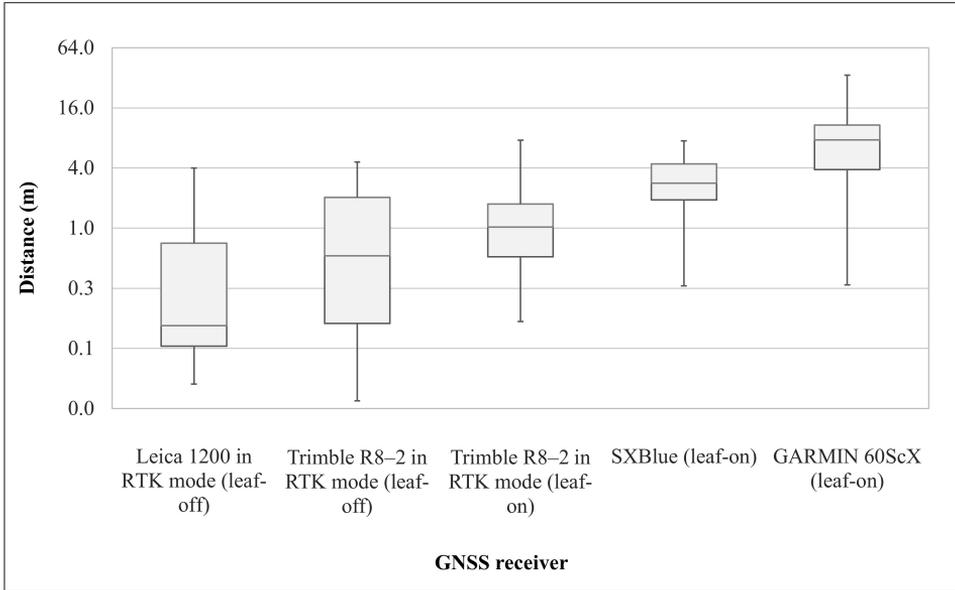
*Figure 8.1: Distances (m) between 23 TMS data loggers used in **Study II** georeferenced using a total station TS Trimble 5503DRS and using several GNSS receivers – note the wide range of horizontal positioning accuracy upon various foliage conditions..*

servations with spatially detailed data (Marsh et al. 2022, Smith-Tripp et al. 2022).

Similarly, accurate GNSS positioning is also required for ground control points (GCP) used to geo-reference RS data both horizontally and vertically. Although the GCP targets are usually placed so that they are visible from the sky, i.e., not directly under the forest canopy, such conditions are difficult to ensure in extensive forest stands, where only occasional canopy gaps or small openings can be used (Bagaram et al. (2018), partially **Study II**). Even there, the surrounding trees can still cause reflections of the received signal and therefore, positional inconsistency in the generated data. Again, the degradation of GNSS signal in forest landscapes often requires the use of total station measurements, regardless of the number of GCPs used (Tomaštík et al. 2017). Complex conditions for high-quality GNSS signal reception under forest canopies can ultimately affect the spatial accuracy of both

ground-based measurements and remotely derived predictors.

8.6 Further Research

In addition to some of the above-described recommendations and prospects for future research, especially in the field of RS, I should also briefly mention some gaps in the forest microclimate research that may possibly be filled by further investigation.

Most RS studies focused on technical aspects, such as data processing, with lower attention to answering ecological questions (Sun et al. 2021). New opportunities will bring about closer cooperation between ecologists, climatologists, and RS experts, for example, to define which ecologically meaningful parameters should be derived and extracted from RS data and how these should be processed in a standard way to enable easy comparison between case studies.

Furthermore, some limitations have arisen in forest microclimate monitoring. Despite the recent development of accessible temperature data loggers (Wild et al. 2019), there are not enough small-scale, self-contained moisture, wind speed, or radiation sensors available to be left in situ alongside temperature data loggers. As a result of this, these important factors are understudied. So far, the focus was on thermal microclimates; for many species and in many ecosystems, however, hydro- and hygro- microclimates might be more relevant (Kopeckỳ et al. 2021). Similarly, the evapotranspiration component in the forest environment plays a substantial role in water balance. Increasing our efforts in measuring and modelling water- and humidity-driven variations in microclimates will offer new opportunities in terrestrial ecological and hydrological research.

Additionally, observing meteorological variables along the vertical profiles below and above forest canopies (see Lenoir et al. (2017)) would be also beneficial. Alternatively, direct measurements from UAS-borne

meteorological sensors would satisfy this demand Cassano (2014), particularly in topographically challenging and inaccessible environments. In such cases, however, high-speed Internet connection will be needed for georeferencing and communicating with the UAS during flight. Similarly, an increasing number of apps and smartphone sensors (such as a thermal camera or a fisheye lens attachment) could substitute standard measurements (**Study I**) and further democratize microclimate monitoring.

The collection of meteorological data should also extend spatially to regions such as Africa or Asia. The current coverage by low-cost data loggers is very spatially uneven, with loggers distributed mostly within Europe (although locally, they can be found in remote locations as well) (Lembrechts et al. 2020). The biggest and, at the same time, the most important challenge for forest microclimate monitoring and modelling lies in studying distant and unexplored areas of tropical rainforests. Limited research has already taken place in these areas (Asner et al. 2015), but more attention should be directed there in the future. The approaches tested in the more explored conditions of temperate forests (**Studies I**, **II**, **III**, **IV**) can thus serve as a supporting basis for future studies in places constituting a substantial source of world biodiversity and key sinks of terrestrial carbon.

Besides, the vast majority of current studies use only short time series and evaluate the buffering effect of the canopy under standard meteorological conditions (Ashcroft and Gollan 2013, Frey et al. 2016, Kovács et al. 2020, Suggitt et al. 2011). Nevertheless, long-term datasets are crucial for capturing microclimate responses during extreme but infrequent events (such as heat waves).

In view of this development, the strengthening of cooperation between scientific disciplines is likely to bring mutual benefits and represents an important route to progress in microclimate research. In summary, the future of forest microclimate research may lie in the use of state-of-the-art technologies to obtain standardized and freely available data

for use in large collaborative studies and the development of additional microclimate models.

8.7 Conclusion

This work provides new insight into forest microclimate and its modelling using data on forest canopy architectures derived from indirect, field-based, and RS techniques. It examines and demonstrates methodologies for how these approaches and scale-relevant data on vegetation characteristics of various temperate forests derived using these methods can be used for exploring internal climatic conditions. From the results of the thesis, the following general conclusions can be drawn:

- Due to their hiddenness from direct observation and the complexity of biophysical interactions, forests represent a unique and complicated environment that significantly modifies local microclimatic conditions. The presented thesis explored the associations between structural properties of the canopy and seasonal as well as daily temperature variations in the forest understorey. Indirectly derived variables, such as canopy cover/closure and height, may well reflect the microclimatic conditions and thus bring much-needed insight into the forest interior.

- HP acquired by a camera with a circular fisheye lens facing upwards provides point-based ecologically and climatologically relevant information about the canopy structure. According to the findings of this thesis, canopy parameters determined from narrower zenith angles may be sufficient to explain thermal and radiation regimes in the forest understorey. This broadens the spectra of cameras and lenses potentially suitable for estimating canopy openness and, thus, further democratizes and standardizes canopy structure calculations in forest ecology and meteorology.

- RS, on the other hand, offers an exciting opportunity to quantify canopy structure and heterogeneity over large spatial and temporal scales and to provide spatially continuous data. Vegetation parameters derived in this way can be used either as predictors for exploring relationships with microclimate variables or as parameters to mechanistic models, crucial for upscaling point-based measurements of microclimatic sensors or downscaling macroclimate datasets into scales appropriate to species that reside there.

- UAS-derived data represent a bridge between satellite platforms and ground-based measurements for studying fine-scale processes governing climate near the ground. Results showed that a UAS-mounted high-resolution RGB camera combined with the SfM algorithm can constitute an efficient low-cost alternative to the LiDAR technique and to hemispherical photographs, providing spatial and volumetric data incorporating local-scale and seasonal variability of canopy structure into forest microclimate modelling.

- Although data inferred from established satellite products are often limited in their spatial resolution, they can provide important insight into the temporal dynamics and spatial heterogeneity of forest canopies allowing microclimate mapping over large areas. Mapping landscape-level microclimate heterogeneity improves our ability to study how organisms respond to climate variation, which has important implications for understanding climate-change impacts on biodiversity and ecosystems.

Chapter 9

References

Abdollahnejad, A., Panagiotidis, D., Surový, P., and Ulbrichová, I. (2018). UAV capability to detect and interpret solar radiation as a potential replacement method to hemispherical photography. *Remote Sensing*, 10(3):423–440.

Abhijith, K., Kumar, P., Gallagher, J., McNabola, A., Baldauf, R., Pilla, F., Broderick, B., Di Sabatino, S., and Pulvirenti, B. (2017). Air pollution abatement performances of green infrastructure in open road and built-up street canyon environments–a review. *Atmospheric Environment*, 162:71–86.

Alexander, C., Moeslund, J. E., Bøcher, P. K., Arge, L., and Svenning, J.-C. (2013). Airborne laser scanner (LiDAR) proxies for understory light conditions. *Remote Sensing of Environment*, 134:152–161.

Alibakhshi, S., Naimi, B., Hovi, A., Crowther, T. W., and Rautiainen, M. (2020). Quantitative analysis of the links between forest structure and land surface albedo on a global scale. *Remote Sensing of Environment*, 246:111854.

Alonso, R., Vivanco, M. G., González-Fernández, I., Bermejo, V., Palomino, I., Garrido, J. L., Elvira, S., Salvador, P., and Artíñano, B. (2011). Modelling the influence of peri-urban trees in the air quality of Madrid region (Spain). *Environmental Pollution*, 159(8-9):2138–2147.

Alvarez-Vanhard, E., Corpetti, T., and Houet, T. (2021). UAV & satellite synergies for optical remote sensing applications: A literature review. *Science of Remote Sensing*, 3:100019.

Anderson, M. (1971). Radiation and crop structure. In Sestak, Z., Catsky, J., and Jarvis, P., editors, *Plant Photosynthetic Production: Manual of Methods*, pages 412–456. Dr. W. Junk N.V., The Hague.

Anderson, M. C. (1966). Stand structure and light penetration. II. A theoretical analysis. *The Journal of Applied Ecology*, 3(1):41.

Arietta, A. Z. A. (2022). Estimation of forest canopy structure and understory light using spherical panorama images from smartphone photography. *Forestry*, 95(1):38–48.

Ash, J. D., Givnish, T. J., and Waller, D. M. (2017). Tracking lags in historical plant species' shifts in relation to regional climate change. *Global Change Biology*, 23(3):1305–1315.

Ashcroft, M. B. and Gollan, J. R. (2013). The sensitivity of topoclimatic models to fine-scale microclimatic variability and the relevance for ecological studies. *Theoretical and Applied Climatology*, 114(1-2):281–289.

Asner, G. P., Martin, R. E., Anderson, C. B., and Knapp, D. E. (2015). Quantifying forest canopy traits: Imaging spectroscopy versus field survey. *Remote Sensing of Environment*, 158:15–27.

Asner, G. P., Palace, M., Keller, M., Pereira Jr, R., Silva, J. N., and Zweede, J. C. (2002). Estimating canopy structure in an amazon forest from laser range finder and ikonos satellite observations 1. *Biotropica*, 34(4):483–492.

Atkins, J. W., Stovall, A. E., and Yang, X. (2020). Mapping temperate forest phenology using tower, uav, and ground-based sensors. *Drones*, 4(3):56.

Aussenac, G. (2000). Interactions between forest stands and microclimate: ecophysiological aspects and consequences for silviculture. *Annals of Forest Science*, 57:287–301.

Bagaram, M. B., Giuliarelli, D., Chirici, G., Giannetti, F., and Barbati, A. (2018). Uav remote sensing for biodiversity monitoring: are forest canopy gaps good covariates? *Remote Sensing*, 10(9):1397.

Baldocchi, D. D., Hicks, B. B., and Camara, P. (1987). A canopy stomatal resistance model for gaseous deposition to vegetated surfaces. *Atmospheric Environment (1967)*, 21(1):91–101.

Baró, F., Haase, D., Gómez-Baggethun, E., and Frantzeskaki, N. (2015). Mismatches between ecosystem services supply and demand in urban areas: A quantitative assessment in five European cities. *Ecological Indicators*, 55:146–158.

Barry, R. G. and Blanken, P. D. (2016). *Microclimate and local climate*. Cambridge University Press.

Barwise, Y. and Kumar, P. (2020). Designing vegetation barriers for urban air pollution abatement: a practical review for appropriate plant species selection. *npj Climate and Atmospheric Science*, 3(1):1–19.

Beckett, K. P., Freer-Smith, P., and Taylor, G. (1998). Urban woodlands: their role in reducing the effects of particulate pollution. *Environmental Pollution*, 99(3):347–360.

Bennie, J., Huntley, B., Wiltshire, A., Hill, M. O., and Baxter, R. (2008). Slope, aspect and climate: Spatially explicit and implicit models of topographic microclimate in chalk grassland. *Ecological Modelling*, 216(1):47–59.

Bertrand, R., Lenoir, J., Piedallu, C., Dillon, G. R., De Ruffray, P., Vidal, C., Pierrat, J. C., and Gégout, J. C. (2011). Changes in plant community composition lag behind climate warming in lowland forests. *Nature*, 479(7374):517–520.

Bian, L. and Butler, R. (1999). Comparing effects of aggregation methods on statistical and spatial properties of simulated spatial data. *Photogrammetric Engineering and Remote Sensing*, 65(1):73–84.

Bianchi, S., Cahalan, C., Hale, S., and Gibbons, J. M. (2017). Rapid assessment of forest canopy and light regime using smartphone hemispherical photography. *Ecology and Evolution*, 7(24):10556–10566.

Bílek, J., Bílek, O., Maršolek, P., and Buček, P. (2021). Ambient air quality measurement with low-cost optical and electrochemical sensors: An evaluation of continuous year-long operation. *Environments*, 8(11):114.

Bjørnstad, O. (2019). ncf: Spatial covariance functions version 1.2–8.

Bode, C. A., Limm, M. P., Power, M. E., and Finlay, J. C. (2014). Subcanopy Solar Radiation Model: predicting solar radiation across a heavily vegetated landscape using LiDAR and GIS solar radiation models. *Remote Sensing of Environment*, 154:387–397.

Böhner, J. and Antonić, O. (2009). Land-surface parameters specific to topoclimatology. *Developments in Soil Science*, 33:195–226.

Bonan, G. B. (2008). Forests and climate change: Forcings, feedbacks, and the climate benefits of forests. *Science*, 320(5882):1444–1449.

Bottalico, F., Travaglini, D., Chirici, G., Garfi, V., Giannetti, F., De Marco, A., Fares, S., Marchetti, M., Nocentini, S., Paoletti, E., Salbitano, F., and Sanesi, G. (2017). A spatially-explicit method to assess the dry deposition of air pollution by urban forests in the city of Florence, Italy. *Urban Forestry & Urban Greening*, 27:221–234.

Bramer, I., Anderson, B. J., Bennie, J., Bladon, A. J., De Frenne, P., Hemming, D., Hill, R. A., Kearney, M. R., Körner, C., Korstjens, A. H., Lenoir, J., Maclean, I. M., Marsh, C. D., Morecroft, M. D., Ohlemüller, R., Slater, H. D., Suggitt, A. J., Zellweger, F., and Gillingham, P. K. (2018). Advances in Monitoring and Modelling Climate at Ecologically Relevant Scales. *Advances in Ecological Research*, 58:101–161.

Bréda, N. J. (2003). Ground-based measurements of leaf area index: A review of methods, instruments and current controversies. *Journal of Experimental Botany*, 54(392):2403–2417.

Brewer, K., Clulow, A., Sibanda, M., Gokool, S., Odindi, J., Mutanga, O., Naiken, V., Chimonyo, V. G., and Mabhaudhi, T. (2022). Estimation of maize foliar temperature and stomatal conductance as indicators of water stress based on optical and thermal imagery acquired using an Unmanned Aerial Vehicle (UAV) platform. *Drones*, 6(7).

Britter, R. E. and Hanna, S. R. (2003). Flow and dispersion in urban areas. *Annual review of fluid mechanics*, 35(1):469–496.

Broadbent, E. N., Zambrano, A. M. A., Asner, G. P., Field, C. B., Rosenheim, B. E., Kennedy-Bowdoin, T., Knapp, D. E., Burke, D., Giardina, C., and Cordell, S. (2014). Linking rainforest ecophysiology and microclimate through fusion of airborne LiDAR and hyperspectral imagery. *Ecosphere*, 5(5):1–37.

Campbell, G. S. (1986). Extinction coefficients for radiation in plant canopies calculated using an ellipsoidal inclination angle distribution. *Agricultural and Forest Meteorology*, 36(4):317–321.

Canham, C. D., Denslow, J. S., Platt, W. J., Runkle, J. R., Spies, T. A., and White, P. S. (1990). Light regimes beneath closed canopies and tree-fall gaps in temperate and tropical forests. *Canadian Journal of Forest Research*, 20(5):620–631.

Canham, C. D., Finzi, A. C., Pacala, S. W., and Burbank, D. H. (1994). Causes and consequences of resource heterogeneity in forests: interspecific variation

in light transmission by canopy trees. *Canadian Journal of Forest Research*, 24(2):337–349.

Cao, C., Lee, X., Muhlhausen, J., Bonneau, L., and Xu, J. (2018). Measuring landscape albedo using unmanned aerial vehicles. *Remote Sensing*, 10(11).

Carlson, T. N. and Ripley, D. A. (1997). On the relation between NDVI, fractional vegetation cover, and leaf area index. *Remote Sensing of Environment*, 62(3):241–252.

Cassano, J. J. (2014). Observations of atmospheric boundary layer temperature profiles with a small unmanned aerial vehicle. *Antarctic Science*, 26(2):205–213.

Chacón, P. and Armesto, J. J. (2005). Effect of canopy openness on growth, specific leaf area, and survival of tree seedlings in a temperate rainforest of Chiloé Island, Chile. *New Zealand Journal of Botany*, 43(1):71–81.

Chapman, L. (2007). Potential applications of near infra-red hemispherical imagery in forest environments. *Agricultural and Forest Meteorology*, 143(1-2):151–156.

Chazdon, R. L. and Pearcy, R. W. (1991). The importance of sunflecks for forest understory plants. *BioScience*, 41(11):760–766.

Chen, H., Cloude, S. R., and Goodenough, D. G. (2016). Forest canopy height estimation using Tandem-X coherence data. *IEEE Journal of Selected Topics in Applied Earth Observations and Remote Sensing*, 9(7):3177–3188.

Chen, J., Blanken, P., Black, T., Guilbeault, M., and Chen, S. (1997). Radiation regime and canopy architecture in a boreal aspen forest. *Agricultural and Forest Meteorology*, 86(1-2):107–125.

Chen, J., Franklin, J. F., and Spies, T. A. (1993). Contrasting microclimates among clearcut, edge, and interior of old-growth douglas-fir forest. *Agricultural and forest meteorology*, 63(3-4):219–237.

Chen, J., Saunders, S. C., Crow, T. R., Naiman, R. J., Brosofske, K. D., Mroz, G. D., Brookshire, B. L., and Franklin, J. F. (1999). Microclimate in forest ecosystem and landscape ecology: variations in local climate can be used to monitor and compare the effects of different management regimes. *BioScience*, 49(4):288–297.

Chen, J. M. and Black, T. (1992). Defining leaf area index for non-flat leaves. *Plant, Cell & Environment*, 15(4):421–429.

Cheung, P. K., Jim, C. Y., and Hung, P. L. (2021). Preliminary study on the temperature relationship at remotely-sensed tree canopy and below-canopy air and ground surface. *Building and Environment*, 204:108169.

Chianucci, F. (2015). A note on estimating canopy cover from digital cover and hemispherical photography. *Silva Fennica*, 50(1).

Chianucci, F. (2020). An overview of in situ digital canopy photography in forestry. *Canadian Journal of Forest Research*, 50(3):227–242.

Chianucci, F. and Cutini, A. (2012). Digital hemispherical photography for estimating forest canopy properties: Current controversies and opportunities. *iForest - Biogeosciences and Forestry*, 5(6):290–295.

Chianucci, F. and Cutini, A. (2013). Estimation of canopy properties in deciduous forests with digital hemispherical and cover photography. *Agricultural and Forest Meteorology*, 168:130–139.

Chianucci, F., Disperati, L., Guzzi, D., Bianchini, D., Nardino, V., Lastri, C., Rindinella, A., and Corona, P. (2016). Estimation of canopy attributes in beech forests using true colour digital images from a small fixed-wing uav. *International journal of applied earth observation and geoinformation*, 47:60–68.

Chianucci, F. and Macek, M. (2022). hemispher: an r package for fisheye canopy image analysis. *bioRxiv*, pages 2022–04.

Claverie, M., Ju, J., Masek, J. G., Dungan, J. L., Vermote, E. F., Roger, J.-C., Skakun, S. V., and Justice, C. (2018). The Harmonized Landsat and Sentinel-2 surface reflectance data set. *Remote Sensing of Environment*, 219:145–161.

Conrad, O., Bechtel, B., Bock, M., Dietrich, H., Fischer, E., Gerlitz, L., Wehberg, J., Wichmann, V., and Böhner, J. (2015). System for automated geoscientific analyses (SAGA) v. 2.1. 4. *Geoscientific Model Development*, 8(7):1991–2007.

Cook, J. G., Stutzman, T. W., Bowers, C. W., Brenner, K. A., and Irwin, L. I. (1995). Spherical densiometers produce biased estimates of forest canopy cover. *Wildlife Society Bulletin*, 23(4):711–717.

Curtis, J. A., Flint, L. E., Flint, A. L., Lundquist, J. D., Hudgens, B., Boydston, E. E., and Young, J. K. (2014). Incorporating cold-air pooling into downscaled climate models increases potential refugia for snow-dependent species within the Sierra Nevada Ecoregion, CA. *PLoS ONE*, 9(9).

Dandois, J. P. and Ellis, E. C. (2010). Remote sensing of vegetation structure using computer vision. *Remote sensing*, 2(4):1157–1176.

Dandois, J. P., Olano, M., and Ellis, E. C. (2015). Optimal altitude, overlap, and weather conditions for computer vision UAV estimates of forest structure. *Remote Sensing*, 7(10):13895–13920.

Davidson, A. and Wang, S. (2004). The effects of sampling resolution on the surface albedos of dominant land cover types in the North American boreal region. *Remote Sensing of Environment*, 93(1-2):211–224.

Davies-Colley, R. J., Payne, G., and Van Elswijk, M. (2000). Microclimate gradients across a forest edge. *New Zealand Journal of Ecology*, pages 111–121.

Davis, K. T., Dobrowski, S. Z., Holden, Z. A., Higuera, P. E., and Abatzoglou, J. T. (2019). Microclimatic buffering in forests of the future: the role of local water balance. *Ecography*, 42(1):1–11.

De Frenne, P., Lenoir, J., Luoto, M., Scheffers, B. R., Zellweger, F., Aalto, J., Ashcroft, M. B., Christiansen, D. M., Decocq, G., De Pauw, K., et al. (2021). Forest microclimates and climate change: Importance, drivers and future research agenda. *Global Change Biology*, 27(11):2279–2297.

De Frenne, P., Zellweger, F., Rodríguez-Sánchez, F., Scheffers, B. R., Hylander, K., Luoto, M., Vellend, M., Verheyen, K., and Lenoir, J. (2019). Global buffering of temperatures under forest canopies. *Nature Ecology & Evolution*, 3(5):744–749.

Díaz, G. M., Mohr-Bell, D., Garrett, M., Muñoz, L., and Lencinas, J. D. (2020). Customizing unmanned aircraft systems to reduce forest inventory costs: can oblique images substantially improve the 3D reconstruction of the canopy? *International Journal of Remote Sensing*, 41(9):3480–3510.

Dickinson, R. E. (1983). Land surface processes and climate—surface albedos and energy balance. *Advances in Geophysics*, 25(C):305–353.

Döpper, V., Gränzig, T., Kleinschmit, B., and Förster, M. (2020). Challenges in UAS-based TIR imagery processing: Image alignment and uncertainty quantification. *Remote Sensing*, 12(10):1–22.

Drake, P. L., Froend, R. H., and Franks, P. J. (2013). Smaller, faster stomata: scaling of stomatal size, rate of response, and stomatal conductance. *Journal of Experimental Botany*, 64(2):495–505.

Dubayah, R., Armston, J., Healey, S. P., Bruening, J. M., Patterson, P. L., Kellner, J. R., Duncanson, L., Saarela, S., Ståhl, G., Yang, Z., Tang, H., Blair, J. B., Fatoyinbo, L., Goetz, S., Hancock, S., Hansen, M., Hofton, M., Hurtt, G., and Luthcke, S. (2022). GEDI launches a new era of biomass inference from space. *Environmental Research Letters*, 17(9).

Duffy, J. P., Anderson, K., Fawcett, D., Curtis, R. J., and Maclean, I. M. (2021). Drones provide spatial and volumetric data to deliver new insights into microclimate modelling. *Landscape Ecology*, 36(3):685–702.

Duncanson, L., Kellner, J. R., Armston, J., Dubayah, R., Minor, D. M., Hancock, S., Healey, S. P., Patterson, P. L., Saarela, S., Marselis, S., et al. (2022). Aboveground biomass density models for NASA's Global Ecosystem Dynamics Investigation (GEDI) lidar mission. *Remote Sensing of Environment*, 270:112845.

Eisenman, T. S., Flanders, T., Harper, R. W., Hauer, R. J., and Lieberknecht, K. (2021). Traits of a bloom: a nationwide survey of US urban tree planting initiatives (TPIs). *Urban Forestry & Urban Greening*, 61:127006.

Emberson, L., Ashmore, M., Cambridge, H., Simpson, D., and Tuovinen, J.-P. (2000). Modelling stomatal ozone flux across europe. *Environmental Pollution*, 109(3):403–413.

Emberson, L., Ashmore, M., Simpson, D., Tuovinen, J.-P., and Cambridge, H. (2001). Modelling and mapping ozone deposition in Europe. *Water, Air, and Soil Pollution*, 130:577–582.

Erell, E., Leal, V., and Maldonado, E. (2005). Measurement of air temperature in the presence of a large radiant flux: An assessment of passively ventilated thermometer screens. *Boundary-Layer Meteorology*, 114(1):205–231.

Erisman, J. W., Van Pul, A., and Wyers, P. (1994). Parametrization of surface resistance for the quantification of atmospheric deposition of acidifying pollutants and ozone. *Atmospheric Environment*, 28(16):2595–2607.

Evans, D. L., Roberts, S. D., and Parker, R. C. (2006). Lidar a new tool for forest measurements? *The Forestry Chronicle*, 82(2):211–218.

Evans, M. R. (2012). Modelling ecological systems in a changing world. *Philosophical Transactions of the Royal Society B: Biological Sciences*, 367(1586):181–190.

Faye, E., Rebaudo, F., Yánez-Cajo, D., Cauvy-Fraunié, S., and Dangles, O. (2016). A toolbox for studying thermal heterogeneity across spatial scales: from unmanned aerial vehicle imagery to landscape metrics. *Methods in Ecology and Evolution*, 7(4):437–446.

Feng, T., Chen, S., Feng, Z., Shen, C., and Tian, Y. (2021). Effects of canopy and multi-epoch observations on single-point positioning errors of a GNSS in coniferous and broadleaved forests. *Remote Sensing*, 13(12).

Fick, S. E. and Hijmans, R. J. (2017). WorldClim 2: new 1-km spatial resolution climate surfaces for global land areas. *International Journal of Climatology*, 37(12):4302–4315.

Fieberg, J. R., Vitense, K., and Johnson, D. H. (2020). Resampling-based methods for biologists. *PeerJ*, 2020(3).

Foody, G. M. (2003). Remote sensing of tropical forest environments: towards the monitoring of environmental resources for sustainable development. *International Journal of Remote Sensing*, 24(20):4035–4046.

Ford, K. R., Ettinger, A. K., Lundquist, J. D., Raleigh, M. S., and Hille Ris Lambers, J. (2013). Spatial heterogeneity in ecologically important climate variables at coarse and fine scales in a high-snow mountain landscape. *PLoS ONE*, 8(6):e65008.

Fournier, R. A. and Hall, R. J. (2017). *Hemispherical photography in forest science: Theory, methods, applications.* Springer.

Franch, B., Vermote, E., Skakun, S., Roger, J. C., Santamaria-Artigas, A., Villaescusa-Nadal, J. L., and Masek, J. (2018). Toward Landsat and Sentinel-2 BRDF normalization and albedo estimation: A case study in the Peruvian Amazon forest. *Frontiers in Earth Science*, 6:1–5.

Franklin, J., Davis, F. W., Ikegami, M., Syphard, A. D., Flint, L. E., Flint, A. L., and Hannah, L. (2013). Modeling plant species distributions under future climates: how fine scale do climate projections need to be? *Global change biology*, 19(2):473–483.

Frazer, G. W., Fournier, R. A., Trofymow, J. A., and Hall, R. J. (2001). A comparison of digital and film fisheye photography for analysis of forest canopy structure and gap light transmission. *Agricultural and Forest Meteorology*, 109(4):249–263.

Frazer, G. W., Trofymow, J., and Lertzman, K. P. (2000). Canopy openness and leaf area in chronosequences of coastal temperate rainforests. *Canadian Journal of Forest Research*, 30(2):239–256.

Frey, S. J., Hadley, A. S., Johnson, S. L., Schulze, M., Jones, J. A., and Betts, M. G. (2016). Spatial models reveal the microclimatic buffering capacity of old-growth forests. *Science advances*, 2(4):e1501392.

Fusaro, L., Marando, F., Sebastiani, A., Capotorti, G., Blasi, C., Copiz, R., Congedo, L., Munafò, M., Ciancarella, L., and Manes, F. (2017). Mapping and assessment of PM_{10} and O_3 removal by woody vegetation at urban and regional level. *Remote Sensing*, 9(8):791.

Gao, F., Masek, J., Schwaller, M., and Hall, F. (2006). On the blending of the landsat and modis surface reflectance: Predicting daily landsat surface reflectance. *IEEE Transactions on Geoscience and Remote sensing*, 44(8):2207–2218.

García-Tejero, I. F., Ortega-Arévalo, C. J., Iglesias-Contreras, M., Moreno, J. M., Souza, L., Tavira, S. C., and Durán-Zuazo, V. H. (2018). Assessing the crop-water status in almond (*Prunus dulcis mill.*) trees via thermal imaging camera connected to smartphone. *Sensors*, 18(4):1–13.

Gardner, A. S., Maclean, I. M., and Gaston, K. J. (2019). Climatic predictors of species distributions neglect biophysiologically meaningful variables. *Diversity and Distributions*, 25(8):1318–1333.

Ge, W., Li, X., Jing, L., Han, J., and Wang, F. (2023). Monitoring canopy-scale autumn leaf phenology at fine-scale using unmanned aerial vehicle (UAV) photography. *Agricultural and Forest Meteorology*, 332:109372.

Geiger, R., Aron, R. H., and Todhunter, P. (1995). *The climate near the ground.* Friedr. Vieweg & Sohn Verlagsgesellschaft mbH, Wiesbaden, 5 edition.

Getzin, S., Nuske, R. S., and Wiegand, K. (2014). Using unmanned aerial vehicles (UAV) to quantify spatial gap patterns in forests. *Remote Sensing*, 6(8):6988–7004.

Gevaert, C. M., Tang, J., García-Haro, F. J., Suomalainen, J., and Kooistra, L. (2014). Combining hyperspectral uav and multispectral formosat-2 imagery for precision agriculture applications. In *2014 6th Workshop on Hyperspectral Image and Signal Processing: Evolution in Remote Sensing (WHISPERS)*, pages 1–4. IEEE.

Ginzler, C. and Hobi, M. L. (2015). Countrywide stereo-image matching for updating digital surface models in the framework of the Swiss National Forest Inventory. *Remote Sensing*, 7(4):4343–4370.

Giuggiola, A., Zweifel, R., Feichtinger, L. M., Vollenweider, P., Bugmann, H., Haeni, M., and Rigling, A. (2018). Competition for water in a xeric forest ecosystem – Effects of understory removal on soil micro-climate, growth and physiology of dominant Scots pine trees. *Forest Ecology and Management*, 409:241–249.

Glatthorn, J. and Beckschäfer, P. (2014). Standardizing the protocol for hemispherical photographs: Accuracy assessment of binarization algorithms. *PLoS ONE*, 9(11):e111924.

Gonsamo, A., D'odorico, P., and Pellikka, P. (2013). Measuring fractional forest canopy element cover and openness - definitions and methodologies revisited. *Oikos*, 122(9):1283–1291.

Gonsamo, A., Walter, J.-M. N., and Pellikka, P. (2010). Sampling gap fraction and size for estimating leaf area and clumping indices from hemispherical photographs. *Canadian Journal of Forest Research*, 40(8):1588–1603.

Gorelick, N., Hancher, M., Dixon, M., Ilyushchenko, S., Thau, D., and Moore, R. (2017). Google Earth Engine: Planetary-scale geospatial analysis for everyone. *Remote Sensing of Environment*, 202:18–27.

Gower, S. T., Kucharik, C. J., and Norman, J. M. (1999). Direct and indirect estimation of leaf area index, f(APAR), and net primary production of terrestrial ecosystems. *Remote Sensing of Environment*, 70(1):29–51.

Gräler, B., Pebesma, E., and Heuvelink, G. (2016). Spatio-temporal interpolation using gstat. *R Journal*, 8(1):204–218.

Gravel, D., Canham, C. D., Beaudet, M., and Messier, C. (2010). Shade tolerance, canopy gaps and mechanisms of coexistence of forest trees. *Oikos*, 119(3):475–484.

Greco, S. and Baldocchi, D. D. (1996). Seasonal variations of CO_2 and water vapour exchange rates over a temperate deciduous forest. *Global Change Biology*, 2(3):183–197.

Greiser, C., Meineri, E., Luoto, M., Ehrlén, J., and Hylander, K. (2018). Monthly microclimate models in a managed boreal forest landscape. *Agricultural and Forest Meteorology*, 250-251:147–158.

Gruen, A. (2012). Development and status of image matching in photogrammetry. *The Photogrammetric Record*, 27(137):36–57.

Haesen, S., Lembrechts, J. J., De Frenne, P., Lenoir, J., Aalto, J., Ashcroft, M. B., Kopecký, M., Luoto, M., Maclean, I., Nijs, I., Niittynen, P., van den Hoogen, J., Arriga, N., Brůna, J., Buchmann, N., Čiliak, M., Collalti, A., De Lombaerde, E., Descombes, P., Gharun, M., Goded, I., Govaert, S., Greiser, C., Grelle, A., Gruening, C., Hederová, L., Hylander, K., Kreyling, J., Kruijt, B., Macek, M., Máliš, F., Man, M., Manca, G., Matula, R., Meeussen, C., Merinero, S., Minerbi, S., Montagnani, L., Muffler, L., Ogaya, R., Penuelas, J., Plichta, R., Portillo-Estrada, M., Schmeddes, J., Shekhar, A., Spicher, F., Ujházyová, M., Vangansbeke, P., Weigel, R., Wild, J., Zellweger, F., and Van Meerbeek, K. (2021). ForestTemp – Sub-canopy microclimate temperatures of European forests. *Global Change Biology*, 27(23):6307–6319.

Hakkenberg, C. R., Tang, H., Burns, P., and Goetz, S. J. (2023). Canopy structure from space using GEDI lidar. *Frontiers in Ecology and the Environment*, 21(1):55–56.

Hale, S. E., Edwards, C., Mason, W. L., Price, M., and Peace, A. (2009). Relationships between canopy transmittance and stand parameters in Sitka spruce and Scots pine stands in Britain. *Forestry*, 82(5):503–513.

Hall, S., Burke, I., Box, D., Kaufmann, M., and Stoker, J. M. (2005). Estimating stand structure using discrete-return lidar: an example from low density, fire prone ponderosa pine forests. *Forest Ecology and Management*, 208(1-3):189–209.

Hardwick, S. R., Toumi, R., Pfeifer, M., Turner, E. C., Nilus, R., and Ewers, R. M. (2015). The relationship between leaf area index and microclimate in tropical forest and oil palm plantation: Forest disturbance drives changes in microclimate. *Agricultural and Forest Meteorology*, 201:187–195.

Hasegawa, H. and Yoshimura, T. (2003). Application of dual-frequency GPS receivers for static surveying under tree canopies. *Journal of Forest Research*, 8(2):0103–0110.

Hassan-Esfahani, L., Ebtehaj, A. M., Torres-Rua, A., and McKee, M. (2017). Spatial scale gap filling using an unmanned aerial system: A statistical downscaling method for applications in precision agriculture. *Sensors*, 17(9).

He, T., Liang, S., Wang, D., Cao, Y., Gao, F., Yu, Y., and Feng, M. (2018). Evaluating land surface albedo estimation from Landsat MSS, TM, ETM +, and

OLI data based on the unified direct estimation approach. *Remote Sensing of Environment*, 204:181–196.

Hengl, T., Heuvelink, G. B., Perčec Tadić, M., and Pebesma, E. J. (2012). Spatio-temporal prediction of daily temperatures using time-series of MODIS LST images. *Theoretical and applied climatology*, 107:265–277.

Hennon, P. E., D'Amore, D. V., Witter, D. T., and Lamb, M. B. (2010). Influence of forest canopy and snow on microclimate in a declining Yellow-Cedar forest of Southeast Alaska. *Northwest Science*, 84(1):73–87.

Hernández-Clemente, R., Hornero, A., Mottus, M., Penuelas, J., González-Dugo, V., Jiménez, J. C., Suárez, L., Alonso, L., and Zarco-Tejada, P. J. (2019). Early diagnosis of vegetation health from high-resolution hyperspectral and thermal imagery: Lessons learned from empirical relationships and radiative transfer modelling. *Current Forestry Reports*, 5(3):169–183.

Hesslerová, P., Pokornỳ, J., Brom, J., and Rejšková-Procházková, A. (2013). Daily dynamics of radiation surface temperature of different land cover types in a temperate cultural landscape: Consequences for the local climate. *Ecological engineering*, 54:145–154.

Hewitt, C. D. (2004). Ensembles-based predictions of climate changes and their impacts. *Eos, Transactions American Geophysical Union*, 85(52):566 – 566.

Hicks, B. B., Baldocchi, D. D., Meyers, T. P., Hosker, R. P., and Matt, D. R. (1987). A preliminary multiple resistance routine for deriving dry deposition velocities from measured quantities. *Water, Air, and Soil Pollution*, 36(3-4):311–330.

Hiemstra, P. H., Pebesma, E. J., Twenhöfel, C. J., and Heuvelink, G. B. (2008). Real-time automatic interpolation of ambient gamma dose rates from the Dutch radioactivity monitoring network. *Computers and Geosciences*, 35(8):1711–1721.

Hijmans, R. J., Cameron, S. E., Parra, J. L., Jones, P. G., and Jarvis, A. (2005). Very high resolution interpolated climate surfaces for global land areas. *International Journal of Climatology*, 25(15):1965–1978.

Hill, R. (1924). A lens for whole sky photographs. *Quarterly Journal of the Royal Meteorological Society*, 50(211):227–235.

Hirschmugl, M., Ofner, M., Raggam, J., and Schardt, M. (2007). Single tree detection in very high resolution remote sensing data. *Remote Sensing of Environment*, 110(4):533–544.

Hovi, A., Liang, J., Korhonen, L., Kobayashi, H., and Rautiainen, M. (2016). Quantifying the missing link between forest albedo and productivity in the boreal zone. *Biogeosciences*, 13(21):6015–6030.

Hu, G., Liu, H., Anenkhonov, O. A., Korolyuk, A. Y., Sandanov, D. V., and Guo, D. (2013). Forest buffers soil temperature and postpones soil thaw as indicated by a three-year large-scale soil temperature monitoring in the forest-steppe ecotone in Inner Asia. *Global and Planetary Change*, 104:1–6.

Huang, C.-W., Chu, C.-R., Hsieh, C.-I., Palmroth, S., and Katul, G. G. (2015). Wind-induced leaf transpiration. *Advances in Water Resources*, 86:240–255.

Huey, R. B., Kearney, M. R., Krockenberger, A., Holtum, J. A., Jess, M., and Williams, S. E. (2012). Predicting organismal vulnerability to climate warming: Roles of behaviour, physiology and adaptation. *Philosophical Transactions of the Royal Society B: Biological Sciences*, 367(1596):1665–1679.

Hylander, K. (2005). Aspect modifies the magnitude of edge effects on bryophyte growth in boreal forests. *Journal of Applied Ecology*, 42(3):518–525.

Hyyppä, E., Yu, X., Kaartinen, H., Hakala, T., Kukko, A., Vastaranta, M., and Hyyppä, J. (2020). Comparison of backpack, handheld, under-canopy UAV, and above-canopy UAV laser scanning for field reference data collection in boreal forests. *Remote Sensing*, 12(20):1–31.

Hyyppä, J. and Hallikainen, M. (1996). Applicability of airborne profiling radar to forest inventory. *Remote Sensing of Environment*, 57(1):39–57.

Hyyppa, J., Kelle, O., Lehikoinen, M., and Inkinen, M. (2001). A segmentation-based method to retrieve stem volume estimates from 3-D tree height models produced by laser scanners. *IEEE Transactions on geoscience and remote sensing*, 39(5):969–975.

Igawa, N., Koga, Y., Matsuzawa, T., and Nakamura, H. (2004). Models of sky radiance distribution and sky luminance distribution. *Solar Energy*, 77(2):137–157.

IPCC (2013). *Climate change 2013: The physical science basis. Contribution of working group I to the Fifth assessment report of the Intergovernmental Panel on Climate Change.* Cambridge University Press, Cambridge, New York.

Isibue, E. W. and Pingel, T. J. (2020). Unmanned aerial vehicle based measurement of urban forests. *Urban Forestry & Urban Greening*, 48:126574.

Jakubowski, M. K., Guo, Q., and Kelly, M. (2013). Tradeoffs between lidar pulse density and forest measurement accuracy. *Remote Sensing of Environment*, 130:245–253.

Janhäll, S. (2015). Review on urban vegetation and particle air pollution - Deposition and dispersion. *Atmospheric Environment*, 105:130–137.

Jarčuška, B., Kucbel, S., and Jaloviar, P. (2010). Comparison of output results from two programmes for hemispherical image analysis: Gap light analyser and winscanopy. *Journal of Forest Science*, 56(4):147–153.

Jarvis, P. G. and McNaughton, K. (1986). Stomatal control of transpiration: scaling up from leaf to region. *Advances in Ecological Research*, 15:1–49.

Jenerowicz, A. and Woroszkiewicz, M. (2016). The pan-sharpening of satellite and UAV imagery for agricultural applications. *Remote Sensing for Agriculture, Ecosystems, and Hydrology XVIII*, 9998:99981S.

Jennings, S. B., Brown, N. D., and Sheil, D. (1999). Assessing forest canopies and understorey illumination: canopy closure, canopy cover and other measures. *Forestry*, 72(1):59–74.

Jiang, Y. and Weng, Q. (2017). Estimation of hourly and daily evapotranspiration and soil moisture using downscaled LST over various urban surfaces. *GIScience and Remote Sensing*, 54(1):95–117.

Jiménez-Muñoz, J. C., Sobrino, J. A., Skoković, D., Mattar, C., and Cristobal, J. (2014). Land surface temperature retrieval methods from Landsat-8 thermal infrared sensor data. *IEEE Geoscience and Remote Sensing Letters*, 11(10):1840–1843.

Jonckheere, I., Fleck, S., Nackaerts, K., Muys, B., Coppin, P., Weiss, M., and Baret, F. (2004). Review of methods for in situ leaf area index determination: Part I. Theories, sensors and hemispherical photography. *Agricultural and Forest Meteorology*, 121(1-2):19–35.

Jonckheere, I. G., Muys, B., and Coppin, P. R. (2005). Derivative analysis for in situ high dynamic range hemispherical photography and its application in forest stands. *IEEE Geoscience and Remote Sensing Letters*, 2(3):296–300.

Jucker, T., Hardwick, S. R., Both, S., Elias, D. M., Ewers, R. M., Milodowski, D. T., Swinfield, T., and Coomes, D. A. (2018). Canopy structure and topography

jointly constrain the microclimate of human-modified tropical landscapes. *Global Change Biology*, 24(11):5243–5258.

Junttila, S., Vastaranta, M., Hämäläinen, J., Latva-Käyrä, P., Holopainen, M., Hernandez Clemente, R., Hyyppä, H., and Navarro-Cerrillo, R. M. (2017). Effect of forest structure and health on the relative surface temperature captured by airborne thermal imagery–Case study in Norway Spruce-dominated stands in Southern Finland. *Scandinavian Journal of Forest Research*, 32(2):154–165.

Karger, D. N., Conrad, O., Böhner, J., Kawohl, T., Kreft, H., Soria-Auza, R. W., Zimmermann, N. E., Linder, H. P., and Kessler, M. (2017). Climatologies at high resolution for the earth's land surface areas. *Scientific data*, 4(1):1–20.

Kašpar, V., Hederová, L., Macek, M., Müllerová, J., Prošek, J., Surový, P., Wild, J., and Kopecký, M. (2021). Temperature buffering in temperate forests: Comparing microclimate models based on ground measurements with active and passive remote sensing. *Remote Sensing of Environment*, 263:112522.

Kay, M. (2020). ggdist: Visualizations of distributions and uncertainty. R package version 2.2.0.

Kearney, M. R. and Porter, W. P. (2020). NicheMapR – an R package for biophysical modelling: the ectotherm and dynamic energy budget models. *Ecography*, 43(1):85–96.

Kellner, J. R., Armston, J., Birrer, M., Cushman, K. C., Duncanson, L., Eck, C., Falleger, C., Imbach, B., Král, K., Krůček, M., Trochta, J., Vrška, T., and Zgraggen, C. (2019). New opportunities for forest remote sensing through ultra-high-density drone LiDAR. *Surveys in Geophysics*, 40(4):959–977.

Kim, D. W., Yun, H. S., Jeong, S. J., Kwon, Y. S., Kim, S. G., Lee, W. S., and Kim, H. J. (2018). Modeling and testing of growth status for Chinese cabbage and white radish with UAV-based RGB imagery. *Remote Sensing*, 10(4).

Klosterman, S. and Richardson, A. D. (2017). Observing spring and fall phenology in a deciduous forest with aerial drone imagery. *Sensors*, 17(2852):1–17.

Komárek, J., Klouček, T., and Prošek, J. (2018). The potential of Unmanned Aerial Systems: A tool towards precision classification of hard-to-distinguish vegetation types? *International Journal of Applied Earth Observation and Geoinformation*, 71:9–19.

Konarska, J., Uddling, J., Holmer, B., Lutz, M., Lindberg, F., Pleijel, H., and Thorsson, S. (2016). Transpiration of urban trees and its cooling effect in a high latitude city. *International journal of biometeorology*, 60:159–172.

Kopeckỳ, M., Macek, M., and Wild, J. (2021). Topographic wetness index calculation guidelines based on measured soil moisture and plant species composition. *Science of the Total Environment*, 757:143785.

Korhonen, L., Korhonen, K. T., Rautiainen, M., and Stenberg, P. (2006). Estimation of forest canopy cover: A comparison of field measurement techniques. *Silva Fennica*, 40(4):577–588.

Körner, C. and Hiltbrunner, E. (2018). The 90 ways to describe plant temperature. *Perspectives in Plant Ecology, Evolution and Systematics*, 30:16–21.

Körner, C. and Paulsen, J. (2004). A world-wide study of high altitude treeline temperatures. *Journal of biogeography*, 31(5):713–732.

Kovács, B., Tinya, F., Németh, C., and Ódor, P. (2020). Unfolding the effects of different forestry treatments on microclimate in oak forests: results of a 4-yr experiment. *Ecological Applications*, 30(2):e02043.

Kozáková, J., Pokorná, P., Vodička, P., Ondráčková, L., Ondráček, J., Křmal, K., Mikuška, P., Hovorka, J., Moravec, P., and Schwarz, J. (2019). The influence of local emissions and regional air pollution transport on a European air pollution hot spot. *Environmental science and pollution research*, 26:1675–1692.

Kuhn, M. (2008). Building predictive models in R using the caret package. *Journal of Statistical Software*, 28(5):1–26.

Kumar, P., Morawska, L., Martani, C., Biskos, G., Neophytou, M., Di Sabatino, S., Bell, M., Norford, L., and Britter, R. (2015). The rise of low-cost sensing for managing air pollution in cities. *Environment International*, 75:199–205.

Kuusinen, N., Kolari, P., Levula, J., Porcar-Castell, A., Stenberg, P., and Berninger, F. (2012). Seasonal variation in boreal pine forest albedo and effects of canopy snow on forest reflectance. *Agricultural and Forest Meteorology*, 164:53–60.

Kuusinen, N., Lukeš, P., Stenberg, P., Levula, J., Nikinmaa, E., and Berninger, F. (2014a). Measured and modelled albedos in Finnish boreal forest stands of different species, structure and understory. *Ecological Modelling*, 284:10–18.

Kuusinen, N., Tomppo, E., Shuai, Y., and Berninger, F. (2014b). Effects of forest age on albedo in boreal forests estimated from MODIS and Landsat albedo retrievals. *Remote Sensing of Environment*, 145:145–153.

Kuželka, K., Slavík, M., and Surový, P. (2020). Very high density point clouds from UAV laser scanning for automatic tree stem detection and direct diameter measurement. *Remote Sensing*, 12(8).

Laisk, A., Kull, O., and Moldau, H. (1989). Ozone concentration in leaf intercellular air spaces is close to zero. *Plant Physiology*, 90(3):1163–1167.

Lang, N., Jetz, W., Schindler, K., and Wegner, Jan, D. (2022). A high-resolution canopy height model of the Earth. *arXiv preprint*, arXiv:2204.08322.

Laskin, D. N., Montaghi, A., and McDermid, G. J. (2017). An open-source method of constructing cloud-free composites of forest understory temperature using MODIS. *Remote Sensing Letters*, 8(2):165–174.

Latifi, H., Heurich, M., Hartig, F., Müller, J., Krzystek, P., Jehl, H., and Dech, S. (2016). Estimating over- and understorey canopy density of temperate mixed stands by airborne LiDAR data. *Forestry*, 89(1):69–81.

Leblanc, S. G., Chen, J. M., Fernandes, R., Deering, D. W., and Conley, A. (2005). Methodology comparison for canopy structure parameters extraction from digital hemispherical photography in boreal forests. *Agricultural and Forest Meteorology*, 129(3-4):187–207.

Legendre, P. and Legendre, L. (2012). *Numerical Ecology*, volume 24. Elsevier, 3rd edition.

Lembrechts, J. J., Aalto, J., Ashcroft, M. B., De Frenne, P., Kopecký, M., Lenoir, J., Luoto, M., Maclean, I. M., Roupsard, O., Fuentes-Lillo, E., García, R. A., Pellissier, L., Pitteloud, C., Alatalo, J. M., Smith, S. W., Björk, R. G., Muffler, L., Ratier Backes, A., Cesarz, S., Gottschall, F., Okello, J., Urban, J., Plichta, R., Svátek, M., Phartyal, S. S., Wipf, S., Eisenhauer, N., Pușcaș, M., Turtureanu, P. D., Varlagin, A., Dimarco, R. D., Jump, A. S., Randall, K., Dorrepaal, E., Larson, K., Walz, J., Vitale, L., Svoboda, M., Finger Higgens, R., Halbritter, A. H., Curasi, S. R., Klupar, I., Koontz, A., Pearse, W. D., Simpson, E., Stemkovski, M., Jessen Graae, B., Vedel Sørensen, M., Høye, T. T., Fernández Calzado, M. R., Lorite, J., Carbognani, M., Tomaselli, M., Forte, T. G., Petraglia, A., Haesen, S., Somers, B., Van Meerbeek, K., Björkman, M. P., Hylander, K., Merinero, S., Gharun, M., Buchmann, N., Dolezal, J., Matula, R., Thomas,

A. D., Bailey, J. J., Ghosn, D., Kazakis, G., de Pablo, M. A., Kemppinen, J., Niittynen, P., Rew, L., Seipel, T., Larson, C., Speed, J. D., Ardö, J., Cannone, N., Guglielmin, M., Malfasi, F., Bader, M. Y., Canessa, R., Stanisci, A., Kreyling, J., Schmeddes, J., Teuber, L., Aschero, V., Čiliak, M., Máliš, F., De Smedt, P., Govaert, S., Meeussen, C., Vangansbeke, P., Gigauri, K., Lamprecht, A., Pauli, H., Steinbauer, K., Winkler, M., Ueyama, M., Nuñez, M. A., Ursu, T. M., Haider, S., Wedegärtner, R. E., Smiljanic, M., Trouillier, M., Wilmking, M., Altman, J., Brůna, J., Hederová, L., Macek, M., Man, M., Wild, J., Vittoz, P., Pärtel, M., Barančok, P., Kanka, R., Kollár, J., Palaj, A., Barros, A., Mazzolari, A. C., Bauters, M., Boeckx, P., Benito Alonso, J. L., Zong, S., Di Cecco, V., Sitková, Z., Tielbörger, K., van den Brink, L., Weigel, R., Homeier, J., Dahlberg, C. J., Medinets, S., Medinets, V., De Boeck, H. J., Portillo-Estrada, M., Verryckt, L. T., Milbau, A., Daskalova, G. N., Thomas, H. J., Myers-Smith, I. H., Blonder, B., Stephan, J. G., Descombes, P., Zellweger, F., Frei, E. R., Heinesch, B., Andrews, C., Dick, J., Siebicke, L., Rocha, A., Senior, R. A., Rixen, C., Jimenez, J. J., Boike, J., Pauchard, A., Scholten, T., Scheffers, B., Klinges, D., Basham, E. W., Zhang, J., Zhang, Z., Géron, C., Fazlioglu, F., Candan, O., Sallo Bravo, J., Hrbacek, F., Laska, K., Cremonese, E., Haase, P., Moyano, F. E., Rossi, C., and Nijs, I. (2020). SoilTemp: A global database of near-surface temperature. *Global Change Biology*, 26(11):6616–6629.

Lembrechts, J. J., Nijs, I., and Lenoir, J. (2019). Incorporating microclimate into species distribution models. *Ecography*, 42:1267–1279.

Lembrechts, J. J., van den Hoogen, J., Aalto, J., Ashcroft, M. B., De Frenne, P., Kemppinen, J., Kopecký, M., Luoto, M., Maclean, I. M., Crowther, T. W., et al. (2022). Global maps of soil temperature. *Global Change Biology*, 28(9):3110–3144.

Lemmon, P. E. (1956). A spherical densiometer for estimating forest overstory density. *Forest science*, 2(4):314–320.

Lenoir, J., Graae, B. J., Aarrestad, P. A., Alsos, I. G., Armbruster, W. S., Austrheim, G., Bergendorff, C., Birks, H. J. B., Bråthen, K. A., Brunet, J., et al. (2013). Local temperatures inferred from plant communities suggest strong spatial buffering of climate warming across Northern Europe. *Global Change Biology*, 19(5):1470–1481.

Lenoir, J., Hattab, T., and Pierre, G. (2017). Climatic microrefugia under anthropogenic climate change: implications for species redistribution. *Ecography*, 40(2):253–266.

Lenoir, J. and Svenning, J.-C. (2015). Climate-related range shifts–a global multi-dimensional synthesis and new research directions. *Ecography*, 38(1):15–28.

Lesser, M. R. and Fridley, J. D. (2016). Global change at the landscape level: Relating regional and landscape-scale drivers of historical climate trends in the Southern Appalachians. *International Journal of Climatology*, 36(3):1197–1209.

Leuzinger, S. and Körner, C. (2007). Tree species diversity affects canopy leaf temperatures in a mature temperate forest. *Agricultural and Forest Meteorology*, 146(1-2):29–37.

Levy, C. R., Burakowski, E., and Richardson, A. D. (2018). Novel measurements of fine-scale albedo: Using a commercial quadcopter to measure radiation fluxes. *Remote Sensing*, 10(8):14–20.

Li, W., Niu, Z., Shang, R., Qin, Y., Wang, L., and Chen, H. (2020). High-resolution mapping of forest canopy height using machine learning by coupling ICESat-2 LiDAR with Sentinel-1, Sentinel-2 and Landsat-8 data. *International Journal of Applied Earth Observation and Geoinformation*, 92:102163.

Liang, X., Kankare, V., Hyyppä, J., Wang, Y., Kukko, A., Haggrén, H., Yu, X., Kaartinen, H., Jaakkola, A., Guan, F., et al. (2016). Terrestrial laser scanning in forest inventories. *ISPRS Journal of Photogrammetry and Remote Sensing*, 115:63–77.

Liu, H., Dahlgren, R. A., Larsen, R. E., Devine, S. M., Roche, L. M., O' Geen, A. T., Wong, A. J., Covello, S., and Jin, Y. (2019). Estimating rangeland forage production using remote sensing data from a Small Unmanned Aerial System (sUAS) and planetscope satellite. *Remote Sensing*, 11(5).

Liu, J., Skidmore, A. K., Jones, S., Wang, T., Heurich, M., Zhu, X., and Shi, Y. (2018). Large off-nadir scan angle of airborne lidar can severely affect the estimates of forest structure metrics. *ISPRS journal of photogrammetry and remote sensing*, 136:13–25.

Lovell, J. L., Jupp, D. L., Culvenor, D. S., and Coops, N. C. (2003). Using airborne and ground-based ranging lidar to measure canopy structure in Australian forests. *Canadian Journal of Remote Sensing*, 29(5):607–622.

Lowman, M. (2021). Life in the treetops—An overview of forest canopy science and its future directions. *Plants People Planet*, 3(1):16–21.

Lukeš, P., Rautiainen, M., Manninen, T., Stenberg, P., and Mõttus, M. (2014). Geographical gradients in boreal forest albedo and structure in Finland. *Remote Sensing of Environment*, 152:526–535.

Lusk, C. H. (2022). A field test of forest canopy structure measurements with the canopycapture smartphone application. *PeerJ*, 10:e13450.

Macek, M., Kopecký, M., and Wild, J. (2019). Maximum air temperature controlled by landscape topography affects plant species composition in temperate forests. *Landscape Ecology*, 34(11):2541–2556.

Macfarlane, C., Bond, C., White, D. A., Grigg, A. H., Ogden, G. N., and Silberstein, R. (2010). Transpiration and hydraulic traits of old and regrowth eucalypt forest in southwestern australia. *Forest ecology and management*, 260(1):96–105.

Machado, J.-l. and Reich, P. B. (1999). Evaluation of several measures of canopy openness as predictors of photosynthetic photon flux density in deeply shaded confier-dominated forest understory. *Canadian Journal of Forest Research*, 29:1438–1444.

Maclean, I. M. (2020). Predicting future climate at high spatial and temporal resolution. *Global Change Biology*, 26(2):1003–1011.

Maclean, I. M. and Klinges, D. H. (2021). Microclimc: A mechanistic model of above, below and within-canopy microclimate. *Ecological Modelling*, 451(November 2020):109567.

Maclean, I. M., Mosedale, J. R., and Bennie, J. J. (2019). Microclima: An R package for modelling meso-and microclimate. *Methods in Ecology and Evolution*, 10(2):280–290.

Maclean, I. M., Suggitt, A. J., Wilson, R. J., Duffy, J. P., and Bennie, J. J. (2017). Fine-scale climate change: modelling spatial variation in biologically meaningful rates of warming. *Global Change Biology*, 23(1):256–268.

Maltamo, M., Naesset, E., and Vauhkonen, J. (2014). *Forestry applications of airborne laser scanning*, volume 27. Springer Netherlands, 1 edition.

Manes, F., Marando, F., Capotorti, G., Blasi, C., Salvatori, E., Fusaro, L., Ciancarella, L., Mircea, M., Marchetti, M., Chirici, G., and Munafò, M. (2016). Regulating ecosystem services of forests in ten Italian Metropolitan Cities: Air quality improvement by PM_{10} and O_3 removal. *Ecological Indicators*, 67(2016):425–440.

Marsh, C. D., Hill, R. A., Nowak, M. G., Hankinson, E., Abdullah, A., Gillingham, P., and Korstjens, A. H. (2022). Measuring and modelling microclimatic air temperature in a historically degraded tropical forest. *International Journal of Biometeorology*, 66(6):1283–1295.

McArdle, B. H. and Anderson, M. J. (2001). Fitting multivariate models to community data: A comment on distance-based redundancy analysis. *Ecology*, 82(1):290–297.

McDowell, N. G., Beerling, D. J., Breshears, D. D., Fisher, R. A., Raffa, K. F., and Stitt, M. (2011). The interdependence of mechanisms underlying climate-driven vegetation mortality. *Trends in Ecology & Evolution*, 26(10):523–532.

Meili, N., Manoli, G., Burlando, P., Carmeliet, J., Chow, W. T., Coutts, A. M., Roth, M., Velasco, E., Vivoni, E. R., and Fatichi, S. (2021). Tree effects on urban microclimate: Diurnal, seasonal, and climatic temperature differences explained by separating radiation, evapotranspiration, and roughness effects. *Urban Forestry & Urban Greening*, 58:126970.

Meineri, E. and Hylander, K. (2017). Fine-grain, large-domain climate models based on climate station and comprehensive topographic information improve microrefugia detection. *Ecography*, 40(8):1003–1013.

Metz, M., Andreo, V., and Neteler, M. (2017). A new fully gap-free time series of land surface temperature from MODIS LST data. *Remote Sensing*, 9(12):1333.

Meyer, H., Katurji, M., Appelhans, T., Müller, M. U., Nauss, T., Roudier, P., and Zawar-Reza, P. (2016). Mapping daily air temperature for Antarctica based on MODIS LST. *Remote Sensing*, 8(9):732.

Milling, C. R., Rachlow, J. L., Olsoy, P. J., Chappell, M. A., Johnson, T. R., Forbey, J. S., Shipley, L. A., and Thornton, D. H. (2018). Habitat structure modifies microclimate: An approach for mapping fine-scale thermal refuge. *Methods in Ecology and Evolution*, 9(6):1648–1657.

Mitchard, E. T., Saatchi, S. S., White, L. J., Abernethy, K. A., Jeffery, K. J., Lewis, S. L., Collins, M., Lefsky, M. A., Leal, M. E., Woodhouse, I. H., et al. (2012). Mapping tropical forest biomass with radar and spaceborne LiDAR in Lopé National Park, Gabon: overcoming problems of high biomass and persistent cloud. *Biogeosciences*, 9(1):179–191.

Mitchard, E. T., Saatchi, S. S., Woodhouse, I. H., Nangendo, G., Ribeiro, N., Williams, M., Ryan, C. M., Lewis, S. L., Feldpausch, T., and Meir, P. (2009). Using satellite radar backscatter to predict above-ground woody biomass: A consistent relationship across four different african landscapes. *Geophysical Research Letters*, 36(23).

Mitchell, R., Maher, B., and Kinnersley, R. (2010). Rates of particulate pollution deposition onto leaf surfaces: temporal and inter-species magnetic analyses. *Environmental Pollution*, 158(5):1472–1478.

Moeser, D., Roubinek, J., Schleppi, P., Morsdorf, F., and Jonas, T. (2014). Canopy closure, LAI and radiation transfer from airborne LiDAR synthetic images. *Agricultural and Forest Meteorology*, 197:158–168.

Monin, A. S. and Obukhov, A. M. (1954). Basic laws of turbulent mixing in the surface layer of the atmosphere. *Tr. Akad. Nauk SSSR Geofiz. Inst.*, 24(151):163–187.

Monsi, M. and Saeki, T. (1953). Über den Lichtfaktor in den Pflanzengesellschaften und seine Bedeutung für die Stoffproduktion. *Japanese Journal of Botany*, 14:22–52.

Monteith, J. L. (1965). Evaporation and environment. In *Symposia of the society for experimental biology*, volume 19, pages 205–234. Cambridge University Press (CUP) Cambridge.

Montesano, P. M., Cook, B. D., Sun, G., Simard, M., Nelson, R. F., Ranson, K. J., Zhang, Z., and Luthcke, S. (2013). Achieving accuracy requirements for forest biomass mapping: A spaceborne data fusion method for estimating forest biomass and LiDAR sampling error. *Remote Sensing of Environment*, 130:153–170.

Moosavi, V., Talebi, A., Mokhtari, M. H., Shamsi, S. R. F., and Niazi, Y. (2015). A wavelet-artificial intelligence fusion approach (WAIFA) for blending Landsat and MODIS surface temperature. *Remote Sensing of Environment*, 169:243–254.

Morani, A., Nowak, D. J., Hirabayashi, S., and Calfapietra, C. (2011). How to select the best tree planting locations to enhance air pollution removal in the MillionTreesNYC initiative. *Environmental Pollution*, 159(5):1040–1047.

Morecroft, M. D., Taylor, M. E., and Oliver, H. R. (1998). Air and soil microclimates of deciduous woodland compared to an open site. *Agricultural and Forest Meteorology*, 90(1-2):141–156.

Moudrý, V., Cord, A. F., Gábor, L., Laurin, G. V., Barták, V., Gdulová, K., Malavasi, M., Rocchini, D., Stereńczak, K., Prošek, J., et al. (2023a). Vegetation structure derived from airborne laser scanning to assess species distribution and habitat suitability: The way forward. *Diversity and Distributions*, 29(1):39–50.

Moudrý, V., Keil, P., Cord, A. F., Gábor, L., Lecours, V., Zarzo-Arias, A., Barták, V., Malavasi, M., Rocchini, D., Torresani, M., et al. (2023b). Scale mismatches between predictor and response variables in species distribution modelling: A review of practices for appropriate grain selection. *Progress in Physical Geography: Earth and Environment*, page 03091333231156362.

Moudrý, V., Urban, R., Štroner, M., Komárek, J., Brouček, J., and Prošek, J. (2019). Comparison of a commercial and home-assembled fixed-wing UAV for terrain mapping of a post-mining site under leaf-off conditions. *International Journal of Remote Sensing*, 40(2):555–572.

Müllerová, J., Bartaloš, T., Brůna, J., Dvořák, P., and Vítková, M. (2017). Unmanned aircraft in nature conservation: an example from plant invasions. *International Journal of Remote Sensing*, 38(8-10):2177–2198.

Muñoz Sabater, J. et al. (2019). ERA5-Land hourly data from 1981 to present. *Copernicus Climate Change Service (C3S) Climate Data Store (CDS)*, 10(10.24381).

Nadeau, C. P., Urban, M. C., and Bridle, J. R. (2017). Coarse climate change projections for species living in a fine-scaled world. *Global Change Biology*, 23(1):12–24.

Naesset, E. (1997). Determination of mean tree height of forest stands using airborne laser scanner data. *ISPRS Journal of Photogrammetry and Remote sensing*, 52(2):49–56.

Naesset, E. and Jonmeister, T. (2002). Assessing point accuracy of DGPS under forest canopy before data acquisition, in the field and after postprocessing. *Scandinavian Journal of Forest Research*, 17(4):351–358.

Nakamura, A., Kitching, R. L., Cao, M., Creedy, T. J., Fayle, T. M., Freiberg, M., Hewitt, C., Itioka, T., Koh, L. P., Ma, K., et al. (2017). Forests and their canopies: achievements and horizons in canopy science. *Trends in Ecology & Evolution*, 32(6):438–451.

Neteler, M. (2010). Estimating daily land surface temperatures in mountainous environments by reconstructed MODIS LST data. *Remote sensing*, 2(1):333–351.

Neuville, R., Bates, J. S., and Jonard, F. (2021). Estimating forest structure from UAV-mounted LiDAR point cloud using machine learning. *Remote Sensing*, 13(3):1–19.

Nobis, M. (2005). SideLook 1.1 - Imaging software for the analysis of vegetation structure with true-colour photographs.

Nobis, M. and Hunziker, U. (2005). Automatic thresholding for hemispherical canopy-photographs based on edge detection. *Agricultural and Forest Meteorology*, 128(3-4):243–250.

Noszczyk, T., Gorzelany, J., Kukulska-Kozieł, A., and Hernik, J. (2022). The impact of the COVID-19 pandemic on the importance of urban green spaces to the public. *Land Use Policy*, 113(May 2021).

Novakova, L. and Pavlis, T. L. (2019). Modern methods in structural geology of twenty-first century: Digital mapping and digital devices for the field geology. *Teaching methodologies in structural geology and tectonics*, pages 43–54.

Nowak, D. J. (1996). Estimating leaf area and leaf biomass of open-grown deciduous urban trees. *Forest science*, 42(4):504–507.

Nowak, D. J. and Crane, D. E. (2000). The Urban Forest Effects (UFORE) Model: quantifying urban forest structure and functions.

Nowak, D. J., Crane, D. E., and Stevens, J. C. (2006). Air pollution removal by urban trees and shrubs in the united states. *Urban Forestry & Urban Greening*, 4(3-4):115–123.

Økland, R. H. (1999). On the variation explained by ordination and constrained ordination axes. *Journal of Vegetation Science*, 10(1):131–136.

Oksanen, J., Blanchet, F. G., Kindt, R., Legendre, P., Minchin, P. R., O'Hara, R., Simpson, G. L., Solymos, P., Stevens, M. H. H., Wagner, H., et al. (2013). Package 'vegan'. *Community ecology package, version*, 2(9):1–295.

Orlanski, I. (1975). A rational subdivision of scales for atmospheric processes. *Bulletin of the American Meteorological Society*, pages 527–530.

Pacifici, M., Foden, W. B., Visconti, P., Watson, J. E., Butchart, S. H., Kovacs, K. M., Scheffers, B. R., Hole, D. G., Martin, T. G., Akçakaya, H. R., Corlett, R. T., Huntley, B., Bickford, D., Carr, J. A., Hoffmann, A. A., Midgley, G. F., Pearce-Kelly, P., Pearson, R. G., Williams, S. E., Willis, S. G., Young, B., and

Rondinini, C. (2015). Assessing species vulnerability to climate change. *Nature Climate Change*, 5(3):215–225.

Pan, Y., Birdsey, R. A., Phillips, O. L., and Jackson, R. B. (2013). The structure, distribution, and biomass of the world's forests. *Annual Review of Ecology, Evolution, and Systematics*, 44:593–622.

Paul, K. I., Polglase, P. J., Smethurst, P. J., O'Connell, A. M., Carlyle, C. J., and Khanna, P. K. (2004). Soil temperature under forests: A simple model for predicting soil temperature under a range of forest types. *Agricultural and Forest Meteorology*, 121(3-4):167–182.

Pfeifer, M., Boyle, M. J., Dunning, S., and Olivier, P. I. (2019). Forest floor temperature and greenness link significantly to canopy attributes in South Africa's fragmented coastal forests. *PeerJ*, 2019(1):1–26.

Pfeifer, M., Gonsamo, A., Disney, M., Pellikka, P., and Marchant, R. (2012). Leaf area index for biomes of the Eastern Arc Mountains: Landsat and SPOT observations along precipitation and altitude gradients. *Remote Sensing of Environment*, 118:103–115.

Pierce, L. L. and Running, S. W. (1988). Rapid estimation of coniferous forest leaf area index using a portable integrating radiometer. *Ecology*, 69(6):1762–1767.

Pinker, R. T. (1985). Determination of surface albedo from satellites. *Advances in Space Research*, 5(6):333–343.

Pokorná, P., Hovorka, J., Klán, M., and Hopke, P. (2015). Source apportionment of size resolved particulate matter at a european air pollution hot spot. *Science of the Total Environment*, 502:172–183.

Popescu, S. C. and Wynne, R. H. (2004). Seeing the trees in the forest: Using lidar and multispectral data fusion with local filtering and variable window size for estimating tree height. *Photogrammetric engineering and remote sensing*, 70(5):589–604.

Popescu, S. C., Zhou, T., Nelson, R., Neuenschwander, A., Sheridan, R., Narine, L., and Walsh, K. M. (2018). Photon counting LiDAR: An adaptive ground and canopy height retrieval algorithm for ICESat-2 data. *Remote Sensing of Environment*, 208:154–170.

Porter, W. P., Mitchell, J. W., Beckman, W. A., and DeWitt, C. B. (1973). Behavioral implications of mechanistic ecology. *Oecologia*, 13(1):1–54.

Potapov, P., Li, X., Hernandez-Serna, A., Tyukavina, A., Hansen, M. C., Kommareddy, A., Pickens, A., Turubanova, S., Tang, H., Silva, C. E., Armston, J., Dubayah, R., Blair, J. B., and Hofton, M. (2021). Mapping global forest canopy height through integration of GEDI and Landsat data. *Remote Sensing of Environment*, 253(August):112165.

Potter, K. A., Arthur Woods, H., and Pincebourde, S. (2013). Microclimatic challenges in global change biology. *Global Change Biology*, 19(10):2932–2939.

Promis, A., Gärtner, S., Butler-Manning, D., Durán-Rangel, C., Reif, A., Cruz, G., and Hernández, L. (2011). Comparison of four different programs for the analysis of hemispherical photographs using parameters of canopy structure and solar radiation transmittance. *Sierra*, 519:36.

Puliti, S., Ørka, H. O., Gobakken, T., and Næsset, E. (2015). Inventory of small forest areas using an unmanned aerial system. *Remote Sensing*, 7(8):9632–9654.

Qi, W., Lee, S.-K., Hancock, S., Luthcke, S., Tang, H., Armston, J., and Dubayah, R. (2019). Improved forest height estimation by fusion of simulated GEDI Lidar data and TanDEM-X InSAR data. *Remote Sensing of Environment*, 221:621–634.

Qu, Z., Oumbe, A., Blanc, P., Espinar, B., Gesell, G., GSCHwIND, B., Klüser, L., Lefèvre, M., Saboret, L., Schroedter-Homscheidt, M., et al. (2017). Fast radiative transfer parameterisation for assessing the surface solar irradiance: The Heliosat-4 method. *Meteorologische Zeitschrift*, 26(1):33–57.

Rahman, M. M., McDermid, G. J., Mckeeman, T., and Lovitt, J. (2019). A workflow to minimize shadows in UAV-based orthomosaics. *Journal of Unmanned Vehicle Systems*, 7(2):107–117.

Raupach, M. R. (1994). Simplified expressions for vegetation roughness length and zero-plane displacement as functions of canopy height and area index. *Boundary-layer meteorology*, 71(1-2):211–216.

Rich, P. M. (1990). Characterizing plant canopies with hemispherical photographs. *Remote Sensing Reviews*, 5(1):13–29.

Richter, R., Hutengs, C., Wirth, C., Bannehr, L., and Vohland, M. (2021). Detecting tree species effects on forest canopy temperatures with thermal remote sensing: The role of spatial resolution. *Remote Sensing*, 13(1):135.

Ripley, B., Venables, B., Bates, D. M., Hornik, K., Gebhardt, A., Firth, D., and Ripley, M. B. (2013). Package 'mass'. *Cran R*, 538:113–120.

Roussel, J.-R., Auty, D., Coops, N. C., Tompalski, P., Goodbody, T. R., Meador, A. S., Bourdon, J.-F., De Boissieu, F., and Achim, A. (2020). lidR: An R package for analysis of Airborne Laser Scanning (ALS) data. *Remote Sensing of Environment*, 251:112061.

Sæbø, A., Popek, R., Nawrot, B., Hanslin, H., Gawronska, H., and Gawronski, S. (2012). Plant species differences in particulate matter accumulation on leaf surfaces. *Science of the Total Environment*, 427:347–354.

Sagan, V., Maimaitijiang, M., Sidike, P., Maimaitiyiming, M., Erkbol, H., Hartling, S., Peterson, K. T., Peterson, J., Burken, J., and Fritschi, F. (2019). UAV/satellite multiscale data fusion for crop monitoring and early stress detection. *International Archives of the Photogrammetry, Remote Sensing and Spatial Information Sciences - ISPRS Archives*, 42(2/W13):715–722.

Schaaf, C. B., Gao, F., Strahler, A. H., Lucht, W., Li, X., Tsang, T., Strugnell, N. C., Zhang, X., Jin, Y., Muller, J.-p., Lewis, P., Barnsley, M., Hobson, P., Disney, M., Roberts, G., Dunderdale, M., Doll, C., Robert, P., Hu, B., Liang, S., Privette, J. L., and Roy, D. (2002). First operational BRDF, albedo nadir reflectance products from MODIS. *Remote Sensing of Environment*, 83:135–148.

Scheffers, B. R., Edwards, D. P., Diesmos, A., Williams, S. E., and Evans, T. A. (2014). Microhabitats reduce animal's exposure to climate extremes. *Global Change Biology*, 20(2):495–503.

Scherrer, D. and Koerner, C. (2010). Infra-red thermometry of alpine landscapes challenges climatic warming projections. *Global Change Biology*, 16(9):2602–2613.

Selmi, W., Weber, C., Rivière, E., Blond, N., Mehdi, L., and Nowak, D. (2016). Air pollution removal by trees in public green spaces in strasbourg city, france. *Urban Forestry & Urban Greening*, 17:192–201.

Shaw, R. H. and Pereira, A. (1982). Aerodynamic roughness of a plant canopy: a numerical experiment. *Agricultural Meteorology*, 26(1):51–65.

Sicard, P., Agathokleous, E., Araminiene, V., Carrari, E., Hoshika, Y., De Marco, A., and Paoletti, E. (2018). Should we see urban trees as effective solutions to reduce increasing ozone levels in cities? *Environmental Pollution*, 243:163–176.

Siok, K., Ewiak, I., and Jenerowicz, A. (2020). Multi-sensor fusion: A simulation approach to pansharpening aerial and satellite images. *Sensors*, 20(24):1–18.

Slabejová, D., Bacigál, T., Hegedüšová, K., Májeková, J., Medvecká, J., Mikulová, K., Šibíková, M., Škodová, I., Zaliberová, M., and Jarolímek, I. (2019). Comparison of the understory vegetation of native forests and adjacent Robinia pseudoacacia plantations in the Carpathian-Pannonian region. *Forest Ecology and Management*, 439:28–40.

Smith, A. M. and Ramsay, P. M. (2018). A comparison of ground-based methods for estimating canopy closure for use in phenology research. *Agricultural and Forest Meteorology*, 252:18–26.

Smith-Tripp, S. M., Eskelson, B. N., Coops, N. C., and Schwartz, N. B. (2022). Canopy height impacts on the growing season and monthly microclimate in a burned forest of british columbia, canada. *Agricultural and Forest Meteorology*, 323:109067.

Snavely, N., Seitz, S. M., and Szeliski, R. (2008). Modeling the world from Internet photo collections. *International Journal of Computer Vision*, 80(2):189–210.

Sobrino, J., Jiménez-Muñoz, J., Sòria, G., Ruescas, A., Danne, O., Brockmann, C., Ghent, D., Remedios, J., North, P., Merchant, C., et al. (2016). Synergistic use of MERIS and AATSR as a proxy for estimating Land Surface Temperature from Sentinel-3 data. *Remote Sensing of Environment*, 179:149–161.

Srbinovska, M., Andova, V., Mateska, A. K., and Krstevska, M. C. (2021). The effect of small green walls on reduction of particulate matter concentration in open areas. *Journal of Cleaner Production*, 279:123306.

Stenberg, P., Linder, S., Smolander, H., and Flower-Ellis, J. (1994). Performance of the LAI-2000 plant canopy analyzer in estimating leaf area index of some Scots pine stands. *Tree Physiology*, 14(7-8-9):981–995.

Stickley, S. F. and Fraterrigo, J. M. (2021). Understory vegetation contributes to microclimatic buffering of near-surface temperatures in temperate deciduous forests. *Landscape Ecology*, 36(4):1197–1213.

Su, A., Qi, J., and Huang, H. (2020). Indirect measurement of forest canopy temperature by handheld thermal infrared imager through upward observation. *Remote Sensing*, 12(21):3559.

Suggitt, A. J., Gillingham, P. K., Hill, J. K., Huntley, B., Kunin, W. E., Roy, D. B., and Thomas, C. D. (2011). Habitat microclimates drive fine-scale variation in extreme temperatures. *Oikos*, 120(1):1–8.

Suggitt, A. J., Wilson, R. J., Isaac, N. J., Beale, C. M., Auffret, A. G., August, T., Bennie, J. J., Crick, H. Q., Duffield, S., Fox, R., Hopkins, J. J., Macgregor, N. A., Morecroft, M. D., Walker, K. J., and Maclean, I. M. (2018). Extinction risk from climate change is reduced by microclimatic buffering. *Nature Climate Change*, 8(8):713–717.

Sun, Z., Wang, X., Wang, Z., Yang, L., Xie, Y., and Huang, Y. (2021). UAVs as remote sensing platforms in plant ecology: Review of applications and challenges. *Journal of Plant Ecology*, 14(6):1003–1023.

Tallis, M., Taylor, G., Sinnett, D., and Freer-Smith, P. (2011). Estimating the removal of atmospheric particulate pollution by the urban tree canopy of london, under current and future environments. *Landscape and Urban Planning*, 103(2):129–138.

Thomas, C. D., Cameron, A., Green, R. E., Bakkenes, M., Beaumont, L. J., Collingham, Y. C., Erasmus, B. F., Ferreira De Siqueira, M., Grainger, A., Hannah, L., Hughes, L., Huntley, B., Van Jaarsveld, A. S., Midgley, G. F., Miles, L., Ortega-Huerta, M. A., Peterson, A. T., Phillips, O. L., and Williams, S. E. (2004). Extinction risk from climate change. *Nature*, 427(6970):145–148.

Tian, X., Li, Z. Y., van der Tol, C., Su, Z., Li, X., He, Q. S., Bao, Y. F., Chen, E. X., and Li, L. H. (2011). Estimating zero-plane displacement height and aerodynamic roughness length using synthesis of LiDAR and SPOT-5 data. *Remote Sensing of Environment*, 115(9):2330–2341.

Tichý, L. (2016). Field test of canopy cover estimation by hemispherical photographs taken with a smartphone. *Journal of Vegetation Science*, 27(2):427–435.

Tillack, A., Clasen, A., Kleinschmit, B., and Förster, M. (2014). Estimation of the seasonal leaf area index in an alluvial forest using high-resolution satellite-based vegetation indices. *Remote Sensing of Environment*, 141:52–63.

Tinkham, W. T. and Swayze, N. C. (2021). Influence of Agisoft Metashape parameters on UAS structure from motion individual tree detection from canopy height models. *Forests*, 12(2):1–14.

Tinya, F., Márialigeti, S., Király, I., Németh, B., and Ódor, P. (2009). The effect of light conditions on herbs, bryophytes and seedlings of temperate mixed forests in Őrség, Western Hungary. *Plant Ecology*, 204(1):69–81.

Tiwari, A., Kumar, P., Baldauf, R., Zhang, K. M., Pilla, F., Di Sabatino, S., Brattich, E., and Pulvirenti, B. (2019). Considerations for evaluating green infrastructure impacts in microscale and macroscale air pollution dispersion models. *Science of The Total Environment*, 672:410–426.

Tiwary, A., Sinnett, D., Peachey, C., Chalabi, Z., Vardoulakis, S., Fletcher, T., Leonardi, G., Grundy, C., Azapagic, A., and Hutchings, T. R. (2009). An integrated tool to assess the role of new planting in PM_{10} capture and the human health benefits: A case study in London. *Environmental Pollution*, 157(10):2645–2653.

Tolasz, R., Brázdil, R., Bulíř, O., Dobrovolný, P., Dubrovský, M., Hájková, L., Halásová, O., Hostýnek, J., Janouch, M., Kohout, M., Krška, K., Křivancová, S., Květoň, V., Lepka, Z., Lipina, P., Macková, J., Metelka, L., Míková, T., Mrkvica, Z., Možný, M., Nekovář, J., Němec, L., Pokorný, J., Reitschläger, J. D., Richterová, D., Jaroslav, R., Řepka, M., Semerádová, D., Sosna, V., Stříž, M., Šercl, P., Škáchová, H., Štěpánek, P., Štěpánková, P., Trnka, M., Valeriánová, A., Valter, J., Vaníček, K., Vavruška, F., Voženílek, V., Vráblík, T., Vysoudil, M., Zahradníček, J., Zusková, I., Žák, M., and Žalud, Z. (2007). *Climate atlas of Czechia*. Czech Hydrometeorological Institute and UP Olomouc, Prague, Olomouc, 1 edition.

Tomaštík, J., Mokroš, M., Saloš, S., Chudỳ, F., and Tunák, D. (2017). Accuracy of photogrammetric UAV-based point clouds under conditions of partially-open forest canopy. *Forests*, 8(5).

Tomlinson, C. J., Chapman, L., Thornes, J. E., and Baker, C. (2011). Remote sensing land surface temperature for meteorology and climatology: A review. *Meteorological Applications*, 18(3):296–306.

Trepekli, K. and Friborg, T. (2021). Deriving aerodynamic roughness length at ultra-high resolution in aricultural areas using UAV-borne LiDAR. *Remote Sensing*, 13(17):1–21.

Turnipseed, A. A., Burns, S. P., Moore, D. J., Hu, J., Guenther, A. B., and Monson, R. K. (2009). Controls over ozone deposition to a high elevation subalpine forest. *Agricultural and Forest Meteorology*, 149(9):1447–1459.

Tymen, B., Vincent, G., Courtois, E. A., Heurtebize, J., Dauzat, J., Marechaux, I., and Chave, J. (2017). Quantifying micro-environmental variation in tropical rainforest understory at landscape scale by combining airborne lidar scanning and a sensor network. *Annals of Forest Science*, 74:1–13.

United Nations, Department of Economic and Social Affairs, P. D. (2019). *World Urbanization Prospects: The 2018 Revision (ST/ESA/SER.A/420)*. United Nations, New York.

Vanwalleghem, T. and Meentemeyer, R. (2009). Predicting forest microclimate in heterogeneous landscapes. *Ecosystems*, 12:1158–1172.

Von Arx, G., Dobbertin, M., and Rebetez, M. (2012). Spatio-temporal effects of forest canopy on understory microclimate in a long-term experiment in Switzerland. *Agricultural and Forest Meteorology*, 166-167:144–155.

Von Arx, G., Graf Pannatier, E., Thimonier, A., and Rebetez, M. (2013). Microclimate in forests with varying leaf area index and soil moisture: potential implications for seedling establishment in a changing climate. *Journal of ecology*, 101(5):1201–1213.

Wallace, A. R. (1878). *Tropical nature, and other essays.* Macmillan and Company.

Wallace, L., Lucieer, A., Malenovskỳ, Z., Turner, D., and Vopěnka, P. (2016). Assessment of forest structure using two UAV techniques: A comparison of airborne laser scanning and structure from motion (SfM) point clouds. *Forests*, 7(62):1–16.

Wallace, L., Lucieer, A., Watson, C., and Turner, D. (2012). Development of a UAV-LiDAR system with application to forest inventory. *Remote Sensing*, 4(6):1519–1543.

Wang, X., Wang, Y., Zhou, C., Yin, L., and Feng, X. (2021). Urban forest monitoring based on multiple features at the single tree scale by UAV. *Urban Forestry & Urban Greening*, 58:126958.

Wang, Y., Kim, J. H., Mao, Z., Ramel, M., Pailler, F., Perez, J., Rey, H., Tron, S., Jourdan, C., and Stokes, A. (2018). Tree root dynamics in montane and sub-alpine mixed forest patches. *Annals of Botany*, 122(5):861–872.

Wang, Z., Erb, A. M., Schaaf, C. B., Sun, Q., Liu, Y., Yang, Y., Shuai, Y., Casey, K. A., and Román, M. O. (2016). Early spring post-fire snow albedo dynamics in high latitude boreal forests using Landsat-8 OLI data. *Remote Sensing of Environment*, 185:71–83.

Wang, Z., Schaaf, C. B., Strahler, A. H., Chopping, M. J., Román, M. O., Shuai, Y., Woodcock, C. E., Hollinger, D. Y., and Fitzjarrald, D. R. (2014). Evaluation

of MODIS albedo product (MCD43A) over grassland, agriculture and forest surface types during dormant and snow-covered periods. *Remote Sensing of Environment*, 140:60–77.

Watson, D. J. (1947). Comparative physiological studies on the growth of field crops: I. variation in net assimilation rate and leaf area between species and varieties, and within and between years. *Annals of Botany*, 11(41):41–76.

Wedeux, B., Dalponte, M., Schlund, M., Hagen, S., Cochrane, M., Graham, L., Usup, A., Thomas, A., and Coomes, D. (2020). Dynamics of a human-modified tropical peat swamp forest revealed by repeat lidar surveys. *Global Change Biology*, 26(7):3947–3964.

Weiss, M. and Baret, F. (2010). CAN-EYE V6. 1 USER MANUAL.

Welles, J. M. and Norman, J. (1991). Instrument for indirect measurement of canopy architecture. *Agronomy Journal*, 83(5):818–825.

Wild, J., Kopecký, M., Macek, M., Šanda, M., Jankovec, J., and Haase, T. (2019). Climate at ecologically relevant scales: A new temperature and soil moisture logger for long-term microclimate measurement. *Agricultural and Forest Meteorology*, 268:40–47.

Woodgate, W., Jones, S. D., Suarez, L., Hill, M. J., Armston, J. D., Wilkes, P., Soto-Berelov, M., Haywood, A., and Mellor, A. (2015). Understanding the variability in ground-based methods for retrieving canopy openness, gap fraction, and leaf area index in diverse forest systems. *Agricultural and Forest Meteorology*, 205:83–95.

Wu, C., Gong, H., Zhang, Y., Sha, L., Xie, Y., Tan, Z., Schaefer, D., Lu, Z., Liu, Y., and You, G. (2012). Observed air/soil temperature trends in open land and understory of a subtropical mountain forest, SW China. *International Journal of Climatology*, 33(5):1308–1316.

Yang, J., Chang, Y., and Yan, P. (2015). Ranking the suitability of common urban tree species for controlling $PM_{2.5}$ pollution. *Atmospheric Pollution Research*, 6(2):267–277.

Yang, J., Yu, Q., and Gong, P. (2008). Quantifying air pollution removal by green roofs in Chicago. *Atmospheric Environment*, 42(31):7266–7273.

Yang, W., Shabanov, N. V., Huang, D., Wang, W., Dickinson, R. E., Nemani, R. R., Knyazikhin, Y., and Myneni, R. B. (2006). Analysis of leaf area index products from combination of MODIS Terra and Aqua data. *Remote Sensing of Environment*, 104(3):297–312.

Yoshimura, T. and Hasegawa, H. (2003). Comparing the precision and accuracy of GPS positioning in forested areas. *Journal of Forest Research*, 8(3):147–152.

Zakrzewska, A., Kopeć, D., Krajewski, K., and Charyton, J. (2022). Canopy temperatures of selected tree species growing in the forest and outside the forest using aerial thermal infrared (3.6–4.9 μm) data. *European Journal of Remote Sensing*, 55(1):313–325.

Zapletal, M. and Chroust, P. (2007). Ozone deposition to a coniferous and deciduous forest in the Czech Republic. *Wate, Air & Soil Pollution: Focus*, 7:187–200.

Zapletal, M., Cudlín, P., Chroust, P., Urban, O., Pokornỳ, R., Edwards-Jonášová, M., Czernỳ, R., Janouš, D., Taufarová, K., Večeřa, Z., et al. (2011). Ozone flux over a norway spruce forest and correlation with net ecosystem production. *Environmental Pollution*, 159(5):1024–1034.

Zellweger, F., Coomes, D., Lenoir, J., Depauw, L., Maes, S. L., Wulf, M., Kirby, K., Brunet, J., Kopecký, M., Máliš, F., Schmidt, W., Heinrichs, S., den Ouden, J., Jaroszewicz, B., Buyse, G., Spicher, F., Verheyen, K., and De Frenne, P. (2019a). Seasonal drivers of understorey temperature buffering in temperate deciduous forests across Europe. *Global Ecology and Biogeography*, 28:1774– 1786.

Zellweger, F., De Frenne, P., Lenoir, J., Rocchini, D., and Coomes, D. (2019b). Advances in microclimate ecology arising from remote sensing. *Trends in Ecology & Evolution*, 34(4):327–341.

Zellweger, F., De Frenne, P., Lenoir, J., Vangansbeke, P., Verheyen, K., Bernhardt-Römermann, M., Baeten, L., Hédl, R., Berki, I., Brunet, J., Van Calster, H., Chudomelová, M., Decocq, G., Dirnböck, T., Durak, T., Heinken, T., Jaroszewicz, B., Kopecký, M., Máliš, F., Macek, M., Malicki, M., Naaf, T., Nagel, T. A., Ortmann-Ajkai, A., Petřík, P., Pielech, R., Reczynska, K., Schmidt, W., Standovár, T., Swierkosz, K., Teleki, B., Vild, O., Wulf, M., and Coomes, D. (2020). Forest microclimate dynamics drive plant responses to warming. *Science*, 368(6492):772–775.

Zhang, D., Liu, J., Ni, W., Sun, G., Zhang, Z., Liu, Q., and Wang, Q. (2019). Estimation of forest leaf area index using height and canopy cover information

extracted from unmanned aerial vehicle stereo imagery. *IEEE Journal of Selected Topics in Applied Earth Observations and Remote Sensing*, 12(2):471–481.

Zhang, L., Gong, S., Padro, J., and Barrie, L. (2001). A size-segregated particle dry deposition scheme for an atmospheric aerosol module. *Atmospheric Environment*, 35(3):549–560.

Zhang, Y., Chen, J. M., and Miller, J. R. (2005). Determining digital hemispherical photograph exposure for leaf area index estimation. *Agricultural and Forest Meteorology*, 133(1-4):166–181.

Zhu, K., Woodall, C. W., and Clark, J. S. (2012). Failure to migrate: Lack of tree range expansion in response to climate change. *Global Change Biology*, 18(3):1042–1052.

Zhu, X., Cai, F., Tian, J., and Williams, T. K.-A. (2018). Spatiotemporal fusion of multisource remote sensing data: Literature survey, taxonomy, principles, applications, and future directions. *Remote Sensing*, 10(4):527.

Zielewska-Büttner, K., Adler, P., Ehmann, M., and Braunisch, V. (2016). Automated detection of forest gaps in spruce dominated stands using canopy height models derived from stereo aerial imagery. *Remote Sensing*, 8(3):175.

Zurita-Milla, R., Clevers, J. G., and Schaepman, M. E. (2008). Unmixing-based landsat tm and meris fr data fusion. *IEEE Geoscience and Remote Sensing Letters*, 5(3):453–457.

Chapter 10

Curriculum Vitae
& List of Publications

Personal

Name: Vít Kašpar
Date of birth: March 16th, 1992 (*Czechia*)
E-mail: kasparvit@fzp.czu.cz
ORCID: https://orcid.org/0000-0002-0879-0137
RG: https://www.researchgate.net/profile/Vit-Kaspar

Affiliations

2017 – present
Department of Spatial Sciences
Faculty of Environmental Sciences
Czech University of Life Sciences Prague

2017 – 2021
Department of Geoecology
Institute of Botany of the Czech Academy of Sciences

Education

2017 – present
Department of Spatial Sciences
Faculty of Environmental Sciences
Czech University of Life Sciences Prague
PhD studies in Environmental Modelling
Thesis topic: Indirect methods for modelling forest microclimate

2014 – 2017
Faculty of Science
Charles University
Master's degree in Physical Geography and Geoecology
Thesis topic: Development of gully erosion – mapping, dynamics and influencing factors

1 – 6/2016
Department of Geography
The University of Sheffield, the UK
Erasmus+ study abroad

2014 – 2016
Faculty of Science
Charles University
Complementary Teaching Geography Education
Thesis topic: Landscape evolution in geographical education

2011 – 2014
Faculty of Science
Charles University
Bachelor's degree in Geography and Cartographyt
Thesis topic: Response of sedimentation and erosion rates to changing human pressure

Participation in Research Projects

2018 – 2022
Clear air and climate adaptation in Ostrava and other cities
Urban Innovation Actions, European Regional Development Fund
Co-investigator

2020
From orbit to understorey: modelling forest microclimate by satellite remote sensing
Deutsche Bundesstiftung Umwelt
Leader

2017 – 2019
Forest microclimate - neglected link between plant diversity and climate change
Czech Science Foundation
Co-investigator

2018 – 2019
Modelling of inner forest environment by UAV-based remote sensing techniques
Internal Grant Agency of the Faculty of Environmental Sciences
Leader

Awards

2021
Czech University of Life Sciences Prague
1st place in Rector's Award for the best publication outputs of doctoral students

2017
ESRI GIS, Czech Republic
2nd place in the poster conference competition

Internships

7/2022 – 8/2022
Institute of Ecology, Chair of Climatology
Technical University Berlin, Germany
Erasmus+ traineenship

1/2020 – 2/2021
Institute of Botany of the Czech Academy of Sciences
GROW Programme of support for talented doctoral students

2/2020 – 7/2020
Institute of Landscape Architecture and Environmental Planning
Chair of Geoinformation in Environmental Planning
Technical University Berlin, Germany
DBU fellowship for graduates from Central and Eastern Europe

5/2019 – 9/2019
Institute of Ecology, Chair of Climatology
Technical University Berlin, Germany
Erasmus+ traineenship

International Conferences

10/2021
Application drone-based remote sensing in modelling ozone removal by urban greenery in the city Ostrava,the Czech Republic
Zapletal, M., **Kašpar, V.**, Samec, P., Juráň, S. Víchová, P., Hladík, J.
In: IUFRO conference on "Air Pollution threats to Plant Ecosystems".
Paphos, Cyprus.

5/2019
Determination of forest microclimate from remote sensing proxy variables
Kašpar, V., Hederová, L., Kopecký, M., Macek, M., Müllerová, J., Wild, J.
In: Living Planet Symposium.
Milan, Italy.

1/2019
Forest microclimate and its modelling by remote sensing proxy variables
Kašpar, V., Hederová, L., Kopecký, M., Macek, M., Müllerová, J., Wild, J.
In: *9th Biennial Conference of the International Biogeography Society* Malaga, Spain.

9/2018
Assessing canopy openness in dense forests from photogrammetric canopy height model.
Kašpar, V., Hederová, L., Kopecký, M., Macek, M., Müllerová, J., Wild, J.
In: *1st EARSeL UAS Workshop – "UAS for mapping and monitoring"*. Warshaw, Poland.

Publications in Journals with Impact Factor (J$_{imp}$)

Ecologically relevant canopy openness from hemispherical photographs (2023). Hederová, L. Macek, M., Wild, J. Brůna, J., **Kašpar, V.**, Klinerová, T. Kopecký, M.*Agriculture and Forest Meteorology.*, Elsevier, vol. 330, p. 109308.

Unmanned Aerial Systems for modelling air pollution removal by urban greenery (2022). **Kašpar, V.**, Zapletal, M. Samec, P., Komárek, J., Bílek, J., Juráň, S. *Urban Forestry and Urban Greening*, Elsevier, vol. 78, p. 127757.

Global maps of soil temperature (2022). Lembrechts, J. J., van den Hoogen, J., Aalto, J., Ashcroft, M. B., De Frenne, P., Kemppinen, J., Kopecký, M., Luoto, M. . . . , **Kašpar, V.**, . . . , Lenoir, J. *Global Change Biology*, Wiley Online Library, vol. 28, p. 3110-3144.

Temperature buffering in temperate forests: Comparing microclimate models based on ground measurements with active and passive remote sensing (2021). **Kašpar, V.**, Hederová, L., Macek, M., Müllerová, J., Prošek, J., Surový, P. Wild, J., Kopecký, M. *Remote Sensing of Environment*, Elsevier, vol. 263, p. 112522.

Other Publications

Adaptation Strategy of the city to climate change. Comprehensive and strategic and planning document of the city of Vsetín (2022). Vizina, Š., Kantor, Č., Frélich, Z. **Kašpar, V.**, Przybyla, R., Ausficír, J., Jurečka, F., Misiaček, R., Vojkovská, R., Karkoszková, Z., City of Vsetín. 221 p.

Local adaptation strategy of the city České Budějovice to climate change (2022). Misiaček, R., Vojkovská, R., Karkoszková, Z. Vizina, Š., Kantor, Č., Frélich, Z. **Kašpar, V.**, Ausficír, J., Jurečka, F., Ander, M. Maceková, M., Čech, M., City of České Budějovice. 191 p.

Green Infrastructure and its effect on air quality. Methodology of planting greenery in urban areas in order to capture pollution (2021). Zapletal, M, **Kašpar, V.**, Samec, P. Bílek, Jiří, Doležal, K. Víchová, P., Balcar, T. Kalužová, G. Juráň, S., Hladík, J., Buček, P., Martaus, A., Blahůšková, V., Vráblová, M., Maršolek, P. Statutory City of Ostrava / Strategic Development Department. ISBN 978-80-88399-04-9. 104 p.

Green Infrastructure for Cities. (2021). Zapletal, M, **Kašpar, V.**, Samec, P. Bílek, Jiří, Doležal, K. Víchová, P., Balcar, T. Kalužová, G. Juráň, S., Hladík,J. Statutory City of Ostrava / Strategic Development Department. ISBN 978-80-88399-01-8. 68 p.

Teaching Experience

2017 – 2019
Department of Spatial Sciences,
Czech University of Life Sciences Prague
Lecturer and assessor of GIS; GIS II
Supervisor and consultant of bachelor´s and master´s theses

2020 – 2023
1st International School of Ostrava
Teacher of geography and humanities